# WEAK LENSING AND MODIFIED GRAVITY OF COSMIC STRUCTURE

Joseph Clampitt

A DISSERTATION

in

**Physics and Astronomy**

Presented to the Faculties of the University of Pennsylvania

in

Partial Fulfillment of the Requirements for the Degree of

**Doctor of Philosophy**

2014

| **Supervisor of Dissertation** | **Graduate Group Chairperson** |
|---|---|
| Bhuvnesh Jain | Randall Kamien |
| Professor, Physics and Astronomy | Professor, Physics and Astronomy |

**Dissertation Comittee:**

Gary Bernstein, Professor, Physics and Astronomy
Larry Gladney, Professor, Physics and Astronomy
Bhuvnesh Jain, Professor, Physics and Astronomy
Ravi Sheth, Professor, Physics and Astronomy
Justin Khoury, Associate Professor, Physics and Astronomy

# Acknowledgements

I would like to thank my thesis committee, Gary Bernstein, Larry Gladney, Bhuvnesh Jain, Justin Khoury, and Ravi Sheth, for taking the time to review my thesis work. Thanks go also to the Cosmology and Astrophysics Professors who made this an interesting subject to learn: Gary Bernstein, Bhuvnesh Jain, Justin Khoury, Adam Lidz, and Mark Trodden. I'm grateful to my officemates, Melinda Andrews, Alan Meert, and David Moore for answering numerous Python and LaTeX questions. I'm indebted to a number of postdocs at Penn for their mentorship: Anna Cabré, Yan-Chuan Cai, Tim Eifler, Elisabeth Krause, Marcos Lima, and Vinu Vikram. I'd like to thank my collaborators on the projects composing this thesis: Yan-Chuan Cai, Bhuvnesh Jain, Justin Khoury, Baojiu Li, and Masahiro Takada. I would like to thank the National Science Foundation and Department of Energy for the funding that made this research possible. A special thanks goes to Erin Sheldon for the generous use of his shear catalogs, without which the measurements in the second half of this thesis would have been impossible. Special thanks go also to Mike Jarvis for clear, intuitive explanations of many difficult topics. I will always be grateful to Yan-Chuan Cai for his guidance and mentoring, especially in the early stages of graduate school. Finally I'd like to thank my advisor, Bhuvnesh Jain, for a valuable graduate school experience, especially for the freedom to work on interesting projects and the opportunity to travel and be stimulated by conversations with numerous people in the field.

## ABSTRACT

WEAK LENSING AND MODIFIED GRAVITY OF COSMIC STRUCTURE

Joseph Clampitt

Bhuvnesh Jain

We offer predictions of symmetron modified gravity in the neighborhood of realistic dark matter halos. The predictions for the fifth force (FF) are obtained by solving the nonlinear symmetron equation of motion in the spherical NFW approximation. We compare the three major known screening mechanisms: Vainshtein, Chameleon, and Symmetron around such dark matter sources, emphasizing the significant differences between them and highlighting observational tests which exploit these differences. In addition to halos, we investigate the behavior of the FF in voids in chameleon modified gravity models using the spherical collapse method. The FF can be many times larger than the Newtonian force. This is very different from the case in halos, where the FF is no more than 1/3 of gravity. Individual voids in chameleon models grow larger by 10%. The number density is up to 2.5 times larger in chameleon models. This difference is about 10 times larger than that in the halo mass function. Turning to weak lensing data analysis, we search for the lensing signal of massive filaments between 220,000 pairs of Luminous Red Galaxies (LRGs) from the Sloan Digital Sky Survey. We use a nulling technique to remove the contribution of the LRG halos, resulting in a 10-sigma detection of the filament lensing signal. We compare the measurements with halo model predictions based on a calculation of 3-point halo-halo-mass correlations. Comparing the "thick" halo model filament to a "thin" string of halos, thick filaments larger than a Mpc in width are clearly preferred by the data. In addition to filaments, dark matter voids should exhibit a weak lensing signal. We find voids in the galaxy distribution using a novel algorithm, then perform a stacked shear measurement on 20,000 voids with radii between 15-40 Mpc/h and redshifts between 0.16-0.37. We detect the characteristic radial shear signal of voids with a statistical significance that exceeds 13-sigma. The mass profile corresponds to a fractional underdensity of about -0.4 inside the void radius and a slow approach to the mean density.

# Contents

CONTENTS

# List of Tables

# List of Figures

## LIST OF FIGURES

# Chapter 1

# Introduction

## 1.1 Modified Gravity

### 1.1.1 How and why does Modified Gravity replace Dark Energy?

The standard model of cosmology calls for a universe in which only a small fraction of the matter and energy come from the standard baryonic material which makes up the stars and galaxies that we observe directly. Under the assumption that Einstein's theory of general relativity (GR) is true at cosmological scales, it is necessary to postulate a component of the universe known as dark energy, which is very successful at accounting for the observed expansion of space. This substance must currently make up $\sim 70\%$ of the total matter/energy of the universe in order to cause the observed rate of expansion. This is disconcerting, but given GR, the cosmological constant is a convenient solution to the expanding universe problem. The Einstein-Hilbert action of GR

$$S = \int \mathrm{d}^4x\sqrt{-g}\left[\frac{R}{16\pi G} + \mathcal{L}_m\right] , \tag{1.1}$$

can be varied with respect to the metric $g^{\mu\nu}$, yielding Einstein's equation

$$R_{\mu\nu} - \frac{1}{2}R\, g_{\mu\nu} = 8\pi G T_{\mu\nu} . \tag{1.2}$$

Including a cosmological constant is straightforward

$$S = \int \mathrm{d}^4x\sqrt{-g}\left[\frac{R}{16\pi G} - \Lambda + \mathcal{L}_m\right], \tag{1.3}$$

and it results in an additional term which causes the background expansion of the universe

$$R_{\mu\nu} - \frac{1}{2}R\, g_{\mu\nu} = 8\pi G(T_{\mu\nu} - \Lambda\, g_{\mu\nu})\,. \tag{1.4}$$

This modification is sufficient to explain the observed expansion of space.

However, the dearth of tests of GR on large scales leaves room for alternative explanations: there are a number of ideas which seek to explain the expansion without dark energy by modifying the fundamental equations of GR (12, 27, 56, 94). Hence, we call these Modified Gravity (MG) theories. For example, the Einstein-Hilbert action can be modified by replacing the Ricci scalar $R$ by some function of $R$,

$$S = \int \mathrm{d}^4x\sqrt{-\tilde{g}}\left[\frac{R + f(R)}{16\pi G} + \mathcal{L}_m\right]. \tag{1.5}$$

One functional form is popular enough to be known as *the* $f(R)$ theory (52)

$$f(R) = -m^2\frac{c_1(R/m^2)^n}{c_2(R/m^2)^n + 1}\,. \tag{1.6}$$

In the high-curvature limit ($m^2/R \to 0$),

$$f(R) \approx -\frac{c_1}{c_2}m^2 + \frac{c_1}{c_2^2}m^2\left(\frac{m^2}{R}\right)^n, \tag{1.7}$$

so that the first term acts as a cosmological constant. The second term has other observable consequences which are sometimes called the "fifth force." However, one of the challenges in developing new models of gravity is the necessity for the theory to agree with GR on scales within the solar system, where GR has been verified to high precision. Although the theory may make different predictions on large scales, these differences must be minimized in the presence of high density environments such as the Milky Way. This ability of a theory is called its "screening" mechanism (56), due to the way it hides the fifth force in high density environments.

### 1.1.2 Screening of the Fifth Force

Equation (1.6) can be rewritten in terms of a transformed metric $g_{\mu\nu}$ as

$$S = \int \mathrm{d}^4x\sqrt{-g}\left[\frac{M_{\rm Pl}^2}{2}R - \frac{1}{2}(\partial\phi)^2 - V(\phi)\right] + \int \mathrm{d}^4x\,\mathcal{L}_m[\tilde{g}]\,. \tag{1.8}$$

This form makes explicit that while matter is minimally coupled to the metric $\tilde{g}_{\mu\nu}$, the action can be written so as to decouple an Einstein-Hilbert piece from a piece involving kinetic and potential terms of a scalar field, $\phi$. Thus gravity described with metric $g_{\mu\nu}$ plus a scalar field is said to be in the "Einstein frame," in contrast to the description in terms of $\tilde{g}_{\mu\nu}$ and no additional scalar field which is called the "Jordan frame." The Einstein frame is intuitive in that the first term of Eq. (1.8) reproduces Einstein's equation, Eq. (1.2). The coupling function $A(\phi)$ relates the Jordan and Einstein frame metrics

$$\tilde{g}_{\mu\nu} = g_{\mu\nu}A^2(\phi)\,. \tag{1.9}$$

The Jordan frame energy-momentum tensor is the one that is conserved

$$\tilde{\nabla}_\mu\tilde{T}^{\mu\nu} = 0\,, \tag{1.10}$$

while in Einstein frame the conserved energy density is

$$\rho = A^3(\phi)\tilde{\rho}\,. \tag{1.11}$$

The details of the conformal transformation between Einstein and Jordan frames are described in Carroll (11), beginning at Eq. (4.129). Note that since the scalar field $\phi$ also participates in the gravitational interaction, particles do not follow geodesics of the Einstein frame metric.

Consider static, spherically-symmetric solutions, where $r$ is the radial coordinate. The time-time component of Eq. (1.2) yields the Poisson equation,

$$\nabla^2\Phi(r) = 4\pi G\rho(r)\,, \tag{1.12}$$

where $\Phi$ is the familiar Newtonian potential. The scalar field equation-of-motion (EOM) also involves the Laplacian, here acting on the scalar $\phi$,

$$\nabla^2\phi = \frac{\partial}{\partial\phi}(V + \rho A) \equiv \frac{\partial}{\partial\phi}V_{\rm eff}\,, \tag{1.13}$$

with boundary conditions

$$\frac{d\phi}{dr}|_{r=0} = 0, \;\; \phi(r \to 0) = \phi_0\,. \tag{1.14}$$

These equations are sufficient to solve for the radial profiles $\Phi(r)$ and $\phi(r)$. These profiles then determine the forces according to

$$F_{\rm N}(r) = -\nabla\Phi(r) \tag{1.15}$$

and

$$F_\phi(r) = -\nabla A(\phi(r)) = -\frac{\partial A}{\partial\phi}\nabla\phi(r)\,. \tag{1.16}$$

The net force is the sum of the Newtonian and fifth forces

$$F_{\rm total} = F_{\rm N} + F_\phi\,. \tag{1.17}$$

We now highlight two examples of screening: the symmetron (42) and chameleon (63) mechanisms.

#### 1.1.2.1 Symmetron Screening

The Symmetron (42) screening mechanism works by a quartic effective potential whose minima change drastically when moving from high to low density regions:

$$V_{\rm eff}(\phi) = \frac{1}{2}\left(\frac{\rho}{M_{\rm s}^2} - \mu^2\right)\phi^2 + \frac{1}{4}\lambda\phi^4\,. \tag{1.18}$$

A plot of the potential is shown in Fig. 1.1. The sign of the quadratic term in the potential determines how close the minimum is to $\phi = 0$. At high densities (left panel), the sign is

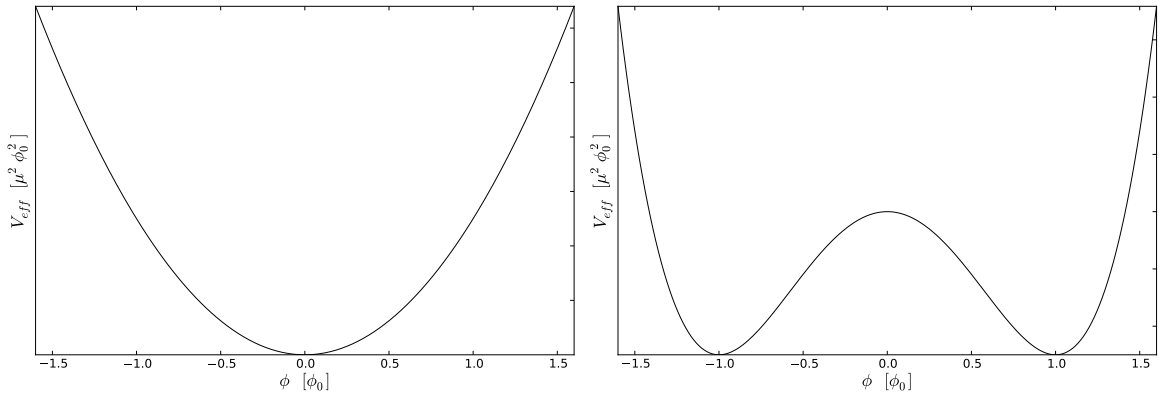


**Figure 1.1:** Shape of the symmetron effective potential in high density, $\rho \gg \bar{\rho}$ (*left panel*), and low density, $\rho \sim \bar{\rho}$ (*right panel*), environments. The x-axis shows the value of the scalar field in units of its value $\phi_0$ at the cosmic mean density. The field seeks to sit at the local minimum of the potential: when this corresponds to $\phi = 0$ as in high density environments, the fifth force, proportional to $\phi$, is screened and GR is restored.

positive and there is a single minimum at $\phi = 0$. For lower densities (right panel), however, the quadratic term flips sign and the field prefers to sit closer to its cosmic mean value $\phi_0$.

The difference between these two minima of $\phi$ has drastic consequences for the resulting forces. The coupling which produces such an effective potential is

$$A(\phi) = 1 + \frac{\phi^2}{2M_{\rm s}^2}\,, \tag{1.19}$$

with Eq. (1.16) giving the corresponding force

$$F_\phi(r) = -\nabla(\phi^2/2M_{\rm s}^2) = -\frac{\phi(r)}{M_{\rm s}}\frac{\nabla\phi(r)}{M_{\rm s}}\,. \tag{1.20}$$

Since $F_\phi \propto \phi(r)$, the small value that $\phi$ reaches inside a dense object sets the fifth force to zero. In the cosmic mean density, on the other hand, the field can couple to matter with gravitational strength, causing a fifth force.

More details of the symmetron theory and parameters can be found in Chapter 2, as well as detailed calculations of the screening in overdensities such as dark matter halos.

#### 1.1.2.2 Chameleon Screening

A second, related screening mechanism is that of the chameleon field (63, 64). An example of a chameleon effective potential is given by, e.g., Li & Zhao (76),

$$V_{\rm eff}(\phi) = \frac{\Lambda}{(1 - e^{-\phi/M_{pl}})^{\alpha}} + \rho e^{\gamma\phi/M_{pl}}\,, \tag{1.21}$$

with coupling

$$A(\phi) = e^{\gamma\phi/M_{\rm Pl}}\,. \tag{1.22}$$

Note that the chameleon effective potential shown in Fig. 1.2 is qualitatively similar to the symmetron potential of Fig. 1.1. The minimum is very near $\phi = 0$ for high density environments, but moves towards larger $\phi$ values for lower densities. However, the coupling is substantially different, resulting in a force

$$F_\phi(r) = \gamma e^{\gamma\phi/M_{\rm Pl}} \frac{\nabla\phi(r)}{M_{\rm Pl}}\,, \tag{1.23}$$

such that small values of $\phi$ can still generate fifth forces, as long as the field is still changing with $r(|\nabla\phi| > 0)$.

In order to understand chameleon screening, a distinction needs to be made between the minimum of the effective potential at a given point in space, which is a *local* quantity, and the value the field actually attains at that point. Call the local minima inside and outside an object $\phi_{\rm in}$ and $\phi_{\rm out}$, respectively. The actual value of the field is affected by the local density, but also by the global solution obeying the field's boundary conditions. The right panel of Fig. 1.2 shows the preferred value of the field outside a high density object, $\phi_{\rm out}$, and the left panel shows its preferred value at the center of the object, $\phi_{\rm in}$. In order to reach the preferred minimum $\phi_{\rm in} \sim 0$, the field has to pass through all intermediate values between $\phi_{\rm out}$ and $\phi_{\rm in}$. The details of this solution must be worked out case by case, according to Eq. (3.28), but schematically, the question of whether $\phi$ actually reaches its preferred minimum depends on the size of the object. A very dense but small object may

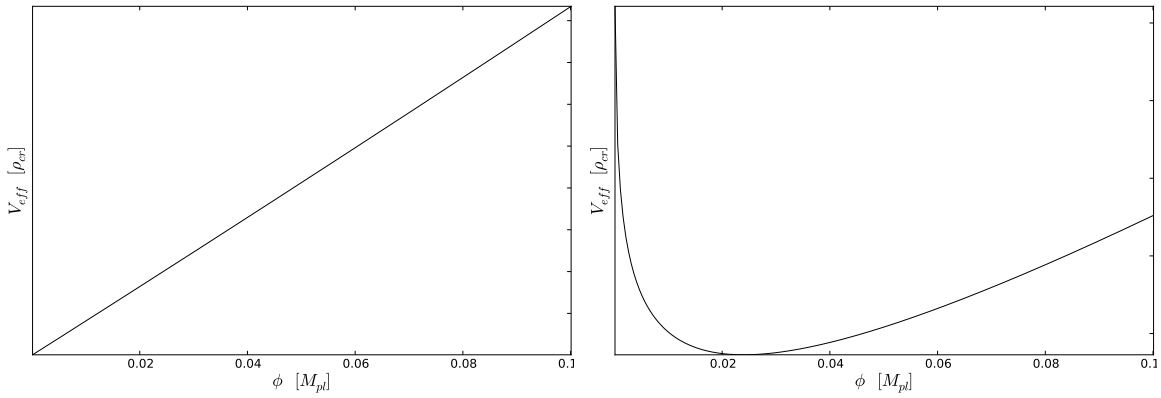


**Figure 1.2:** Same as Fig. 1.1, but showing chameleon potentials. In a high density medium the preferred minimum of the field is very near $\phi = 0$ (*left panel*), and moves to larger field values in less dense media (*right panel*). Since the chameleon force is proportional to $\nabla\phi$, and not $\phi$, this is not enough to say that high density objects are screened.

have a nonzero gradient of $\phi$ throughout, whereas a larger but less dense object could be partially screened when at some radius $r > 0$, the field attains its minimum, $\phi_{\rm in}$, and stays there all the way in to $r = 0$.

More details of this chameleon theory and parameters can be found in Chapter 3, as well as detailed solutions for the case of screening in underdensities such as dark matter voids.

### 1.1.3 The fifth force in astrophysical environments

As we move towards connecting with observations, it is useful to build some intuition for the effects of the fifth force. The following analogy with two of the other four forces, electromagnetism and Newtonian gravity, is inspired by Hui et al. (53). Recall Coulomb's law for the force between two objects with charges $q_1$ and $q_2$,

$$F_E = \frac{1}{4\pi\epsilon_0}\frac{q_1 q_2}{r^2}\,. \tag{1.24}$$

The force is proportional to the product of the charges of the two objects. In Newtonian gravity the masses $M_1$ and $M_2$ play a similar role

$$F_g = \frac{-G\,M_1 M_2}{r^2}\,.$$

Likewise, two objects can be thought of as having their own 5th force "charges," $Q_1$ and $Q_2$. The new wrinkle is that the charge is no longer a property purely of the object itself, but is dependent on the density of the larger-scale environment in which the object sits. The fifth force, mediated by the scalar field $\phi$ is, schematically,

$$F_\phi \propto \frac{-G\,Q_1(\rho_1, \rho_{env})\,Q_2(\rho_2, \rho_{env})}{r^2}\,. \tag{1.25}$$

The case of $Q_i \to 0$ is called screening. In this limit the predictions of the scalar tensor theory correspond to those of GR. Note also that at large distances there is a significant change in the range of the fifth force:

$$F_\phi \propto \frac{-G\,Q_1(\rho_1, \rho_{env})\,Q_2(\rho_2, \rho_{env})}{r^2} e^{-r/\lambda}\,, \tag{1.26}$$

where the Compton wavelength $\lambda$ for the theories we consider is confined to be $\sim$ Mpc (137). The exponential falloff is order unity for $r \lesssim \lambda$, but cuts the force off much faster than gravity for $r > \lambda$.

Even at the level of this mnemonic, it is possible to distinguish potentially interesting astrophysical and cosmological systems from those which are unlikely to exhibit the effects of a fifth force. The criteria for an interesting system is that both the source of gravity with charge $Q_1$ and the "test particle" with charge $Q_2$ are unscreened. Since $Q$ is also affected by the environment, this also requires looking for objects in low density environments. The following table illustrates how difficult it is to find systems which exhibit the fifth force:

| Environment | Source ($Q_1$) | test particle ($Q_2$) | $Q_1 \times Q_2$ |
|---|---|---|---|
| galaxy cluster | dwarf galaxy | HI gas clouds | 0 |
| | | dark matter (particles or subhalos) | 0 |
| | | main sequence stars | 0 |
| | | cepheid stars | 0 |
| | | light | 0 |
| void | dwarf galaxy | HI gas clouds | max |
| | | dark matter (particles or subhalos) | max |
| | | main sequence stars | 0 |
| | | cepheid stars | partial |
| | | light | 0 |

Note that some tests which seem useful at first glance are actually red-herrings, due to the degeneracy of the fifth force with the mass of the object. For example, puffy HI gas clouds in a dwarf galaxy in a void would show the effect of enhanced forces, whereas comparable gas clouds in a similar size dwarf galaxy in the neighborhood of a galaxy cluster would move under Newtonian gravity. But given only the information that dwarfs in voids tend to be heavier than those near clusters, it is not possible to distinguish whether these are two separate populations both moving according to GR, or the same population with only some members moving under the influence of the fifth force.

Nonetheless, there are a number of useful tests. For a dwarf galaxy in a void, the mass obtained from the motion of HI gas clouds and that of main sequence stars should be different (57, 134). Note that the schematic value of $Q_1 \times Q_2$ in the table depends on the value of the theory parameters. The above values correspond to an $f(R)$ theory in which the charge of the milky way just reaches $Q = 0$, that is, $|f_{R0}| = 10^{-6}$ in the theory of Hu & Sawicki (52). By comparison of the tight period-luminosity relation of Cepheids in different environments, Jain et al. (58) were able to put even tighter constraints on this theory.

As will be touched on at the beginning of § 1.2, photons have no fifth force charge so that gravitational lensing also provides a useful null test of the fifth force. This will be an important detail in chapter 2, which shows predictions for tests comparing the mass of galaxies obtained using dynamical tracers such as HI gas clouds and or small stars to those

obtained using weak lensing. In addition, in chapter 3 we will consider the lowest density environments available, cosmic voids, and predict the change in their size distribution given a fifth force that increases the outward push on their constituent dark matter particles.

## 1.2 Weak Lensing

In addition to the familiar movement of massive bodies in a gravitational field, General Relativity predicts that photons are deflected by gravity. The above discussion of fifth forces applies to non-relativistic particles which follow time-like geodesics, not relativistic particles following null geodesics. It can be shown that relativistic particles are immune to the effects of the fifth force; the details of the argument summarized here can be found in Padmanabhan (100), in Eqs. (4.68, 4.74) and the surrounding discussion. Padmanabhan (100) argues by first taking the point of view, different from our definitions in § 1.1, that the geodesic equation changes under conformal transformations. That is, all particles move on the geodesics of both frames, and thus Einstein frame does not need a separate scalar field and fifth force. Then, they show that while in general geodesics in one frame are not geodesics in the other, null geodesics remain the same in both frames. It is a convenient result: the Newtonian potential of GR is sufficient to calculate the deflection of light, from which all weak lensing observables are derived.

Whether modifications to General Relativity are needed or not, gravitational lensing is a useful probe of cosmic structure. Below we summarize some basic equations of weak gravitational lensing, including a brief discussion of how this technique can be used to measure the masses of dark matter halos in the presence of statistical and systematic observational errors.

### 1.2.1 Lensing Geometry

Let $\Phi$ again be the Newtonian potential of a massive "lens," such as a galaxy or dark matter. It can be shown, e.g., in Carroll (11) Section 7.3, that the angle by which background light is deflected by this lens is

$$\vec{\hat{\alpha}} = \frac{2}{c^2} \int \vec{\nabla}_\perp \Phi \, \mathrm{d}r_{\mathrm{los}} \,, \tag{1.27}$$

where $\vec{\nabla}_\perp$ is the gradient perpendicular to the velocity vector of the photon.

For a point source, the potential is given by

$$\Phi(R, r_{\mathrm{los}}) = -\frac{GM}{(R^2 + r_{\mathrm{los}}^2)^{1/2}} \tag{1.28}$$

where $R$ is the impact parameter and $r_{\mathrm{los}}$ parameterizes the path of the light, approximated by the undeflected path. The deflection angle is then

$$\hat{\alpha} = \frac{4GM}{c^2 R} \tag{1.29}$$

A fuller picture of the relevant geometry is shown in Fig. 1.3: for this figure and the following discussion, we mostly follow the conventions of Narayan & Bartelmann (91). The impact parameter has a magnitude given by

$$R = D_{\mathrm{L}} \theta \,, \tag{1.30}$$

where $\theta$ is the observed angular distance between the lens and source (in radians) and $D_{\mathrm{L}}$ is the distance between the observer and the lens. Distances defined such that this arc-length formula holds are termed "angular diameter distances." Likewise, $D_{\mathrm{s}}$ and $D_{\mathrm{Ls}}$ are the angular diameter distances from the observer to the source and from the lens to the source, respectively. For more discussion of these and other distance measures used in cosmology, see, e.g., Hogg (44).

The observed source position $\vec{\theta}$ is the angle on the sky at which the observer sees the background source galaxy. The lensing deflection has obscured the true source position, $\vec{\beta}$. These two angles are related through the lens equation

$$\vec{\beta} = \vec{\theta} - \vec{\alpha}\,, \tag{1.31}$$

where $\vec{\alpha}$ is the "reduced" deflection angle. Since the triangle defined by the true source position, angle $\vec{\hat{\alpha}}$, and observed position shares a side with that defined by the true position, angle $\vec{\alpha}$, and observed position, and both angles are small, they are related by

$$\vec{\alpha} = \frac{D_{\rm Ls}}{D_{\rm s}}\vec{\hat{\alpha}}\,. \tag{1.32}$$

### 1.2.2 Relating true and observed images

In order to use the shapes of background sources to learn something about the intervening matter, we need to relate their true and observed images. This mapping is given by asking how small changes in the observed position, $\vec{\theta}$, relate to small changes in the true position $\vec{\beta}$:

$$\frac{\partial\beta_i}{\partial\theta_j} = \frac{\partial}{\partial\theta_j}(\theta_i - \alpha_i) \tag{1.33}$$

$$= \delta_{ij} - \frac{\partial\alpha_i}{\partial\theta_j} \tag{1.34}$$

$$\equiv \delta_{ij} - \frac{\partial}{\partial\theta_j}\left(\frac{\partial\psi}{\partial\theta_i}\right) \tag{1.35}$$

where we have defined a lensing potential $\psi$ whose gradient with respect to $\theta$ is the reduced deflection angle,

$$\vec{\nabla}\psi \equiv \vec{\alpha}\,. \tag{1.36}$$

The functional form of this lensing potential is then

$$\psi(\vec{\theta}) = \frac{2}{c^2}\frac{D_{\rm Ls}}{D_{\rm L}D_{\rm s}}\int \Phi(D_{\rm L}\vec{\theta}, r_{\rm los})\,{\rm d}r_{\rm los}\,, \tag{1.37}$$

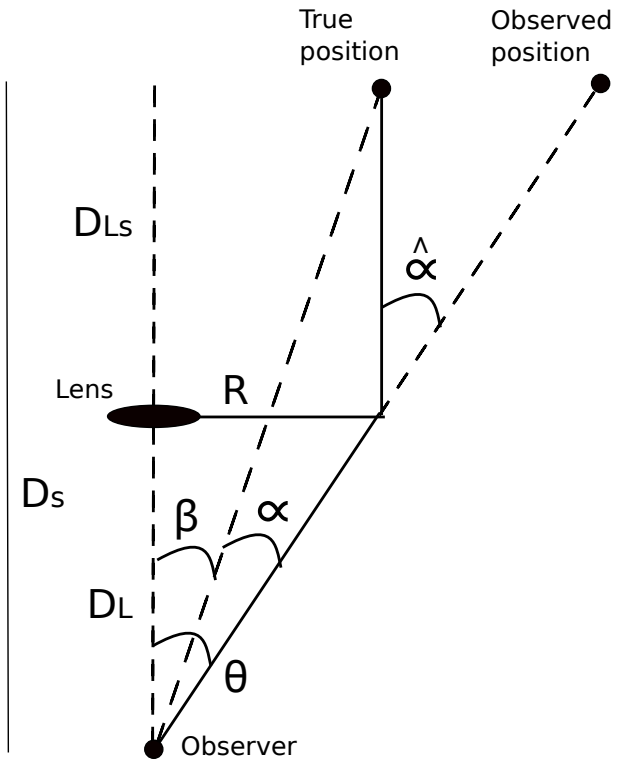


**Figure 1.3:** The trajectory of a photon moving near a massive object is deflected by an angle $\hat{\alpha}$. The light was emitted by a source galaxy observed at an angle $\theta$ from the lens, but with true position $\beta$. These angles are related by the angular diameter distances between observer, lens, and source.

as can be shown:

$$\vec{\nabla}_\theta \psi = D_{\rm L} \vec{\nabla}_R \psi \tag{1.38}$$

$$= \frac{D_{\rm Ls}}{D_{\rm s}} \frac{2}{c^2} \int \vec{\nabla}_R \Phi(\vec{R}, r_{\rm los})\, {\rm d}r_{\rm los} \tag{1.39}$$

$$= \frac{D_{\rm Ls}}{D_{\rm s}} \vec{\hat{\alpha}}\,. \tag{1.40}$$

Linear combinations of derivatives of $\psi$ describe the change in shape of background source galaxies. One effect is magnification, an isotropic stretching of the galaxy light, but we will focus on anisotropic stretching, or "shear." In a Cartesian coordinate system, the two components of shear are

$$\gamma_1 = \frac{1}{2}\left(\frac{\partial^2 \psi}{\partial \theta_1^2} - \frac{\partial^2 \psi}{\partial \theta_2^2}\right) \tag{1.41}$$

$$\gamma_2 = \frac{\partial^2 \psi}{\partial \theta_1 \partial \theta_2}\,. \tag{1.42}$$

Gravitational lensing causes a shear of the background source which is tangential to the line joining the lens and source. Shear in the tangential coordinate system relative to the above Cartesian shears is

$$\gamma_t(\vec{\theta}) = -\gamma_1(\vec{\theta}) \cos(2\phi) - \gamma_2(\vec{\theta}) \sin(2\phi)\,, \tag{1.43}$$

where $\phi$ is the angle between the x-axis of the Cartesian coordinate system and the line joining this particular lens-source pair. The cross-component,

$$\gamma_\times(\vec{\theta}) = \gamma_1(\vec{\theta}) \sin(2\phi) - \gamma_2(\vec{\theta}) \cos(2\phi)\,, \tag{1.44}$$

describes shears that are at 45° to the tangential line. This component is not generated gravitationally by single deflections, but can be generated by errors in the shape measurement procedure. Thus it serves as a useful test of systematics.

### 1.2.3 Lensing signal of dark matter halos

The excess surface density $\Delta\Sigma$ is a useful quantity, as it connects the direct observable $\gamma_t(\theta)$ to the 3D density $\rho(r)$. On one side, we have

$$\Delta\Sigma(R) = \Sigma_{\rm cr}(D_{\rm L}, D_{\rm s})\,\gamma_t(R)\,, \tag{1.45}$$

where the proportionality factor $\Sigma_{\rm cr}$ determines the strength of the lensing; this critical surface density is given by

$$\Sigma_{\rm cr} = \frac{c^2}{4\pi G}\frac{D_s}{D_l D_{ls}}\,. \tag{1.46}$$

And on the other side, the connection to the 3D density is

$$\Delta\Sigma = \bar{\Sigma}(<R) - \Sigma(R) \tag{1.47}$$

where the surface density is an integral over the 3D density,

$$\Sigma(R) = \int_{-\infty}^{\infty} \rho(r = \sqrt{\chi^2 + R^2}) d\chi\,, \tag{1.48}$$

and the average of the surface density inside projected radial distance $R$ is

$$\begin{aligned} \bar{\Sigma}(<R) &= \frac{\int\int \Sigma(R')d^2R'}{\int\int d^2R'} \\ &= \frac{2}{R^2}\int_0^R \Sigma(R')R'dR'\,, \end{aligned} \tag{1.49}$$

for the case of a circularly symmetric mass distribution.

Motivated by N-body simulation results (92), we can take a density which follows the NFW profile

$$\rho(r) = \frac{4\rho_{\rm s}}{r/r_{\rm s}(1 + r/r_{\rm s})^2}\,, \tag{1.50}$$

fully determined by two parameters, the scale radius $r_{\rm s}$ and density $\rho_{\rm s}$. An equivalent and common parameter set is the halo mass, $M_{\rm vir}$ (with associated $R_{\rm vir}$), and concentration, $c = R_{\rm vir}/r_s$. The left panel of Fig. 1.4 shows the excess surface density for halos of mass

$M_{\rm vir} = 10^{12}, 10^{13}, 10^{14} M_\odot/h$: it is a strong function of halo mass. Coincidentally, the peaked 3D density profile of dark matter halos results in a similar radial shape for the lensing observable. In chapter 5, we will show that this is not the case for dark matter voids.

### 1.2.4 Statistical and systematic errors

A model fitting approach can be used to obtain the mass and concentration by varying the 3D profile of Eq. (2.11) to produce the $\Delta\Sigma(R)$ profile best matched to the weak lensing observable $\gamma_t$. However, this also requires an accurate uncertainty on measurements at each radial bin. The dominant uncertainty at small scales is given by shape noise, the intrinsic ellipticity of source galaxies. This ellipticity is indistinguishable from the lensing effect, except for its random orientation, allowing a statistical measurement in which the random noise, initially hundreds of times larger than the signal, is decreased below the level of the gravitational shear by stacking many lens-source pairs. The noise is

$$\sigma_{\gamma_t} = \frac{\sqrt{\sigma^2_{\rm shape} + \sigma^2_{\rm m}}}{\sqrt{N_{\rm pair}}} \approx \frac{0.3}{\sqrt{N_{\rm pair}}} \tag{1.51}$$

per radial bin. The rms intrinsic ellipticity of 0.3 is beat down by the number of lens-source pairs per bin,

$$\begin{aligned} N_{\rm pair} &= N_{\rm lens} \times N_{\rm source} \\ &= \left( (\text{Volume}) \left.\frac{dn}{dm}\right|_{z_l} \right) \times \left( n_{\rm source} \pi (R_i^2 - R_{i-1}^2) \right) \end{aligned} \tag{1.52}$$

where $R_i, R_{i+1}$ label the bin edges, $n_{\rm source}$ is the surface density of background sources, and $\mathrm{d}n/\mathrm{d}m$ is the halo mass function. The uncertainty in the excess surface density

$$\sigma_{\Delta\Sigma} = \Sigma_{\rm cr} \sigma_{\gamma_t} \tag{1.53}$$

depends also on the critical surface density.

In order to give some sense of the S/N we reference a particular experiment. The Dark Energy Survey (DES) will cover 5,000 square degrees of the southern sky to a limiting magnitude of $i < 24$, several magnitudes deeper than current comparable surveys such as Sloan Digital Sky Survey (SDSS). Given this limiting magnitude, DES should find all lenses down to a halo mass $M_{\rm halo} \sim 10^{12} M_\odot/h$ in the redshift interval $0.2 < z < 0.4$. We integrate over the mass function between $11.8 < \log_{10}(M_{\rm halo} \times h/M_\odot) < 12.2$ and multiply by the volume between $0.2 < z < 0.4$ to obtain the number of lenses. For the sources we take an effective source redshift of $z_s = 0.75$, and source density of $n_{\rm source} = 10$ per sq. arcmin to obtain the number of sources, $N_{\rm source}$, in Eq. (1.52). In the right panel of Fig. 1.4 we show the S/N ratio for these $\sim 10^{12} M_\odot/h$ size lenses (dot-dashed line). The result is also shown for two orders of magnitude higher in halo mass, each time integrating the mass function over an interval $\log_{10}(M_{\rm halo}) \pm 0.2 \log_{10}(M_{\rm halo})$.

However, these S/N estimates are extremely optimistic in that there are other factors which increase the variance significantly, and can even systematically bias the signal. Determining lens and source galaxy redshifts using only the five DES filters results in large uncertainty in the line-of-sight distance to these galaxies. That uncertainty translates into increased scatter and possibly bias through the scaling of $\gamma_t$ to $\Delta\Sigma$ based on the redshift dependence of $\Sigma_{\rm cr}$. In addition, these line-of-sight distance errors may affect distance assumptions and therefore luminosity determination, leading to error in the halo sizes in the stacked measurement. However, even with true redshift information, there is an intrinsic mass-luminosity scatter in the way galaxies occupy dark matter halos. This scatter, whether intrinsic or due to photometric redshifts, makes it more difficult to interpret the halo masses obtained from the tangential shear profiles.

A number of other effects are worth mentioning. For example, lens variance such as scatter in the concentration-mass relation will affect small scales more strongly than large scales. At the image level of estimating source galaxy ellipticities, issues such as deblending and sky subtraction can bias the estimates. Intrinsic alignments of satellite galaxies with

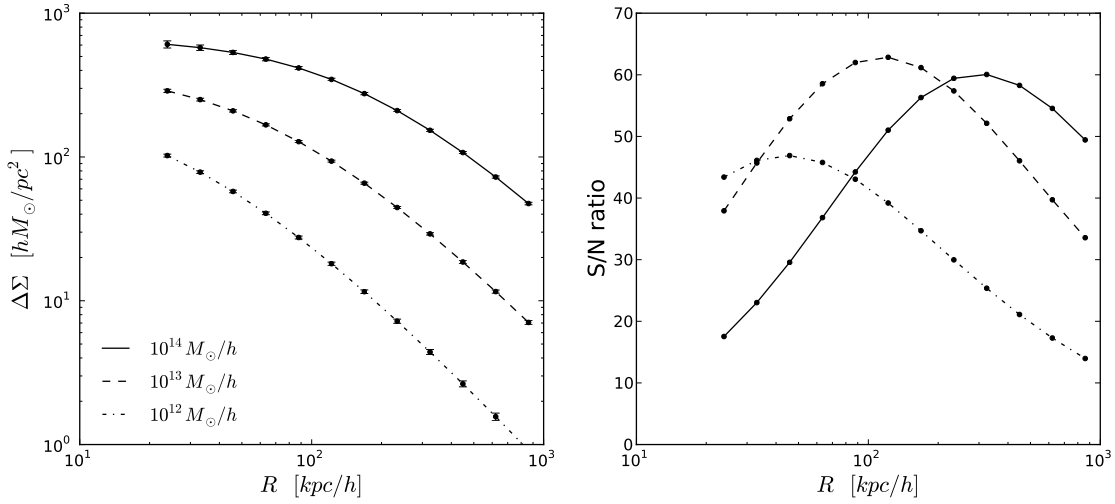


**Figure 1.4:** Signal-to-noise ratio for $M = 10^{14}, 10^{13}$, and $10^{12} M_\odot/h$ halos. Based on an estimate of the DES magnitude limit, we expect to find all halos of these masses within redshifts of 0.2 and 0.4; this redshift range, along with the DES survey area of 5000 sq. deg., gives the volume needed to estimate the number of stacked lenses. The effective lens and source redshifts are $z_l = 0.3$ and $z_s = 0.75$, while source density is 10 per sq. arcmin.

centrals have been measured; these can bias galaxy-galaxy lensing if some supposed background sources are actually satellites of the lens galaxy. Assuming the brightest galaxy in a cluster or group is at the center of the dark matter halo can also lead to decreased signal, since stacking tangential shears around some point other than the center smooths out the observed profile. The NFW profile used above is motivated by dark matter simulations, but baryons in the form of stars and gas also contribute to the total mass and therefore lensing profile. Finally, uncertain cosmology can also cause some error due to the dependence of distances on dark energy parameters.

These systematics and others have been considered by, e.g., Mandelbaum et al. (78) and Sheldon et al. (118), which obtain masses of dark matter halos using SDSS data. In chapter 4 we move away from the simpler, spherically-symmetric lensing signal of halos to measure

lensing from dark matter filaments in SDSS. However, the above basics of weak lensing data analysis, such as accounting for statistical and systematic errors, are still very relevant. And finally, in chapter 5 we measure the minute gravitational lensing signal of voids in SDSS, in the process developing a new void finder optimized for lensing purposes.

# Chapter 2

# Halo Scale Predictions of Symmetron Modified Gravity

## 2.1 Introduction

The observed acceleration in the expansion of the universe can arise from a dark energy component or from a departure of gravity from general relativity (GR) on cosmological scales. One way to distinguish between the two possibilities is to consider the growth of perturbations. For modified gravity (MG) theories, the relation of the expansion history to the growth of perturbations is specific to every model. In the quasi-static, Newtonian linear regime, several authors have parameterized the growth of perturbations with $g(k,z) \equiv G/G_N$ and $\eta(k,z) \equiv \psi/\phi$ (e.g. (55, 142)).

Laboratory and solar system constraints (see (138) and references therein) require any viable MG theory to have some mechanism by which it mimics the predictions of GR within Milky Way-size halos. Such "screening" mechanisms (see (56) for a review) generally determine the deviations from GR based on the local density: in high density environments the scalar force is suppressed, while in low density environments it can be of approximately gravitational strength. Two such mechanisms have been extensively studied in the literature:

the chameleon screening (63) of $f(R)$ theories (12, 52, 96) and Vainshtein screening (133) of higher dimensional (e.g., Dvali-Gabadadze-Porrati (DGP) gravity (27)) and Galileon models (94). Recent work has included detailed simulations which are necessary because of the nonlinearity inherent in how GR is recovered inside the Milky Way (14, 113).

In this work we explore the symmetron model of (42) (see also (99) and (107)), which exploits a novel screening mechanism similar in part to chameleon screening but with key differences. The symmetron has a vacuum expectation value (VEV) that is large in low density environments and small in high density environments. Symmetron screening then relies on a coupling to matter that is proportional to the VEV, thus suppressing the scalar force in high density environments. Recent work has focused on symmetron cosmology, including the evolution of the symmetron field through various cosmological epochs (43), as well as its effect on linear (5) and nonlinear (25) structure formation.

Tests of gravity on linear scales have some limitations. The $g, \eta$ parameterization is only valid on scales smaller than the superhorizon regime and larger than the nonlinear regime. At high redshift there is a different problem: since MG models recover GR at high redshift for consistency with CMB and Nucleosynthesis observations, effects of enhanced forces are manifested only at late times. Thus, even if observations are made late enough to be within the MG era, the signal has had limited time to accumulate.

In this study we consider tests on scales within and outside virial radii of dark matter halos modeled with the Navarro-Frenk-White (NFW) (92) profile. In this regime the predicted deviations due modified gravity can be significantly larger than in the linear regime (measurement errors and systematic uncertainties need to be taken into account but will not be considered here). As highlighted by (53) and (57), astrophysical tests in this regime can provide effective tests of chameleon theories. We will calculate the predicted deviations for symmetron theories.

In § II we describe the symmetron theory and our method for calculating modified forces around NFW halos. § III contains our isolated halo results as well as a comparison of the

various screening mechanisms. In § IV we model and show results for forces on test particles in two-body host-satellite systems. We conclude in §V.

## 2.2 Force profiles of NFW halos

### 2.2.1 Symmetron theory

In the Einstein frame we can describe the gravitational forces as GR with an additional "fifth force," mediated by the symmetron field, $\phi$. For GR we have the usual Poisson equation: $\nabla^2\Psi_{\rm N} = 4\pi G\rho$, leading to

$$|F_{\rm N}| = \frac{{\rm d}\Psi_{\rm N}}{{\rm d}r} = \frac{GM(<r)}{r^2}\,. \tag{2.1}$$

The symmetron equation of motion in the presence of non-relativistic matter (42) is

$$\Box\phi = \frac{\partial V}{\partial\phi} + \rho\frac{\partial A}{\partial\phi} \equiv \frac{\partial}{\partial\phi}V_{\rm eff}\,, \tag{2.2}$$

where

$$V(\phi) = -\frac{1}{2}\mu^2\phi^2 + \frac{1}{4}\lambda\phi^4\,, \tag{2.3}$$

and

$$A(\phi) = 1 + \frac{\phi^2}{2M_{\rm s}^2} + \mathcal{O}\left(\frac{\phi^4}{M_{\rm s}^4}\right)\,. \tag{2.4}$$

Note that the relevant field range is $\phi \ll M_{\rm s}$, such that any $\mathcal{O}(\phi^4/M_{\rm s}^4)$ terms in $A(\phi)$ can be consistently neglected. The potential $V(\phi)$ comprises the most general renormalizable form invariant under the $\mathbb{Z}_2$ symmetry $\phi \to -\phi$. The coupling to matter $\sim \phi^2/M_{\rm s}^2$ is the leading such coupling compatible with the symmetry. The model involves two mass scales, $\mu$ and $M_{\rm s}$, and one positive dimensionless coupling $\lambda$. The mass term is tachyonic, so that the $\mathbb{Z}_2$ symmetry $\phi \to -\phi$ is spontaneously broken. The effective potential of eq. (2.2) is

$$V_{\rm eff}(\phi) = \frac{1}{2}\left(\frac{\rho}{M_{\rm s}^2} - \mu^2\right)\phi^2 + \frac{1}{4}\lambda\phi^4\,. \tag{2.5}$$

Whether the quadratic term is negative or not, and hence whether the $\mathbb{Z}_2$ symmetry is spontaneously broken or not, depends on the local matter density.

The screening mechanism works roughly as follows: in vacuum or in large voids, where $\rho \simeq 0$, the potential breaks reflection symmetry spontaneously, and the scalar acquires a VEV $|\phi| = \phi_0 \equiv \mu/\sqrt{\lambda}$; in regions of high density, such that $\rho > M_{\rm s}^2\mu^2$, the effective potential no longer breaks the symmetry, and the VEV goes to zero. Meanwhile, to lowest order the symmetron-matter coupling is $\sim \rho\phi^2/M_{\rm s}^2$. Fluctuations $\delta\phi$ around the local background value $\phi_{\rm VEV}$, which would be detected by local experiments, couple to density as

$$\sim \frac{\phi_{\rm VEV}}{M_{\rm s}^2}\delta\phi\ \rho\,. \tag{2.6}$$

In particular, the coupling is proportional to the local VEV. In high-density environments where the symmetry is restored, the VEV should be near zero and fluctuations of $\phi$ do not couple to matter. In less dense environments, where $\rho < M_{\rm s}^2\mu^2$ and the symmetry is broken, the coupling turns on.

For a static-spherically symmetric source, eq. (2.2) becomes

$$\frac{{\rm d}^2\phi}{{\rm d}r^2} = -\frac{2}{r}\frac{{\rm d}\phi}{{\rm d}r} + \left(\frac{\rho}{M_{\rm s}^2} - \mu^2\right)\phi + \lambda\phi^3\,. \tag{2.7}$$

We set the parameters as in (42): $M_{\rm s} = 10^{-3}M_{\rm Pl}$ satisfies solar system constraints while still allowing for order unity deviations elsewhere. Also, $\mu = \sqrt{\rho_c}/M_{\rm s}$ and $\lambda = (\mu/\phi_0)^2$, where $\rho_c$ is the average cosmological density today and $\phi_0$ is the background value of the field. Note that these parameter choices correspond to $\mu \sim {\rm Mpc}^{-1}$, constraining symmetron effects to $\sim$ Mpc distances.

As in (43), the symmetron-mediated force $F_\phi$ relative to the Newtonian force $F_{\rm N}$ between two test masses in vacuum is set by the symmetry-breaking value $\phi_0$:

$$\frac{F_\phi}{F_{\rm N}} = 2M_{\rm Pl}^2\left(\frac{{\rm d}\ln A}{{\rm d}\phi}\bigg|_{\phi_0}\right)^2 \simeq 2\left(\frac{\phi_0 M_{\rm Pl}}{M_{\rm s}^2}\right)^2\,. \tag{2.8}$$

If the scalar-mediated force is to be comparable to gravity in vacuum, then we must impose $\phi_0/M_{\rm s}^2 \sim 1/M_{\rm Pl}$, that is,

$$\phi_0 \equiv \frac{\mu}{\sqrt{\lambda}} = g\frac{M_{\rm s}^2}{M_{\rm Pl}}\,, \tag{2.9}$$

where $g \sim \mathcal{O}(1)$. To be precise, it follows from eq. (2.8) that $g$ measures the strength of the scalar force in vacuum relative to gravity: $F_\phi = 2g^2 F_{\rm N}$. For comparison to $f(R)$ and DGP theories, for which the fifth force is at most $1/3$ $F_{\rm N}$, we will set $g = 1/\sqrt{6}$; otherwise we choose $g = 1$, which is still consistent with solar system tests, as shown in (42). Note that eq. (2.8) has no dependence on the test bodies involved. Extended mass distributions affect the scalar and Newtonian forces differently so that solving for the Newtonian potential and scalar field profile is required in order to evaluate the ratio. The ratio of forces on a test mass in the neighborhood of such an extended distribution is

$$\frac{F_\phi}{F_{\rm N}} = \frac{(\phi/M_{\rm s})(\nabla\phi/M_{\rm s})}{\nabla\Psi_{\rm N}}\,. \tag{2.10}$$

### 2.2.2 NFW halos

We consider gravitational forces in the neighborhood of NFW halos (92), whose density profiles are a good fit to those of stacked simulated halos. The (untruncated) density is

$$\rho_{\rm NFW}(r) = \frac{4\rho_{\rm s}}{\frac{r}{r_{\rm s}}\left(1+\frac{r}{r_{\rm s}}\right)^2}\,, \tag{2.11}$$

where $\rho_{\rm s}$ and $r_{\rm s}$ are parameters that depend on halo mass (see below). We define the mass $M_{300}$ of each halo as that enclosed within the virial radius, $R_{300}$. This is the radius at which the average density enclosed is 300 times the critical density $\rho_c$. The concentration connects the virial radius to the scale radius, $c = R_{300}/r_{\rm s}$. We take it to be a function of halo mass,

$$c = 9\left(\frac{M_{300}}{3.2\times10^{12}M_\odot/h}\right)^{-0.13}\,, \tag{2.12}$$

as found in (8). The mass and concentration definitions are chosen to allow comparison of our results with the chameleon model of (115). We note that the profile itself will change somewhat with the modified forces.

The mass enclosed within radius $r$ is

$$M(< r) = M_{300}\frac{F(c\, r/R_{300})}{F(c)}\,, \tag{2.13}$$

where $F(x) = \ln(1+x) - x/(1+x)$. We use eq. (2.13) in (2.1) to solve for the Newtonian force. In order to obtain the symmetron profile, it is useful to define a dimensionless scalar field, $\psi \equiv \phi/\phi_0$ whose equation of motion follows from eq. (3.28):

$$\frac{\mathrm{d}^2\psi}{\mathrm{d}r^2} = -\frac{2}{r}\frac{\mathrm{d}\psi}{\mathrm{d}r} + \left(\frac{\rho}{M_\mathrm{s}^2} - \mu^2\right)\psi + \mu^2\psi^3\,. \tag{2.14}$$

We obtain the radial profile by substituting eq. (2.11) in (2.14) with boundary conditions

$$\left.\frac{d\psi}{dr}\right|_{r=0} = 0, \quad \psi(r\to\infty) = 1\,. \tag{2.15}$$

We use a shooting algorithm to solve this nonlinear equation, tuning the boundary condition $\psi(r=0)$ such that the field stays within 1% of $\psi = 1$ at large $r$ for at least 25 virial radii. Note that Eqs. (2.14), (2.15) depend only on the theory parameters $\mu$ and $M_\mathrm{s}$; they are independent of $\phi_0$ and $\lambda$. The only effect of changing $\phi_0$ is to set the overall amplitude of the symmetron profile and therefore the amplitude of the ratio of forces.

For comparison to the work of (42) and as a check of our numerical solutions, we also solve for the force deviation in the case of a top-hat density profile

$$\rho_{\mathrm{top-hat}}(r) = \begin{cases}\rho_0, & r < R_\mathrm{vir}\\ 0, & r > R_\mathrm{vir}\,,\end{cases} \tag{2.16}$$

where $\rho_0 = 300\rho_\mathrm{c}$. For the top-hat profile, specifying the mass and density fixes $R_{300}$. To obtain an analytic solution, we approximate the symmetron equation of motion as quadratic

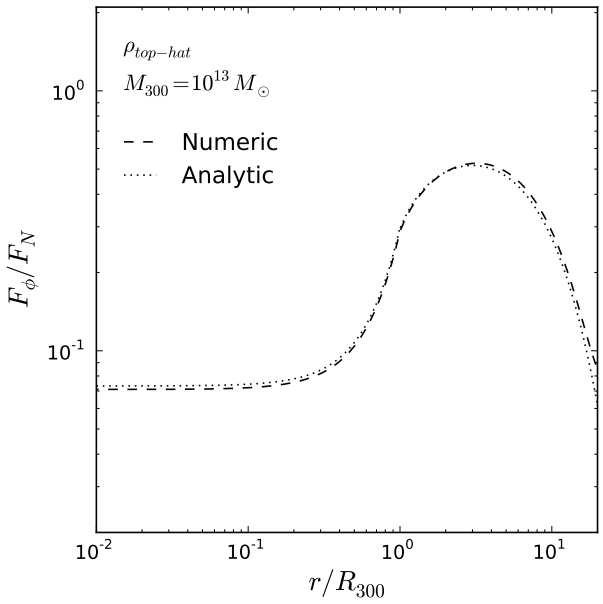


**Figure 2.1:** Force deviation $F_\phi/F_{\rm N}$ for a top-hat density profile of total mass $10^{13}M_\odot$ calculated numerically (dashed line) and analytically (dotted line). We find similar agreement between the two methods throughout the mass range $10^{10} - 2\times10^{14}M_\odot$.

around the appropriate minimum inside and outside the object (see (42) for details) resulting in

$$\begin{aligned} \phi_{\rm in}(r) &= A\frac{R}{r}\sinh\left(r\sqrt{\frac{\rho}{M_{\rm s}}-\mu^2}\right) \\ \phi_{\rm out}(r) &= B\frac{R}{r}e^{-\sqrt{2}\mu r}+\phi_0\,, \end{aligned} \tag{2.17}$$

and solve for $A$ and $B$ by matching at the boundary. The exact solution is obtained using our shooting algorithm as in the NFW case. Figure 2.1 shows the equivalence of these methods for a top-hat mass $10^{13}M_\odot$. We find similar agreement between the two methods throughout the mass range $10^{10}-2\times10^{14}M_\odot$.

We can define $\overline{\gamma}_{\rm vir}$ as an average of the force deviation over the virial radius of a halo (see (115) for details). This quantity can be determined from both theory and observations. From the theory we have calculated

$$\overline{\gamma}_{\rm vir}=\frac{\int r^3\rho(r)\,F_{\rm N}(1+F_\phi/F_{\rm N})\,dr}{\int r^3\rho(r)\,F_{\rm N}\,dr}\,, \tag{2.18}$$

where the integral is over the virial radius $R_{300}$. This is straightforward to compare to observations, which yield

$$\overline{\gamma}_{\rm vir}=(M_{300,\rm dyn}/M_{300})^{5/3}\,, \tag{2.19}$$

where $M_{300,\rm dyn}$ is a dynamical mass, and $M_{300}$ is the "true" or lensing mass.

As will be seen later, the deviation from GR is significant out to $\sim 10$ times the virial radius. Therefore we define a second average $\bar{\gamma}_d$ exactly as in eq. (2.18), except the integrals are taken over distances $d=0.5,\ 1,\ 4,$ and $10\ R_{300}$.

## 2.3 Results for isolated halos

Figure 2.2 shows the force deviation $F_\phi/F_{\rm N}$ on a test particle given by eq. (2.10) in the neighborhood of isolated NFW halos of various masses. Also pictured are the deviations

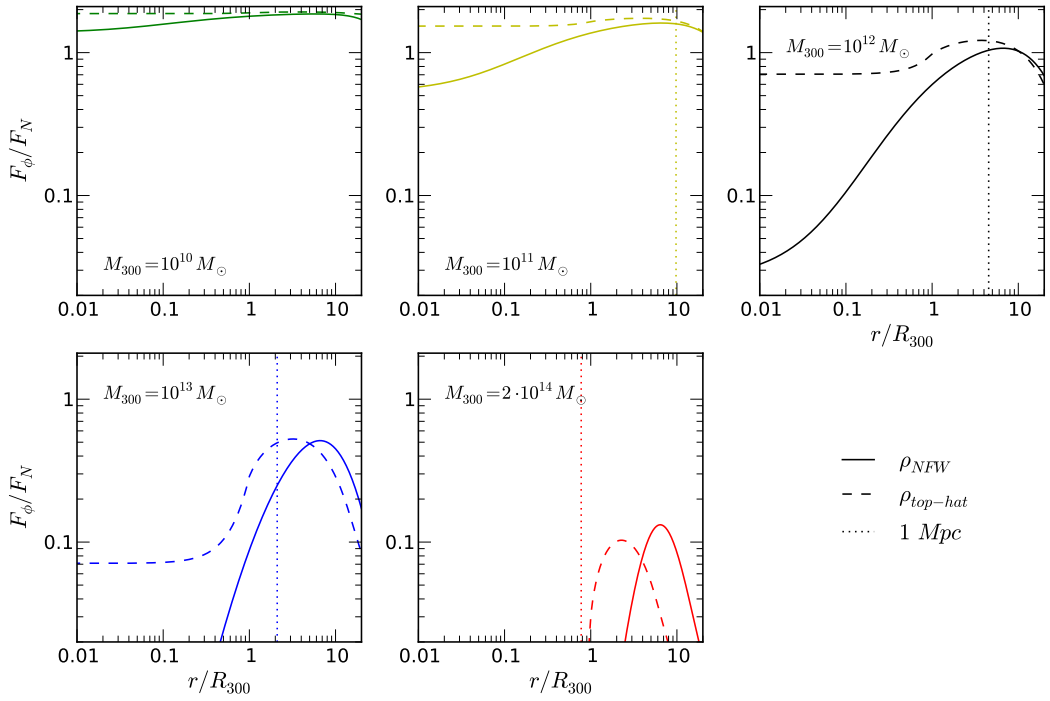


**Figure 2.2:** Ratio $F_\phi/F_{\rm N}$ of the symmetron mediated force to the GR force for halos of different masses with field symmetry breaking value $\phi_0 = M_{\rm s}^2/M_{\rm Pl}$ (i.e. $g = 1$). The halos are modeled with NFW (solid line) and spherical tophat (dashed line) profiles. Note that the ratio is plotted vs. radius in units of each halo's virial radius, $R_{300}$. The background compton wavelength, $\lambda_\phi \approx 1$ Mpc (vertical dotted line) gives a sense of the physical distance.

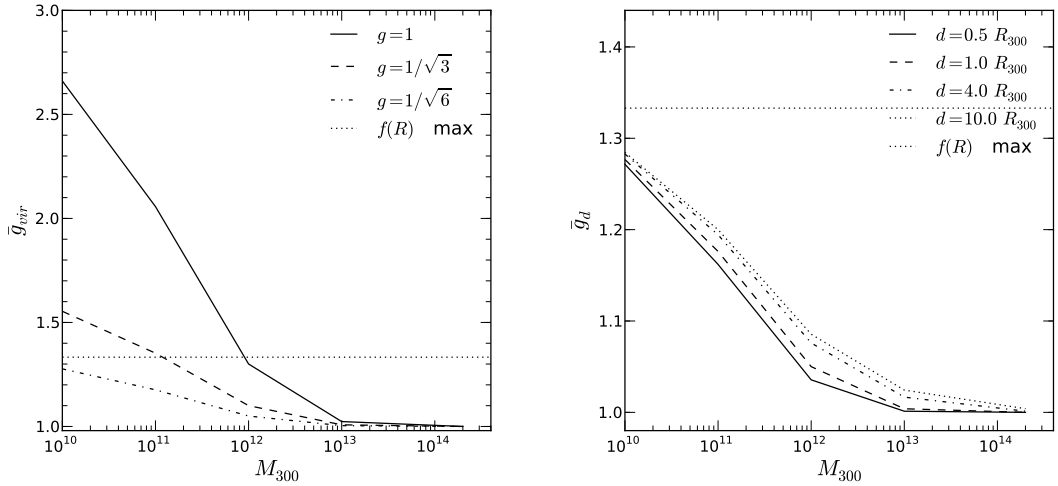


**Figure 2.3:** (*left panel*): Averaged force deviation, $\overline{\gamma}_{\rm vir}$, as a function of "true" or lensing mass for different values of the symmetry breaking field value, $\phi_0 = gM_{\rm s}^2/M_{\rm Pl}$. (*right panel*): A modified averaged force deviation for the smallest field value $g = 1/\sqrt{6}$. The average is taken over a distance $d$ from the center of the halo, with $d = 0.5,\ 1,\ 4$, and 10 $R_{300}$ from bottom. On both panels, the horizontal dotted line at 4/3 shows the maximum average for $f(R)$ modified gravity.

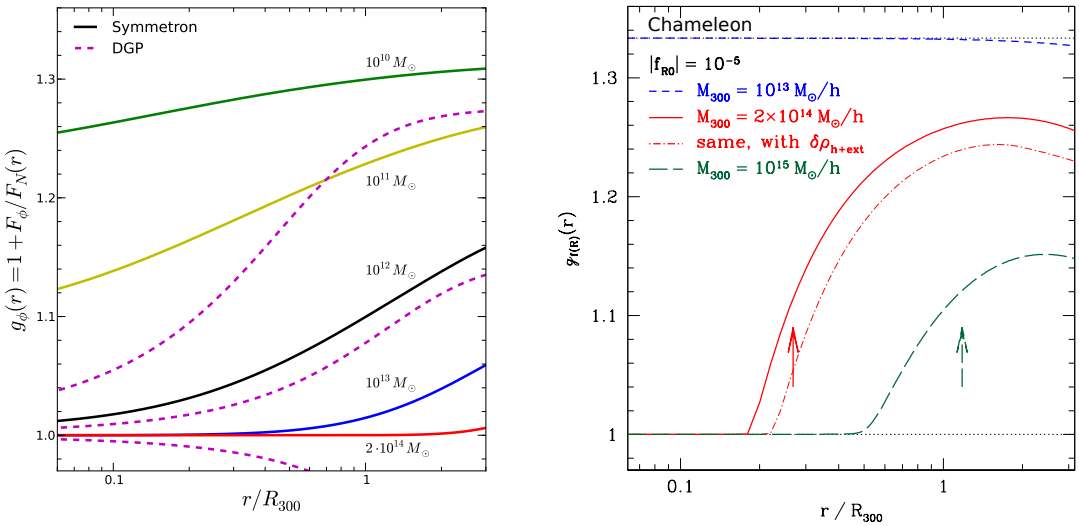


**Figure 2.4:** (*left panel*): Here we plot $\gamma_\phi \equiv 1 + F_\phi/F_{\rm N}$ for comparison with $\gamma_{f(R)}$ in (115). Solid curves are from our symmetron model with $\phi_0 = M_{\rm s}^2/\sqrt{6}M_{\rm Pl}$. Dashed curves are from normal branch DGP with crossover radius $r_c = 500$ Mpc, $r_c = 3100$ Mpc, and self-accelerating DGP, from top to bottom. (*right panel*): Reproduced from (115). Force deviation for Hu-Sawicki $f(R)$ around NFW halos. Arrows denote the radius where the chameleon thin-shell condition is first met. See (115) for details of the DGP and $f(R)$ models. We see that the three types of screening predict distinct transitions in $F_\phi/F_{\rm N}$ with respect to both radius and mass (see text for details).

for constant density spheres of the same mass. We plot using the symmetron vacuum value $\phi_0 = M_s^2/M_{\rm Pl}$, but as argued in section 2.2, letting $\phi_0 \to g\phi_0$ simply shifts these curves down by a factor $g^2$. For all but the smallest halos ($10^{10} M_\odot$), the two profiles give significantly different results all the way out to the virial radius $R_{300}$.

In the left panel of figure 2.3, we plot $\overline{\gamma}_{\rm vir}$ given by eq. (2.18) for three values of the symmetron vacuum value: $\phi_0 = g M_s^2/M_{\rm Pl}$ with $g = 1, 1/\sqrt{3}, 1/\sqrt{6}$. Setting $g = 1/\sqrt{6}$ fixes the max deviation at 4/3 as in $f(R)$ and DGP theories. Equation (2.18) implies $M_{\rm dyn,300} = \overline{\gamma}_{\rm vir}^{3/5} M_{300}$ so that the symmetron theory predicts, e.g., the dynamical mass of a $10^{11} M_\odot$ halo to be 50%, 25%, or 10% greater than the lensing mass for the three pictured values of $g$.

The right panel of figure 2.3 shows the same average taken out to larger radii $d \times R_{300}$, corresponding to 0.5, 1, 4, and 10 times the halo's virial radius. Although the peak deviations in figure 2.2 are at approximately 7 $R_{300}$, the weighting by density in the integral of eq. (2.18) results in a relatively small increase in $\overline{\gamma}_{\rm vir}$ with $d$ for a given halo.

In figures 2.4 we collect results for screening in the symmetron, DGP, and chameleon theories. The DGP and chameleon results are from (115). The left panel overlays our symmetron results (setting $g = 1/\sqrt{6}$) with three DGP models exhibiting Vainshtein screening. These are normal branch DGP with crossover radius $r_c = 500$ Mpc, $r_c = 3000$ Mpc, and self-accelerating DGP. The right panel of figure 2.4 shows chameleon screening in the $f(R)$ model of (52) with field cosmological value $|f_{R0}| = 10^{-5}$. We refer the reader to (115) for further details of these theories.

The "thin-shell" effect (63) of the chameleon, in which only a thin shell at the edge of a screened object contributes to the fifth force, is evident in the rapid rise of the force deviations from zero to their peak at $r \approx 2R_{300}$. In contrast, partially screened halos in the symmetron model show nonzero deviations at smaller radii that increase all the way to $\sim 7R_{300}$ before declining back to zero (see figure 2.2 for the large $r$ behavior). DGP models

also show nonzero deviations that increase beyond $2R_{300}$, eventually approaching a constant value.

The transition of the force deviations with halo mass also shows promise for distinguishing between the three screening mechanisms. For concreteness, consider the deviations at the virial radius $R_{300}$. For the chameleon background field value $|f_{R0}| = 10^{-5}$ ($10^{-6}$), a $10^{16}M_\odot$ ($10^{15}M_\odot$) halo shows no deviation while a $10^{13}M_\odot$ ($10^{12}M_\odot$) halo exhibits the maximum allowable deviation of 4/3. All smaller halos will likewise show a 4/3 deviation. In contrast, the symmetron $2 \times 10^{14}M_\odot$ halo is completely screened at $R_{300}$ while the deviation is only maximized at 4/3 for dwarfs of mass $\lesssim 10^9 M_\odot$. Thus, the degeneracy in the deviation exhibited between smaller halos in the chameleon model is not present in the symmetron. Furthermore, DGP models show no dependence on halo mass. These arguments imply that probes of modified forces spanning the mass range $10^9 - 10^{14}M_\odot$ would be effective at distinguishing between all three types of screening.

Simulations of $f(R)$ (114, 143) and symmetron (25) gravity show little evidence for large changes in halo concentration. However, the simulations of (2) show that for some models of interacting dark energy with a scalar fifth force, halo concentrations can be up to a factor of two larger or smaller than for comparable halos in ΛCDM. Furthermore, none of the above simulations resolve halos smaller than $\sim 10^{12}M_\odot$, for which the fifth force is most likely to cause a change in the density profile. We therefore conclude our study of single-halo solutions by considering the changes in $F_\phi/F_{\rm N}$ resulting from concentrations $c_{\rm min} \equiv c\,/\,2$ and $c_{\rm max} \equiv 2\,c$, where $c$ is our fiducial concentration given by Eq. (2.12).

The results for a $10^{11}M_\odot$ halo are shown in figure 2.5. This particular halo mass shows our largest changes in $F_\phi$, reaching $\pm 20\%\, F_{\rm N}$ relative to our fiducial concentration model in the innermost parts of the halo ($r \approx 0.01\, R_{300}$). However, even for this most extreme example the deviations fall to the few % level by $\sim 0.2\, R_{300}$. While smaller halos show slightly lesser changes with concentration, we find that for masses $\geq 10^{12}M_\odot$ the increase or decrease is at most $\approx 5\%\, F_{\rm N}$.

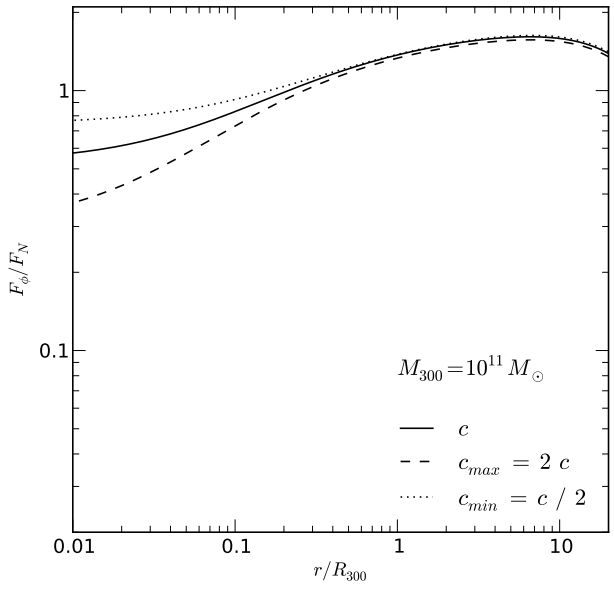


**Figure 2.5:** Force deviation $F_\phi/F_\mathrm{N}$ for three different halo concentrations: our fiducial choice $c$ given by Eq. (2.12) (solid line), a maximum variation $c_\mathrm{max} = 2c$ (dashed), and a minimum variation $c_\mathrm{min} = c\,/\,2$ (dotted). Although we have used extreme changes in the concentration and plotted the deviations for the halo most susceptible to such changes ($10^{11}\,M_\odot$), the difference in $F_\phi$ is less than $10\%\,F_\mathrm{N}$ for most of the extent of the halo.

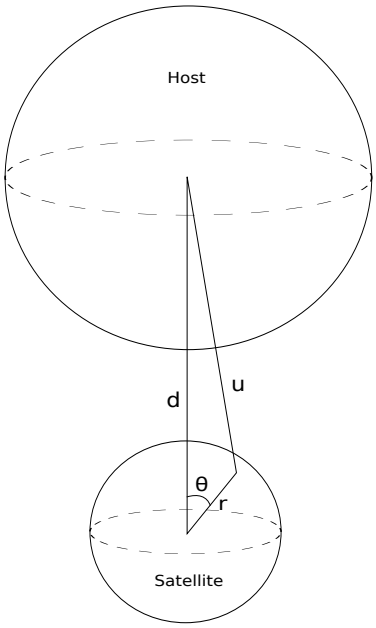


**Figure 2.6:** We average the host density in spherical shells about the satellite's center. The parameter $d$ is the center-to-center distance between the halos, $r$ is the standard radial coordinate, $\theta$ is the azimuthal angle, and $u^2 = d^2 + r^2 - 2dr\cos\theta$.

## 2.4 Host-satellite effects

### 2.4.1 Model

We now consider the force deviation that would be experienced by a test mass in the neighborhood of a satellite halo which is itself blanket screened by a nearby host. We model host and satellite with NFW profiles as before, determined by Eqs. (2.11), (2.12). To preserve spherical symmetry, we approximate the host profile by averaging its density in spherical

shells around the satellite location. See figure 2.6. Thus, for the average host profile we have

$$\begin{aligned}\langle\rho_{\rm h}\rangle(r) &= \frac{1}{4\pi}\int \mathrm{d}\Omega\ \rho_{\rm host}(u(r,d,\theta)) \\ &= \frac{1}{2}\int_0^\pi \mathrm{d}\theta \sin\theta \frac{4\rho_{\rm s}}{\frac{u}{r_{\rm s}}(1+\frac{u}{r_{\rm s}})^2} \\ &= \begin{cases} \frac{4\rho_{\rm s} r_{\rm s}^3/d}{(d+r_{\rm s})^2-r^2}, & 0 \le r \le d \\ \frac{4\rho_{0,{\rm s}} r_{\rm s}^3/r}{(r+r_{\rm s})^2-d^2}, & d \le r\,, \end{cases} \end{aligned} \tag{2.20}$$

where $u^2 = d^2 + r^2 - 2dr\cos\theta$, $d$ is the center-to-center distance between the halos, and $\theta$ is the azimuthal angle. Averaging the satellite density $\rho_{\rm sat}$ around its own center leaves its own NFW profile unchanged. We insert the total density

$$\rho = \rho_{\rm sat} + \langle\rho_{\rm h}\rangle \tag{2.21}$$

in eq. (2.14) with the boundary conditions (2.15), yielding the radial symmetron profile. The Newtonian force is given by integrating the profile eq. (2.20) in spherical shells to find the enclosed mass (see appendix A). We note that this averaged density profile will slightly overestimate (underestimate) the force deviation $F_\phi/F_{\rm N}$ on the side of the satellite nearer to (farther from) the host.

Figure 2.7 shows the density profile of a cluster-size ($2\times10^{14}M_\odot$) host modeled by eq. (2.20), an NFW satellite, and their sum, for two host-satellite separation $d = 1$ and $2\ R_{\rm host}$. In the inner parts of the satellite its own NFW profile dominates the total density, while the host profile is a slowly increasing function of $r$. At $r \sim R_{\rm sat}$ the averaged host density becomes the dominant component. After the cusp, which occurs at the host center we see the host density rapidly transitions to the NFW $\rho \propto 1/r^3$ power law. The pictured density profile is qualitatively similar for all relevant satellite and host masses.

### 2.4.2 Results

The cluster's screening effect on the satellite is evident in figure 2.8. At low radii the force deviation $F_\phi/F_{\rm N}$ for the total density profile has a similar slope to that of the isolated

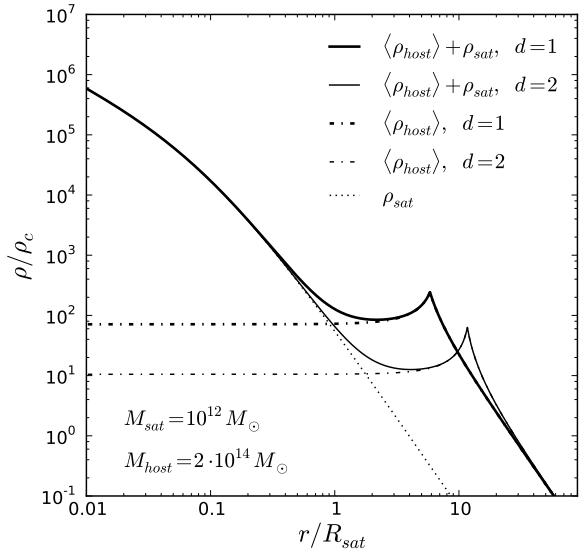


**Figure 2.7:** Host-satellite density profile as a function of radius in units of the *satellite's* virial radius, centered at the satellite's location. Pictured are the NFW satellite profile (dotted), averaged host profile given by eq. (2.20) (dot-dashed), and the sum of host and satellite components (solid). The latter two curves are shown for host-satellite separation $d = 1R_{\rm host}$ (thick lines) and $d = 2R_{\rm host}$ (thin lines). In each case, the cusp in the total profile is located at the separation distance $d$. This plot assumes $M_{\rm sat} = 10^{12}M_\odot$ and $M_{\rm host} = 2 \times 10^{14}$, although the profile is qualitatively similar for all relevant satellite and host masses. The host density becomes the dominant component at $r \sim R_{\rm sat}$.

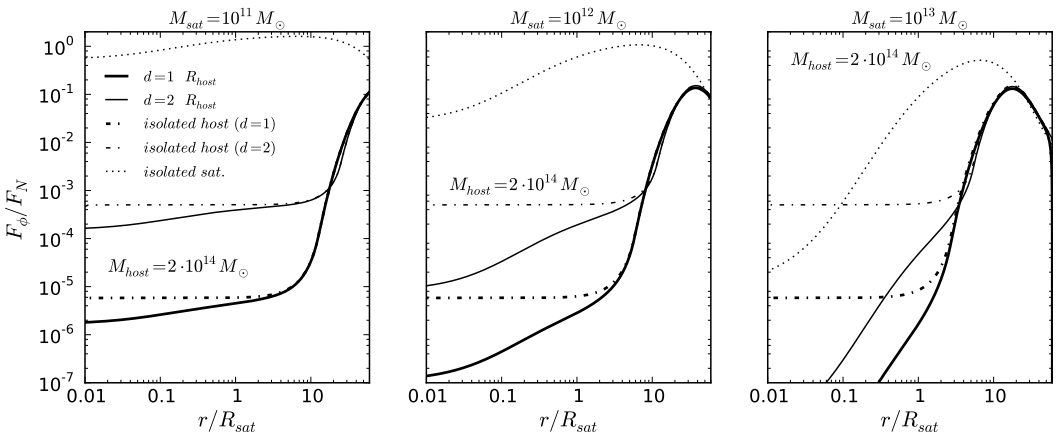


**Figure 2.8:** Force deviation $F_\phi/F_{\rm N}$ for the total density profile of eq. (2.21) (solid lines). This is the deviation that would be experienced by a test mass in the neighborhood of a satellite halo which is itself blanket screened by a nearby host ($M_{\rm host} = 2\times10^{14}M_\odot$). The deviation is shown for two values of the host-satellite separation $d$: thick solid lines for $d = 1R_{\rm host}$ and thin solid lines for $d = 2R_{\rm host}$. Also shown are $F_\phi/F_{\rm N}$ for isolated halos with mass equal to the satellite (dotted) and host (thin and thick dot-dashed). The environmental screening from the host brings the modified forces of the satellite below 10%, therefore nearly unobservable in each case. Figure 2.9 shows larger deviations for lower host masses.

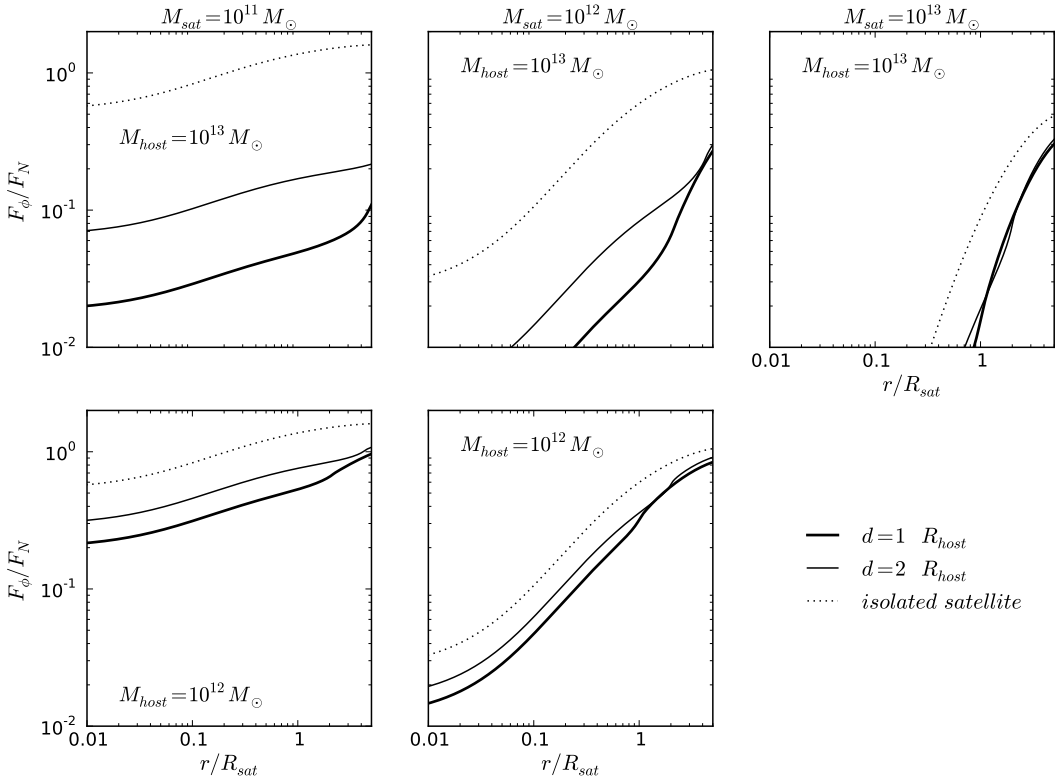


**Figure 2.9:** Force deviation $F_\phi/F_{\rm N}$ for the total density profile of eq. (2.21) (solid lines), using smaller host masses than in figure 2.8. This is the deviation that would be experienced by a test mass in the neighborhood of a satellite halo which is itself (partially) blanket screened by a nearby host. The deviation is shown for two values of the host-satellite separation $d$: thick solid lines for $d = 1R_{\rm host}$ and thin solid lines for $d = 2R_{\rm host}$. For comparison, the dotted line plots the deviation for an isolated satellite: the difference between dotted and solid lines indicate the additional screening due to the nearby host. In each case, the host significantly decreases the force deviations of the satellite, but to a level that is still potentially observable.

satellite profile, but with an amplitude decreased below the observationally interesting level of $\sim 1\%$. In each panel there is a sharp transition of the solid line at the distance $d$ (i.e., location of the cusp in figure 2.7) separating the host and satellite. Here the force ratio for the total density profile is closely approximated by that of the host alone. At very large radii, all three curves fall off rapidly, as the symmetron force decays exponentially due to its finite compton wavelength. The environmental screening from the host brings the force deviation of the satellite below the level of observations for each case. Note that for this and the following two-halo calculations, we set $\phi_0 = M_s^2/M_{\rm Pl}$.

In order to see the partial screening of a satellite, it is necessary to consider smaller hosts. Figure 2.9 shows the force deviation $F_\phi/F_{\rm N}$ for the same range of satellite masses and host satellite separations as in figure 2.8, but with host masses of $10^{13}$ and $10^{12} M_\odot$. For $M_{\rm sat} < M_{\rm host}$, including the host at 2 $R_{\rm host}$ decreases the fifth force by 50-150% relative to gravity, and halving the separation to 1 $R_{\rm host}$ brings a further decrease of 5-10%. For example, an isolated $10^{11} M_\odot$ has $F_\phi \approx 150\% F_{\rm N}$ at its virial radius, while if a $10^{12} M_\odot$ halo is 2 or 1 virial radii away, this deviation is cut down to $60\% F_{\rm N}$ or $45\% F_{\rm N}$, respectively. See appendix B for calculations of the modified forces at the satellite virial radius as a continuous function of $d$.

A few comments on the validity of the approximate host profile of eq. (2.20) and the results of Figs. 2.8, 2.9 are in order here. Since the NFW profile of the host does not change much across the diameter of the smaller satellite, we expect the force deviation predictions to be accurate in the regime $r \lesssim R_{\rm sat}$. Here our spherically symmetric approximation should slightly overestimate the deviation on the side of the satellite nearer the host, while underestimating the deviation on the far side. For $r \gg d$ the offset between host and satellite is negligible, so that eq. (2.20) approaches the NFW density profile eq. (2.11). Thus, our approximation captures well the small and large $r$ behavior of the exact host-satellite system.

In the intermediate regime $r \sim d$ we note that the screening will vary widely between the near and far sides of the satellite. On the side nearer the host we should observe thorough

blanket screening, while on the far side screening from the host may well be negligible, depending on the separation $d$. However, given that dynamical tracers of the satellite mass (such as stars, HI gas, and satellite galaxies) are generally confined to $r \lesssim R_{\rm sat}$, our model describes well the observationally relevant range.

## 2.5 Discussion

We have presented predictions for the modified forces of symmetron gravity around dark matter halos, modeling the halo density with the NFW profile. For a large range of halo masses $10^{10} - 10^{13} M_\odot$ we find order unity deviations from GR at distances $1 - 7\ R_{300}$ from the halo center, while the dwarf-size halos of $10^{10} - 10^{11} M_\odot$ exhibit large deviations throughout (figure 2.2).

We have also shown an average of this deviation given by the quantity $\overline{\gamma}_{\rm vir}$ suggested by (115); our theoretical calculations of $\overline{\gamma}_{\rm vir}$ (figure 2.3) are simply related to observables by Eqs. (2.18) and (2.19). We find $\gtrsim 20\%$ differences over the mass range $10^{10} - 10^{13} M_\odot$, indicating that observations of dynamical and lensing masses of galaxies are a promising way to constrain parameters of the theory.

Furthermore, $\overline{\gamma}_{\rm vir}$ is necessary to test the mass function of the theory. Reference (25) obtains the mass function from symmetron N-body simulations by counting halos as a function of their true or lensing mass. However, observations more commonly yield the dynamical mass of virialized structures; a means of converting between the two is therefore essential to constrain the theory using the mass function.

We have gathered predictions for symmetron, chameleon, and Vainshtein screening in the neighborhood of NFW haloes in order to find ways to distinguish between classes of MG models in realistic astrophysical situations. We find significant differences among the three screening mechanisms, including

- In contrast to the chameleon, the lack of a distinct thin-shell radius for the symmetron results in a nonzero deviation at small radii even for partially screened halos. Since visible tracers of galaxies are often well within the virial radius, the tests of (53, 57) are more easily applied to test symmetron screening.

- At a given radius, the chameleon deviations change rapidly with mass and therefore reach their maximum of 4/3 quickly. The symmetron exhibits more gradual changes in the deviation, while DGP models have no dependence on halo mass.

We note that there is an approximation involved in using the NFW profile: although this profile is a good fit to stacked halo densities in GR simulations, it is possible that the profile itself will change with the modified forces. However, the symmetron N-body simulations of (25) are able to resolve halos of mass $\gtrsim 5 \times 10^{12} M_{\odot}$; for these larger halos we have compared our results for the symmetron field and find them qualitatively consistent with the N-body simulations. (Note that (25) defines a parameter $z_{\rm SSB}$ related to $\mu$ and $M_{\rm s}$ (see (25) for details) and focus on $z_{\rm SSB} = 2.0$. We have checked our results with theirs using this same value for $z_{\rm SSB}$, but our standard choice of parameters corresponds to $z_{\rm SSB} \approx 0.5$, for which the theory predicts relatively lesser deviations from GR. Thus, consistency with the simulations for the larger value of $z_{\rm SSB}$ is actually a *more* stringent test than consistency for our choice of parameters.)

This work has not considered two other screening mechanisms that have recently been discovered: the environmentally dependent dilaton (7, 24) and k-mouflage (1). However, k-mouflage screening has been shown to be similar to Vainshtein (i.e., independent of halo mass), and due to the similar dependence of the derivative of the coupling ($\partial A/\partial\phi \propto \phi$) in symmetron and dilaton models, the dilaton screening may exhibit similarities to the symmetron.

We have also shown results for screening of satellite halos by larger neighboring hosts. We have approximated the host density by averaging its NFW profile in spherical shells

about the satellite: the resulting profile is shown in eq. (2.20) and figure 2.7. We found that the environmental screening effect from a $2\times10^{14}M_{\odot}$ cluster is sufficient to reduce deviations from GR well below the level of 1% for smaller halos located within twice the host virial radius (figure 2.8). However, figure 2.9 shows that for smaller hosts of mass $10^{12}-10^{13}M_{\odot}$ the force deviations around the satellite are decreased (relative to the isolated case) but still potentially observable. One caveat to this method should be mentioned: in reality, adding a second halo breaks the spherical symmetry of our system. Thus we expect that our results for two-body systems slightly underestimate (overestimate) the screening on the side of the halo nearer to (farther from) the second halo.

We comment briefly on the possibility of analytical solutions for two-body systems in symmetron modified gravity. There has been some success in finding approximate analytical solutions of two-body systems in chameleon theories. In (87) the thin shell effect is used to find solutions for uniform density spheres in a variety of configurations. Furthermore, (109) expands these solutions to include an NFW host halo and test body (point mass) satellites of $M_{\rm sat}\leq10^{10}M_{\odot}$. However, these results do not straightforwardly translate to symmetron gravity: the thin-shell effect of the chameleon allows a clean division into 3 regions in the neighborhood of an object with a thin shell (inside the shell, the thin shell itself, and outside the shell); in contrast, the symmetron transitions more smoothly within screened objects (see figure 2.4), making such a partitioning much more difficult.

# Chapter 3

# Voids in Modified Gravity: Excursion Set Predictions

## 3.1 Introduction

Models of modified gravity (MG) are introduced to explain the observed accelerating cosmic expansion, without invoking a cosmological constant in the Einstein equation. Scalar-tensor gravity theories are among those that are well received recently. In these theories, the scalar field is coupled to matter, triggering an extra fifth force which leads to an universal enhancement of gravity. The enhanced gravity violates existing robust tests of general relativity (GR) in the solar system, so that only theories with a *screening mechanism* to suppress the fifth force in high density regions are observationally viable (e.g. 63). Gravity is therefore back to GR in the early universe, as well as in the vicinity of virilized objects where the local density is sufficiently high. MG models like chameleon gravity can therefore pass the tests of current constraints from the solar system (63). Nevertheless, structure formation in these models should be somewhat different from that of the standard $\Lambda$-cold-dark-matter ($\Lambda$CDM, where $\Lambda$ represents the cosmological constant) paradigm. In low density regions of the universe, the fifth force is weakly or not suppressed, so that dark matter and ordinary

matter will feel this extra force and hence evolve differently from the GR case. Qualitatively, one may expect structure to form earlier in MG than in GR with the help of enhanced gravity. Indeed, halos are found to be more massive and more abundant in simulations of $f(R)$ gravity (74) as compared to GR at the same epoch. Similarly, voids appear to be larger and emptier in MG. These qualitative results seem to point in the same direction as some recent observational facts, which have been shown to be in tension with a ΛCDM universe.

Firstly, some galaxy clusters detected using X-ray and lensing techniques at high redshift are found to be too massive and have formed too early (e.g. 30, 45, 50, 60). The probability of the existence of those massive clusters in ΛCDM is prohibitively small, but see Harrison & Coles (38), Hotchkiss (46), Hoyle et al. (51), Waizmann et al. (135, 136). Introducing non-Gaussianity can ease this tension, but the $f_{\rm NL}$ parameter required to fit the data is usually too high, which is in tension with other observational constrains like the cosmic microwave background (CMB). Secondly, the detected integrated Sachs Wolfe (ISW) (111) signal from the stacking of 4-deg$^2$-size regions of the CMB corresponding to the SDSS super clusters and super voids is found to be $2-3\sigma$ higher than estimations from simulations (35, 102). This tension with the ΛCDM paradigm is perhaps more than $3-\sigma$ as suggested in Nadathur et al. (89). Accounting for non-linear ISW effect by using simulations of full-sky ISW maps from (9), the tension remains nearly unchanged (32). Similar conclusions are found by independent study of (39). If one assumes that the expansion history of the universe is given by the concordance ΛCDM model, then one plausible explanation of this discrepancy is that the abundance of structure in the real Universe may be greater than expected, i.e., there might be more clusters and super clusters, and voids might have grown larger and deeper. This explanation seems to coincide with the first tension mentioned above. Again, one could perhaps use this data to constrain non-Gaussianity, and find a large $f_{\rm NL}$, but an alternative solution might be to modify gravity.

In this work, we explore the difference of structure formation in GR and chameleon models of MG. Using the spherical collapse model and excursion set theory (4), we investigate

individual void properties and the void volume distribution function in these two models. We also compare the relative merits of distinguishing between GR and MG using voids or halos; predictions for the latter have been addressed by Li & Efstathiou (72).

One common way to distinguish MG from GR is by looking at the difference between the lensing mass and dynamical mass of halos (15, 31, 67, 115, 144**?** ). The chameleon model studied here predicts that such a difference is at most 1/3 between the screened and unscreened cases. At present, it is still very difficult to have mass estimates of halos which achieve this level of accuracy, partly due to the difficulty of looking for unscreened objects. To realize the 1/3 difference, such objects must be both small, so that they are not self-screened, and located in low density environments, so as not to be screened by the environment. Voids, however, are usually very low in density so that the fifth force is unscreened inside. Furthermore, we show that the strength of the fifth force may be relatively stronger than that of Newtonian gravity in voids. This may lead to a larger difference of void properties from GR than that of halos.

The outline of this paper is as following: In section 3.2, we give a brief summary of the coupled scalar field gravity, of which the chameleon model is an example. In section 3.3, we solve the scalar field profile for voids in this model and highlight interesting differences of the fifth force to Newtonian gravity in voids. In section 3.4, we extend the spherical collapse model to solve for the evolution of shells in voids in this model and identify the best regimes to distinguish this model from GR. Section 4.2 presents the first crossing barrier for voids, and incorporates the moving barrier and environmental dependence of void formation to the excursion set theory to calculate a void volume distribution function. We summarize our results and consider possible ways to test MG in voids in section 3.6.

## 3.2 The Chameleon Theory

This section lays down the theoretical framework for investigating the effects of a coupled scalar field in cosmology. We shall present the relevant general field equations in § 3.2.1,

and then specify the models analyzed in this paper in § 3.2.2.

### 3.2.1 Cosmology with a Coupled Scalar Field

The equations presented in this subsection can be found in Li & Barrow (71), Li & Zhao (75, 76), and are presented here only to make this work self-contained.

We start from a Lagrangian density

$$\mathcal{L} = \frac{1}{2}\left[M_{\rm Pl}^2 R - \nabla^a\phi\nabla_a\phi\right] + V(\phi) - C(\phi)(\mathcal{L}_{\rm DM} + \mathcal{L}_{\rm S}), \tag{3.1}$$

in which $R$ is the Ricci scalar; the reduced Planck mass is $M_{\rm Pl} = 1/\sqrt{8\pi G}$ with $G$ being the gravitational constant; and $\mathcal{L}_{\rm DM}$ and $\mathcal{L}_{\rm S}$ are respectively the Lagrangian densities for dark matter and standard model fields. $\phi$ is the scalar field and $V(\phi)$ its potential; the coupling function $C(\phi)$ characterises the coupling between $\phi$ and matter. Given the functional forms for $V(\phi)$ and $C(\phi)$, a coupled scalar field model is then fully specified.

Varying the total action with respect to the metric $g_{ab}$, we obtain the following expression for the total energy momentum tensor in this model:

$$T_{ab} = \nabla_a\phi\nabla_b\phi - g_{ab}\left[\frac{1}{2}\nabla^c\nabla_c\phi - V(\phi)\right] + C(\phi)(T_{ab}^{\rm DM} + T_{ab}^{\rm S}), \tag{3.2}$$

where $T_{ab}^{\rm DM}$ and $T_{ab}^{\rm S}$ are the energy momentum tensors for (uncoupled) dark matter and standard model fields. The existence of the scalar field and its coupling change the form of the energy momentum tensor, leading to potential changes in the background cosmology and structure formation.

The coupling to a scalar field produces a direct interaction (fifth force) between matter particles due to the exchange of scalar quanta. This is best illustrated by the geodesic equation for dark matter particles

$$\frac{{\rm d}^2\mathbf{r}}{{\rm d}t^2} = -\vec{\nabla}\Phi - \frac{C_\phi(\phi)}{C(\phi)}\vec{\nabla}\phi, \tag{3.3}$$

where $\mathbf{r}$ is the position vector, $t$ the (physical) time, $\Phi$ the Newtonian potential and $\vec{\nabla}$ is the spatial derivative; $C_\phi \equiv \mathrm{d}C/\mathrm{d}\phi$. The second term on the right hand side is the fifth force, with potential $\ln C(\phi)$.

To solve the above two equations we need to know both the time evolution and the spatial distribution of $\phi$, *i.e.* we need the solutions to the scalar field equation of motion (EOM)

$$\nabla^a \nabla_a \phi + \frac{\mathrm{dV}(\phi)}{\mathrm{d}\phi} + \rho \frac{\mathrm{dC}(\phi)}{\mathrm{d}\phi} = 0, \tag{3.4}$$

where $\rho = \rho_{\mathrm{DM}} + \rho_b$, the sum of dark and baryonic matter densities. Equivalently

$$\nabla^a \nabla_a \phi + \frac{\mathrm{dV_{eff}}(\phi)}{\mathrm{d}\phi} = 0, \tag{3.5}$$

where we have defined

$$V_{\mathrm{eff}}(\phi) = V(\phi) + \rho\, C(\phi). \tag{3.6}$$

The background evolution of $\phi$ can be solved easily given the present-day value of $\rho$ since $\rho \propto a^{-3}$. We can then divide $\phi$ into two parts, $\phi = \bar{\phi} + \delta\phi$, where $\bar{\phi}$ is the background value and $\delta\phi$ is its (not necessarily small nor linear) perturbation, and subtract the background part of the scalar field equation of motion from the full equation to obtain the equation of motion for $\delta\phi$. In the quasi-static limit in which we can neglect time derivatives of $\delta\phi$ as compared with its spatial derivatives (which turns out to be a good approximation on galactic and cluster scales), we find

$$\vec{\nabla}^2 \delta\phi = \frac{\mathrm{dC}(\phi)}{\mathrm{d}\phi}\rho - \frac{\mathrm{dC}(\bar{\phi})}{\mathrm{d}\bar{\phi}}\bar{\rho} + \frac{\mathrm{dV}(\phi)}{\mathrm{d}\phi} - \frac{\mathrm{dV}(\bar{\phi})}{\mathrm{d}\bar{\phi}}, \tag{3.7}$$

where $\bar{\rho}$ is the background matter density.

The computation of the scalar field $\phi$ using the above equation then completes the computation of the source term for the Poisson equation

$$\begin{aligned} \vec{\nabla}^2\Phi &= \frac{1}{2M_{\mathrm{Pl}}^2}\left[\rho_{\mathrm{tot}} + 3p_{\mathrm{tot}}\right] \\ &= \frac{1}{2M_{\mathrm{Pl}}^2}\left[\rho\, C(\phi) - 2V(\phi)\right], \end{aligned} \tag{3.8}$$

where we have neglected the kinetic energy of the scalar field because it is always very small for the model studied here.

### 3.2.2 Specification of Model

As mentioned above, to fully fix a model we need to specify the functional forms of $V(\phi)$ and $C(\phi)$. Here we will use the models investigated by (70, 75, 76), with

$$C(\phi) = \exp(\gamma\phi/M_{\rm Pl}), \tag{3.9}$$

and

$$V(\phi) = \frac{\rho_\Lambda}{[1 - \exp{(-\phi/M_{\rm Pl})}]^\alpha}. \tag{3.10}$$

In the above $\rho_\Lambda$ is a parameter of mass dimension four and is of order the present dark energy density ($\phi$ plays the role of dark energy in this model). $\gamma, \alpha$ are dimensionless parameters controlling the strength of the coupling and the steepness of the potential respectively.

We choose $\alpha \ll 1$ and $\gamma > 0$ as in Li & Zhao (75, 76), which ensure that $V_{\rm eff}(\phi)$ has a global minimum close to $\phi = 0$ and that $\mathrm{d}^2V_{\rm eff}(\phi)/\mathrm{d}\phi^2 \equiv m_\phi^2$ at this minimum is very large in high density regions. There are two consequences of these choices of model parameters: (1) $\phi$ is trapped close to zero throughout cosmic history so that $V(\phi) \sim \rho_\Lambda$ behaves as a cosmological constant; (2) the fifth force is strongly suppressed in high density regions where $\phi$ acquires a large mass, $m_\phi^2 \gg H^2$ ($H$ is the Hubble expansion rate), and thus the fifth force cannot propagate far. The suppression of the fifth force is even stronger at early times, and thus its influence on structure formation occurs mainly at late times. The environment-dependent behaviour of the scalar field was first investigated by Khoury & Weltman (63), and is often referred to as the 'chameleon effect'.

## 3.3 Static underdensity solutions

The radial profile of a chameleon-type scalar field has been studied in detail for spherical overdensities, in which cases a simple analytical formula for the fifth force has been derived (63) and shown to agree well with the numerical simulations (74). We know from these previous studies that, depending on its size and environment, a spherical overdensity could develop a thin shell which is a region of fast change of $\phi(r)$ with respect to $r$, and approximately only the matter contained in this shell contributes to the fifth force on a particle at the edge of the overdensity. If the shell is thin the fifth force is much weaker than gravity (the latter coming from all mass contained in the overdensity), while if its thickness becomes comparable to the radius of the overdensity, the fifth force approaches a constant ratio to gravity. For our fiducial model this ratio is $2\gamma^2$ and we choose the coupling $\gamma$ such that $2\gamma^2 = 1/3$, so that the maximum deviations from GR match those of $f(R)$ models.

Unfortunately, no analytical approximation for the fifth force is known for the case of underdensities. It is our task in this section to study $\phi(r)$ in underdensities and the fifth force which results. We will see that the maximum ratio of $2\gamma^2 = 1/3$ will no longer apply in this case: in voids the fifth force can have much stronger effects than gravity.

### 3.3.1 Voids in Newtonian Gravity

Consider a spherically-symmetric underdensity defined by radius $r$ and inner and outer densities, $\rho_{\rm in}$ and $\rho_{\rm out}$, such that $\rho_{\rm in} < \rho_{\rm out}$. First we review the forces around such voids in Newtonian gravity. Since $C(\phi) \approx 1$, the first term on the right-hand side of Eq. (3.8) can be integrated once to give the force per unit test mass

$$F_{\rm N}(\chi) = -\frac{GM(<\chi)}{\chi^2} \tag{3.11}$$

where

$$M(<\chi) = 4\pi \int_0^{\chi} {\rm d}\chi'\, \chi'^2 \rho_0(\chi')\,. \tag{3.12}$$

We are interested in the simplest model of a void, with top-hat density profile

$$\rho_0(\chi) = \begin{cases} \rho_{\rm in} & \text{for} \quad \chi \leq r \\ \rho_{\rm out} & \text{for} \quad \chi > r \end{cases} . \tag{3.13}$$

(We use the notation $r$ for the void radius and $\chi$ for the radial coordinate for the sake of continuity with later sections of the paper.) The resulting force on the mass shell at $r$ is

$$F_{\rm N}(r) = -\frac{4\pi G}{3}\rho_{\rm in} r \tag{3.14}$$

$$= -\frac{\rho_{\rm in} r}{6M_{\rm Pl}^2} . \tag{3.15}$$

Only mass within the radius $r$ contributes to the force on it – test masses inside completely empty voids where $\rho_{\rm in} = 0$ feel no force since the pull from all the mass elements outside the void cancel perfectly. This is a standard, although counter-intuitive, result of Newtonian gravity. If $\rho_{\rm in}$ is nonzero, the force on the shell is equal to that of a point particle of mass $M(< \chi)$ which is located at $\chi = 0$, and the force is attractive.

Similarly, since $V(\phi) \approx \rho_\Lambda$, the second term on the right-hand side of Eq. (3.8) gives the effective force due to the scalar field potential (or equivalently, the cosmological constant),

$$F_\Lambda(r) = \frac{\rho_\Lambda r}{3M_{\rm Pl}^2}. \tag{3.16}$$

This contributes an effective repulsive force at late cosmological times, which we call the dark energy force in this paper.

### 3.3.2 Voids in Chameleon Theories

The total force on a test particle is the sum of the Newtonian force, effective force from the dark energy, and the scalar-mediated fifth force. We will see that the fifth force is always *repulsive* in voids, in the sense that the force on a test mass pushes it away from the center of the void, towards the nearest wall; it aids the dark energy in emptying the void of matter.

The second term on the right-hand side of Eq. (3.3) gives the fifth force, which for our choice of $C(\phi)$ in Eq. (3.9) is

$$F_5(\chi) = -\gamma \frac{\mathrm{d}}{\mathrm{d}\chi}(\phi/M_{\rm Pl})\,. \tag{3.17}$$

We define the ratio of fifth to Newtonian forces as

$$\eta \equiv \frac{F_5}{F_{\rm N}} = \frac{6\gamma M_{\rm Pl}}{r\rho_{\rm in}} \left.\frac{\mathrm{d}\phi}{\mathrm{d}\chi}\right|_{\chi=r}\,, \tag{3.18}$$

which is constrained to be $\eta \leq 2\gamma^2$ for overdensities. Thus the problem of finding the force deviations on a test particle in the void has been reduced to obtaining the scalar field profile $\phi(\chi)$. Before solving Eq. (3.5) to obtain the profile, we note some properties of this scalar field model which will simplify the solution.

At fixed density $\rho_0$, our theory has an effective potential

$$V_{\rm eff}(\phi) = \frac{\Lambda}{[1-\exp\left(-\phi/M_{\rm Pl}\right)]^\alpha} + \rho_0 \exp(\gamma\phi/M_{\rm Pl}). \tag{3.19}$$

Call $\phi_0$ the field value which minimizes this potential for the given density. Using the facts that $\alpha \ll 1$ and $\phi_0/M_{\rm Pl} \ll 1$ (Sec. 3.2.2), we set $\partial V_{\rm eff}/\partial\phi = 0$ and expand in the small parameter $\phi_0/M_{\rm Pl}$ to find

$$\phi_0/M_{\rm Pl} = \frac{\alpha}{\gamma}\frac{\rho_\Lambda}{\rho_0}\,. \tag{3.20}$$

If $m_0$ is the mass of small fluctuations about this minimum, then

$$m_0^2 = \frac{\partial^2 V_{\rm eff}}{\partial\phi^2} = \frac{(\gamma\rho_0)^2}{\alpha M_{\rm Pl}^2 \rho_\Lambda} \tag{3.21}$$

so that the associated Compton wavelength $\lambda_0 \equiv m_0^{-1}$ and the field value at the minimum are related by

$$\phi_0 = \sqrt{\alpha\rho_\Lambda}\lambda_0\,. \tag{3.22}$$

The above analytic relations between the density and associated field value and compton wavelength, namely $1/\rho_0 \propto \phi_0 \propto \lambda_0$, are not a general feature of scalar-tensor theories of

gravity, nor even of chameleon models. For example, in the $f(R)$ model of Hu & Sawicki (52), the relation between these three quantities has no closed form solution. While these analytic relations are useful in themselves, we now show how they can be used to decrease the void parameter space from three to two variables, while simultaneously removing dependence on the theory parameters $\alpha$ and $\gamma$.

Naively, any top-hat void of radius $r$ and density $\rho_{\rm in}$ in a uniform background density $\rho_{\rm out}$ is dependent on three length scales: $r$, $\lambda_{\rm in}$, and $\lambda_{\rm out}$. However we show that since $\phi/M_{\rm Pl} \ll 1$, the Planck scale drops out of the equation of motion, giving us the freedom to rescale the solution by one of these lengths. This reduces the problem to two non-trivial degrees of freedom. The equation of motion Eq. (3.5) is given by

$$\frac{\mathrm{d}^2\phi}{\mathrm{d}\chi^2} + \frac{2}{\chi}\frac{\mathrm{d}\phi}{\mathrm{d}\chi} = -\alpha\frac{\rho_\Lambda\sqrt{\kappa}e^{-\sqrt{\kappa}\phi}}{(1-e^{-\sqrt{\kappa}\phi})^{\alpha+1}} + \rho_0(\chi)\,\gamma\sqrt{\kappa}\,e^{\gamma\sqrt{\kappa}\phi}\,, \tag{3.23}$$

where $\rho_0(\chi)$ is again the top-hat profile of Eq. (3.13). Expanding to lowest order in $\phi/M_{\rm Pl}$ and using $\alpha \ll 1$ we have

$$\begin{aligned}\frac{\mathrm{d}^2\phi}{\mathrm{d}\chi^2} + \frac{2}{\chi}\frac{\mathrm{d}\phi}{\mathrm{d}\chi} &= \alpha\rho_\Lambda\left(\frac{1}{\phi_0(\chi)} - \frac{1}{\phi}\right) &(3.24)\\ &= \frac{\alpha\rho_\Lambda}{\phi_{\rm out}}\left(\frac{\phi_{\rm out}}{\phi_0(\chi)} - \frac{\phi_{\rm out}}{\phi}\right)\,. &(3.25)\end{aligned}$$

Defining the dimensionless field $\psi \equiv \phi/\phi_{\rm out}$ and using (3.22) yields

$$\frac{\mathrm{d}^2\psi}{d\chi^2} + \frac{2}{\chi}\frac{\mathrm{d}\psi}{\mathrm{d}\chi} = \frac{1}{\lambda_{\rm out}^2}\left(\frac{\phi_{\rm out}}{\phi_0(\chi)} - \frac{1}{\psi}\right)\,. \tag{3.26}$$

Then defining a dimensionless radial coordinate $\tau \equiv \chi/\lambda_{\rm out}$, the equation further simplifies to

$$\frac{\mathrm{d}^2\psi}{\mathrm{d}\tau^2} + \frac{2}{\tau}\frac{\mathrm{d}\psi}{\mathrm{d}\tau} = \frac{\phi_{\rm out}}{\phi_0(\tau)} - \frac{1}{\psi}\,. \tag{3.27}$$

Now, from the three length scales we can form two ratios $r/\lambda_{\rm out}$ and $\lambda_{\rm out}/\lambda_{\rm in}$ (note that for voids we must have $0 \leq \lambda_{\rm out}/\lambda_{\rm in} < 1$) and recast the EOM in terms of these. The problem

is then reduced to solution of the differential equation

$$\frac{\mathrm{d}^2\psi}{\mathrm{d}\tau^2} + \frac{2}{\tau}\frac{\mathrm{d}\psi}{\mathrm{d}\tau} + \frac{1}{\psi} = \begin{cases} \lambda_{\rm out}/\lambda_{\rm in} & \text{for} \quad \tau \leq r/\lambda_{\rm out} \\ 1 & \text{for} \quad \tau > r/\lambda_{\rm out} \end{cases} \tag{3.28}$$

with boundary conditions

$$\left.\frac{\mathrm{d}\psi}{\mathrm{d}\tau}\right|_{\tau=0} = 0, \qquad \psi(\tau \to \infty) = 1\,. \tag{3.29}$$

Rewriting Eq. (3.18) in terms of the new variables and using $\rho_\Lambda = \Omega_\Lambda \rho_{\rm c}$, we find

$$\eta(r) = 6\gamma\sqrt{\frac{\alpha\Omega_\Lambda}{\Omega_m}}\frac{M_{\rm Pl}\sqrt{\bar{\rho}_m}}{r\rho_{\rm in}}\left.\frac{\mathrm{d}\psi}{\mathrm{d}\tau}\right|_{\tau=r/\lambda_{\rm out}}, \tag{3.30}$$

where $\bar{\rho}_m$ is the background matter density today.

Before describing the resulting solutions of the scalar field and fifth force for realistic underdensities, we make some comments about the relevance of Eq. (3.28) for our results in Sections 3.4 and 4.2. Since there is no known analytical approximation for $\phi$ in underdensities, as there is in the overdense case, it will be necessary to solve numerically the EOM at each time step for an expanding void in Sec. 3.4. Furthermore, in order to obtain the void-formation barriers of Sec. 4.2, we must calculate the trajectories of many such expanding voids of different initial sizes and densities. While a top-hat underdensity intrinsically has three degrees of freedom, $\rho_{\rm in}$, $\rho_{\rm out}$, and $r$, we have shown that two ratios formed from these quantities are sufficient to solve the EOM. Thus, the most difficult numerical challenge of Sections 3.4 and 4.2 can be overcome with a single two-dimensional table of $\mathrm{d}\psi/\mathrm{d}\tau$ values, where the derivative is evaluated at the border of the void. Furthermore, our recasting of Eq. (3.23) as Eq. (3.28) has no explicite dependence on the theory parameters $\alpha$ and $\gamma$. Thus, this same 2-D table serves to calculate the void-formation barriers under variations in $\alpha$ and $\gamma$, as in Sec. 3.5.6.

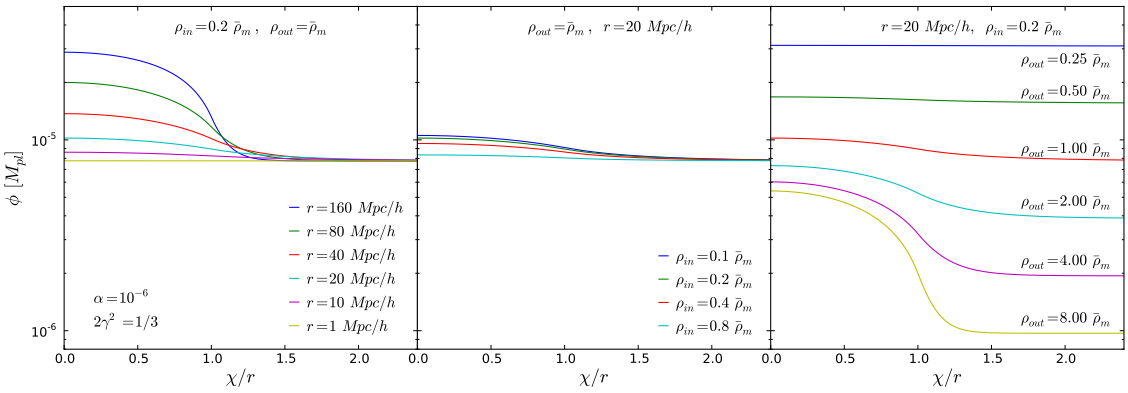


**Figure 3.1:** *Left panel*: Radial profile of the scalar field in a spherical top-hat underdensity for fixed values of $\rho_{\rm in} = 0.2\,\bar{\rho}_m$, $\rho_{\rm out} = \bar{\rho}_m$ and different radii $r$. *Center panel*: The same, but for fixed values of $\rho_{\rm out} = \bar{\rho}_m$, $r = 20\,{\rm Mpc}/h$ and different inner densities $\rho_{\rm in}$. *Right panel*: The same, but for fixed values of $r = 20\,{\rm Mpc}/h$, $\rho_{\rm in} = 0.2\,\bar{\rho}_m$ and different outer densities $\rho_{\rm out}$. Note that the horizontal axis is scaled with respect to void radius $r$, so $\chi/r = 1$ is the edge of the spherical underdensity; also we evaluate the cosmic mean density at the present day, $\bar{\rho}_m(z) = \bar{\rho}_m(0)$.

### 3.3.3 Radial Profile of the Scalar Field

Now we consider the results for the radial profile of the scalar field in various underdensities, paying special attention to the value of the derivative at the void border. The left panel of Fig. 3.1 shows the dependence on void radius, $r$. If $r$ is small, then the underdensity can be considered as a small perturbation on the environment and the scalar field value inside is very close to its value at the boundary. As $r$ increases, however, there is increasing space for $\phi$ to evolve away from the exterior value (here $\phi_{\rm out} \approx 0.8 \times 10^{-5} M_{\rm Pl}$) as $\chi/r$ decreases, and therefore the scalar comes closer to reaching the value which minimizes the interior effective potential. Since $\phi_{\rm in(out)} \propto 1/\rho_{\rm in(out)}$ and $\rho_{\rm out}/\rho_{\rm in} = 5$ in the figure, we know $\phi_{\rm in} = 5\phi_{\rm out}$ and see that even $160\,{\rm Mpc}/h$ is not enough space for the scalar field to attain its minimum at the center of the void.

Fig. 3.1 shows the dependence of the scalar field profile $\phi(r)$ on interior density $\rho_{\rm in}$ in the central panel, assuming an exterior density equal to the cosmic mean. Here the field does not experience much change between the outside and inside of the void, growing by only 25% in the most extreme case, $\rho_{\rm in} = 0.1\,\bar{\rho}_m$. As a result, the derivative of the scalar, and therefore the fifth force, at the void border $\chi/r = 1$ must be small. However, we will see that in order to get a full picture of the forces involved it is necessary to consider the gravitational force and dark energy force as well. For this void the magnitude of the fifth force is about twice as large as Newtonian gravity, so that even this slowly varying $\phi$ profile results in a force that is stronger than $F_{\rm N}$.

Finally, the dependence on $\rho_{\rm out}$ is shown in the right panel of Fig. 3.1. The variations here appear more drastic, since only in this panel is the limiting value $\phi_{\rm out}$ changed from one curve to another. With fixed interior density, a denser environment for the void results in a larger change in the scalar and correspondingly higher derivative ${\rm d}\phi/{\rm d}\chi$. Note also that due to Birkhoff's theorem, changes in $\rho_{\rm out}$ do not affect the gravitational force inside the void, nor is the dark energy force is affected. So only from this panel can we infer directly that larger gradients of $\phi$ imply greater deviations from GR.

There are some interesting differences from the overdense case. Consider an overdensity and underdensity each embedded in the same environmental density $\rho'_{\rm out}$, with corresponding minimum $\phi'_{\rm out}$. For the overdensity, we know $\phi$ decreases from $\phi'_{\rm out}$ as we move towards the center; however by the shape of the effective potential Eq. (3.19), $\phi$ is strictly positive, so $0 < \phi'_{\rm in} < \phi'_{\rm out}$. The maximum change is therefore $\Delta\phi = \phi'_{\rm out}$, no matter how great is the interior density. In contrast, for the underdensity, $\phi$ increases from $\phi'_{\rm out}$ as we move towards the center so that $\Delta\phi$ has no such bound: $\rho_{in}$ can be infinitely small in principle. For concreteness consider the lowest curve on the right panel of Fig. 3.1: here $\phi'_{\rm out} = 10^{-6} M_{\rm Pl}$ so that for an overdensity $\Delta\phi < 10^{-6} M_{\rm Pl}$, while for the pictured underdensity we see $\Delta\phi \geq 4 \times 10^{-6} M_{\rm Pl}$. Since the fifth force is proportional to the derivative of $\phi$ at the void border, we expect this lack of upper bound on $\Delta\phi$ for underdensities to show itself in the force. We turn our attention next to these results.

### 3.3.4 The Fifth Force

In the top panels of Fig. 3.2 we show the force deviation $\eta = F_5/F_{\rm N}$ with variations in the three physical parameters which define a void, $r$, $\rho_{\rm in}$, and $\rho_{\rm out}$. The first interesting feature is that $\eta$ is always negative. The fifth force in voids is repulsive, always pointing at the opposite direction of normal gravity. This is the direct consequence of the scalar field profile we have shown in Fig. 3.1, whose slope is always negative at the edge of the underdensity. Intuitively, this repulsion occurs due to the Yukawa potential ($e^{-\chi/\lambda}/\chi$) of the scalar: at distances of the order of the Compton wavelength, the potential falls off more strongly than $1/\chi$. Mass elements on the far wall of a large void are unable to cancel the pull of the near wall. Furthermore, even if $\rho_{\rm in}$ is nonzero, the integrated mass inside the shell is unable to compete with the denser nearby wall, and the force is again repulsive.

Secondly, as we anticipated in Sec. 3.3.3, the unboundedness of the field, along with the result of Eq. (3.15) that $F_{\rm N}$ vanishes as $\rho_{\rm in} \to 0$ or $r \to 0$, leads to deviations which do not share the bound of $|\eta| \leq 2\gamma^2$. Thus the relative strength of the fifth force can be much larger

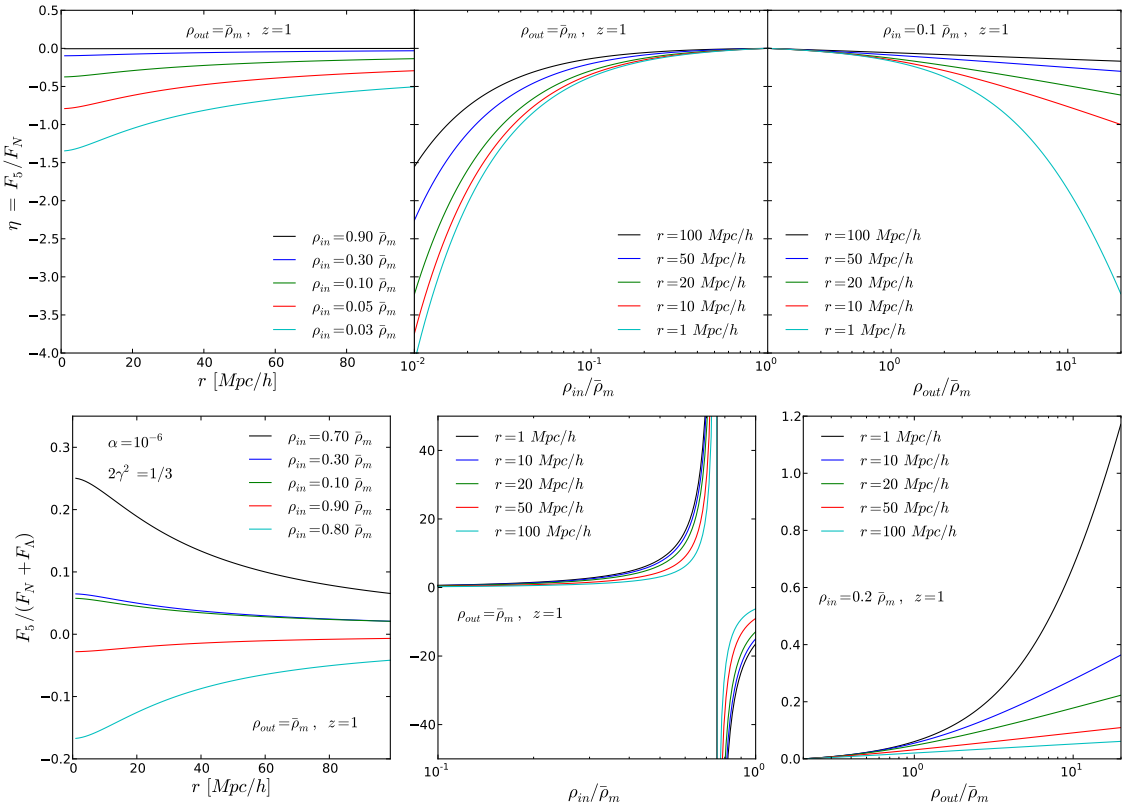


**Figure 3.2:** *Top-left panel:* Variations of the force deviation $\eta$ with underdensity radius, $r$. The exterior density is fixed to the cosmic mean today, $\rho_{\rm out} = \bar{\rho}_m$. Various values of interior density $\rho_{\rm in}$ are shown, with $\rho_{\rm in}$ decreasing from top to bottom. *Top-center panel:* The same, but for continuous variations of $\rho_{\rm in}$, fixed $\rho_{\rm out} = \bar{\rho}_m$ and various values of radius $r$, with $r$ decreasing from top to bottom. *Top-right panel:* The same, but for continuous variations of $\rho_{\rm out}$, fixed $\rho_{\rm in} = 0.1\,\bar{\rho}_m$, and various values of radius $r$, with $r$ decreasing from top to bottom. Note that in all the panels, we evaluate the cosmic mean density at redshift one, $\bar{\rho}_m(z) = \bar{\rho}_m(1)$. *Bottom-left, -middle* and *-right panels* are the same as the top-left, -middle and -right panels, but showing the fractional difference of the total force between MG and GR theories, $F_5/(F_N+F_\Lambda)$.

than Newtonian gravity, as seen in all top panels of Fig. 3.2. Even for common voids with ratio of densities $\rho_{\rm in}/\rho_{\rm out} = 0.2$ we can have $|\eta| \approx 1/3$, already reaching the upper bound for overdensities. If the ratio decreases to the percent level, then $\eta \sim -2$ for the smallest voids.

The left panel of Figs. 3.1 and top-left panel of Fig. 3.2 both show variations with respect to void radius $r$. Comparing these, we see that while the change in $\phi$ and therefore the fifth force increases with void radius, the deviation $\eta$ gets smaller. Thus we infer that $F_{\rm N}$ increases more quickly than $F_5$ in these cases due to the increasing mass enclosed within the larger void radius.

In contrast, comparing the middle panel of Figs. 3.1 and top-middle panel of 3.2 shows that under variations in $\rho_{\rm in}$ the changes in the fifth force dominate the dependence of $\eta$. The net effect of decreasing the interior density is to strengthen the fifth force relative to gravity.

The variations of $\rho_{\rm out}$ in the top-right panel of Fig. 3.2 leave $F_{\rm N}$ unaffected, so here changes in $\eta$ straightforwardly reflect changes in $F_5$. We can unify the results of varying $\rho_{\rm out}$ and $\rho_{\rm in}$ by noting that increasing the density contrast $\rho_{\rm out}/\rho_{\rm in}$ generally increases the deviation from GR.

In principle this unboundedness of the force ratio $\eta$ in underdensities looks very promising for distinguishing between GR and chameleon models. However, at late times when $\bar{\rho}_m$ and $\rho_\Lambda$ are comparable, the repulsive dark energy force can dominate over Newtonian gravity where the density is low. $F_\Lambda$ is common in both GR and MG models but negligible for halos where the local density is much greater than the cosmic mean. The evolution of voids in MG models are therefore affected by $F_5$, $F_\Lambda$ and $F_N$.

Bottom panels of Fig. 3.2 show the fractional difference of total force between MG and GR, $F_5/(F_N{+}F_\Lambda)$. Comparing them with the top panels, we find the following: A.) like $\eta$, the fractional difference decreases with radius (bottom-left) and increases with $\rho_{\rm out}$(bottom-right). This is because the additional $\rm F_\Lambda$ term is just a constant at a certain epoch. B.)

$F_5/(F_N+F_\Lambda)$ can be positive or negative, depending on the relative amplitude of $F_N$ and $F_\Lambda$. The transition occurs at $\rho_{\rm in} = 2\rho_\Lambda$ when $F_N$ is canceled out by $F_\Lambda$, and the evolution of the system is only governed by $F_5$. Note that the sign switch in $F_5/(F_N+F_\Lambda)$ is no more than an indicator for the switch of the relative strength between $F_N$ and $F_\Lambda$. The forces $F_\Lambda$ and $F_5$ are always repulsive, and act to accelerate the expansion of void. C.) When $\rho_{\rm in}$ is close to $2\rho_\Lambda$, the fractional difference can be very large.

In summary, if we track the evolution of a spherical underdensity with the radius of $r$, in the early universe it is dominated by $F_N$, the amplitude of which decreases with $\rho_{in}$. Later, the repulsive dark energy force $F_\Lambda$ from the background scalar field emerges to cancel part of $F_N$, and it helps to accelerate the expansion of void shells. In the mean time, $F_5$ appears from the coupling of the scalar field with mass, and is also repulsive in voids. As the void keeps emptying itself, $F_5$ becomes larger and $F_\Lambda$ also grows with time as $\Omega_\Lambda$ increases. The amplitude of the positive $F_N+F_\Lambda$ keeps decreasing until $\rho_{\rm in} = 2\rho_\Lambda$, then $F_N + F_\Lambda$ switches sign and the amplitude starts increasing. $F_5$ should also keep increasing with time as $\rho_{\rm in}$ decreases faster than its environment density, which makes the density contrast inside and and outside the void grow larger. Overall, $F_5$ should help to accelerate the expansion of void. In the next section, we will quantify this effect.

## 3.4 Evolving individual void

With the solution of the fifth force in underdense regions, we can apply it to solve the equations that govern the evolution of a spherical underdensity in a given environment specified by its density. We will explore how the evolution of voids or underdense regions are affected by the fifth force.

### 3.4.1 Evolution of Environment

We have shown in the previous section that the profile of the scalar field and hence the fifth force depends on the local density as well as the density of its environment. This is one distinct feature of chameleon models. We therefore need to follow the evolution of the environment properly in order to calculate the fifth force. The environmental dependence in chameleon models has been discussed by Li & Efstathiou (72) and Li & Lam (73) for halos. We shall adopt the same idea of taking the environment as a spherical region with radius much larger than the underdensity in consideration. The exact choice of the environment size will be specified where it is used later for the void statistics (Sec. 3.5.3). Note that for the purposes of single-shell evolution which we describe in this section, the environment is completely specified by its density relative to the cosmic mean.

To track the non-linear evolution of the environment, we denote its physical radius at time $t$ by $r(t)$, its initial comoving radius by $R$, and define $q(t) \equiv a(t)R$. The evolution equation for $r(t)$ is

$$\frac{\ddot{r}}{r} = -\frac{1}{6M_{\rm Pl}^2}\left(\rho - 2\rho_\Lambda\right), \tag{3.31}$$

where $\rho \equiv 3M/4\pi r^3$ is the matter density in the spherical region of the environment and the constant $\rho_\Lambda \approx V(\phi)$ is the effective dark energy density. Note that Eq. (3.31) assumes that the environment is unaffected by the fifth force. We make this approximation since the environments are very large in size and therefore the effects of the fifth force on them are minimal. Let us define $y(t) \equiv r(t)/q(t)$ and change the time variable to $N \equiv \ln(a)$; derivatives with respect to $N$ are denoted by $y' = {\rm d}y/{\rm d}N$. By using Eq. (3.31), $q(t) \propto a(t)$ and the Friedman equation $H^2/H_0^2 = \Omega_m a^{-3} + \Omega_\Lambda$, we find

$$y'' + \left[2 - \frac{3}{2}\Omega_m(N)\right] y' + \frac{\Omega_m(N)}{2}\left(y^{-3} - 1\right) y = 0, \tag{3.32}$$

which is a non-linear equation, where $\Omega_m(N) \equiv \Omega_m e^{-3N}/(\Omega_m e^{-3N} + \Omega_\Lambda)$, and $\Omega_\Lambda(N) \equiv \Omega_\Lambda/(\Omega_m e^{-3N} + \Omega_\Lambda)$.

At very early times we must have $y \approx 1$ and so can write $y = 1 + \epsilon$ with $|\epsilon| \ll 1$. Substituting this into Eq. (3.32) to get the linearised evolution equation for $\epsilon$, we find that $\epsilon \propto D_+$, in which $D_+$ is the linear growth factor governed by the equation

$$D_+'' + \left[2 - \frac{3}{2}\Omega_m(N)\right] D_+' - \frac{3}{2}\Omega_m(N) D_+ \quad = \quad 0, \tag{3.33}$$

and the proportionality coefficient can be found using mass conservation: $y^3(1 + \delta_i) = 1 \Rightarrow \epsilon = -\delta_i/3 \propto D_+$ (here $\delta_i$ is the linear density perturbation at the initial time). As a result, the initial conditions for $y$ are $y(a_i) = 1 - \delta_i/3$ and $y'(a_i) = -\delta_i/3$.

Eqs. (3.32, 3.33), associated with their corresponding initial conditions, completely determine the necessary dynamics in the ΛCDM model used for the environment shell. In what follows we shall use $y_{\rm env}$ to denote the $y$ for the environment, in contrast to that for the underdensity, which we shall denote by $y_{\rm v}$. We will reserve $r$ for the physical radius of the underdensity, matching the notation of Sec. 3.3.

### 3.4.2 Evolution of Underdensity

The only difference between the evolution of an underdensity and that of its environment is the effect of the fifth force. To calculate the fifth force at each time-step we use a spherical top-hat profile,

$$\rho(\chi) = \begin{cases} \rho_{\rm v} & \text{for} \quad \chi \leq r \\ \rho_{\rm env} & \text{for} \quad \chi > r \end{cases} . \tag{3.34}$$

We assume there is no shell crossing, so that to study the evolution we only need to understand the motion of the shell at the edge. Note that this is not strictly true: for a model different than ours, Martino & Sheth (80) have shown that modified gravity can cause an initially top-hat underdensity to have a slight density gradient near the edge. We find a similar effect, but it is quite small and it is beyond the scope of this paper to self-consistently track the deviations of the density profile from the top-hat.

Denoting the density inside the underdensity by $\rho_{\rm v}$ and using mass conservation, we can show that

$$\begin{aligned} \rho_{\rm v} r^3 &= \left(\bar{\rho}_m a^{-3}\right)(aR)^3 \\ \rho_{\rm v} &= \bar{\rho}_m \left(a y_{\rm v}\right)^{-3} , \end{aligned} \tag{3.35}$$

where $\bar{\rho}_m$ is the background matter density today. Similarly, the matter density in the environment, $\rho_{\rm env}$, can be expressed in terms of $y_{\rm env}$ as

$$\rho_{\rm env} = \bar{\rho}_m \left(a y_{\rm env}\right)^{-3} . \tag{3.36}$$

Using these relations we can rewrite Eqs. (3.15) and (3.17) in terms of the variables $y_{\rm v}$ and $y_{\rm env}$, yielding

$$\begin{aligned} F_{\rm N} &= \frac{1}{6M_{\rm Pl}^2}\bar{\rho}_m \left(a y_{\rm v}\right)^{-2} R \\ &= \frac{1}{2}\Omega_m \left(H_0 R\right)\left(a y_{\rm v}\right)^{-2} H_0, \end{aligned} \tag{3.37}$$

$$\begin{aligned} F_5 &= \gamma \frac{{\rm d}\left(\phi/M_{\rm Pl}\right)}{{\rm d}\chi}\Big|_{\chi=r} \\ &= \sqrt{3\alpha\Omega_\Lambda}\gamma H_0 \frac{{\rm d}\psi}{{\rm d}\tau}\Big|_{\tau=r/\lambda_{\rm out}} , \end{aligned} \tag{3.38}$$

where

$$r/\lambda_{\rm out} = \sqrt{\frac{3}{\alpha\Omega_\Lambda}} a y_{\rm v} \left(a y_{\rm env}\right)^{-3} \gamma \Omega_m H_0 R , \tag{3.39}$$

and $\psi$ and $\tau$ are defined as in Sec. 3.3. The fifth-force-to-gravity ratio is then

$$\eta = \frac{\sqrt{3\alpha\Omega_\Lambda}\gamma \frac{{\rm d}\psi}{{\rm d}\tau}\Big|_{\tau=r/\lambda_{\rm out}}}{\frac{1}{2}\Omega_m \left(H_0 R\right)\left(a y_{\rm v}\right)^{-2}} , \tag{3.40}$$

and the evolution equation of the underdensity becomes

$$\frac{\ddot{r}}{r} = -\frac{1}{6M_{\rm Pl}^2}\left[\rho_{\rm v}(1+\eta) - 2\rho_\Lambda\right] . \tag{3.41}$$

Rewriting using $y_{\rm v}$ we obtain

$$y_{\rm v}'' + \left[2 - \frac{3}{2}\Omega_m(N)\right] y_{\rm v}' + \frac{\Omega_m(N)}{2}\left[y_{\rm v}^{-3}(1+\eta) - 1\right] y_{\rm v} = 0\,. \tag{3.42}$$

Note that we absorb all the difference between GR and MG in $\eta$ in the above equation, which is the same quantity we have shown in the top panels of Fig. 3.2. Equations (3.32, 3.33, 3.40, 3.42) form a set of coupled nonlinear differential equations, which govern the evolution of an underdensity in a given environment.

We can now solve the above equations to track the evolution of a spherical top-hat void. We compare results in our chameleon model and in ΛCDM in Fig. 3.3; both start from the same underdense regions $\delta_{\rm sc} = -2.76$, where $\delta_{\rm sc}$ (shell-crossing) is the initial density contrast of the void region extrapolated to today. This setting of the initial condition corresponds to voids that would have just shell-crossed today in the ΛCDM universe (121). The mean nonlinear density contrast of those underdense regions today is $\delta = -0.8$, so that even without the fifth force these are already fairly empty voids.

The difference between the two models in the void expansion history depends on the initial comoving sizes of voids $R$ as well as their environment, quantified by $\delta_{\rm env}$, the initial environment density perturbation linearly extrapolated to today. Voids in denser environments show a larger difference between GR and MG. This is due to the greater density contrast realized by an underdensity in a very overdense environment. As seen in Figs. 3.1 and 3.2, such contrasts in density cause a large change in the scalar field, which in turn results in a stronger fifth force.

In all cases, voids in MG expand faster and grow larger than their counterparts in ΛCDM. The comoving void radius would have grown by a factor of 1.7 at shell-crossing in GR. However in MG, Fig. 3.3 shows the same underdensity would have grown by a factor of $\sim 2$ for voids with $R \sim 3$ Mpc$/h$ in dense environments. The difference between GR and MG is at $\sim 10\%$ level, and smaller for less dense environments. For larger voids the difference becomes smaller, e.g., for $R \sim$100 Mpc$/h$ it is at the sub-percent level. Although the absolute

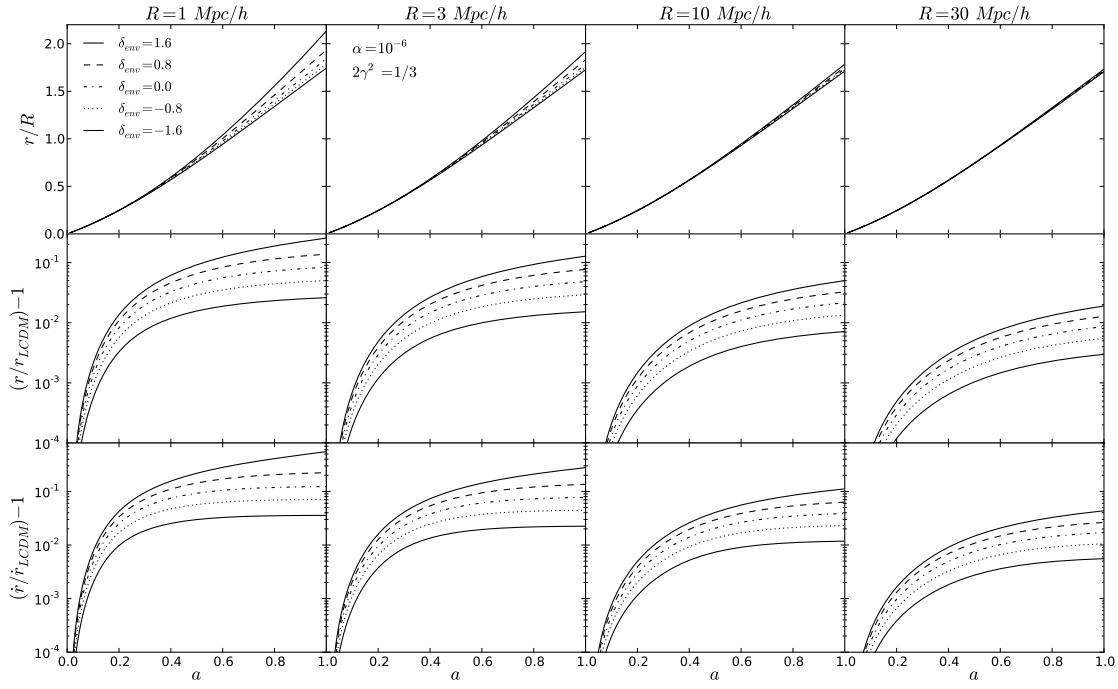


**Figure 3.3:** *Top row:* Radius $r$ of an expanding underdensity in units of its initial comoving radius $R$, as a function of scale factor $a$. *Center row:* Fractional difference between the radii of such underdensities with identical initial conditions, expanding with and without the fifth force. *Bottom row:* Fractional difference in the velocity. Columns show various values of initial comoving radius, $R = 1, 3, 10$ and $30\,\mathrm{Mpc}/h$, from left to right. All panels have an initial underdensity, linearly extrapolated to today, of $\delta = -2.76$: these are objects which in a universe with no fifth force would have just reached the epoch of shell-crossing today. Various values of the exterior density are shown, with $\delta_{\mathrm{env}}$ decreasing from top to bottom. The largest deviations from GR occur for voids expanding within a larger overdense region.

value of the fifth force is smaller for small voids (left panel of Fig. 3.1), the gravitational force is correspondingly smaller due to the decreased integrated mass. As shown in Fig. 3.2, the net effect is that the instantaneous ratio between the two is larger (more negative) for smaller voids. The void size $y_v$ or $r$ at any given time shows the integrated effects of nonzero $\eta$ from all previous times. Thus the radii of smaller voids have expanded more beyond their $\Lambda$CDM counterparts, which themselves have expanded much more than the background.

While the size of voids shows the cumulative effect of gravity, the expansion velocity of each shell responds more sensitively to any change of gravity at a given time. The bottom panels of Fig. 3.3 shows the fractional difference of the expansion velocity of shells in GR and MG. Indeed, the differences in velocity are larger than the differences in sizes. For voids of $R \sim 3$ Mpc$/h$, the expansion velocity can be 10% to 30% faster in MG in over-dense environments. By $R \sim 30$ Mpc$/h$, the difference has dropped to a few percent in this model.

Our results suggest that perhaps the best way to look for modified gravity is to find voids in overdense environments, especially small voids, where we expect the difference from GR is maximized. Those voids should be emptier due to the relatively strong repulsive fifth force and faster expansion of the shells. Moreover, the difference in redshift space could be more prominent due to the even larger difference in the velocity field. We propose that the clustering analysis of tracers of small voids in redshift space could be a powerful test of GR. Predictions for this test from $N$-body simulations will be presented in a separate paper.

## 3.5 Void definition and statistics

Having success in following the evolution of a single shell, we can now look for a common definition of voids for GR and MG. Then we will compare the population of voids in both GR and MG statistically by generalizing the excursion set approach (4). But first we will lay down briefly the essential idea of the excursion set theory; more details can be found in Appendix C.

### 3.5.1 Excursion Set Theory

Assume that the initial local density perturbation filtered at a given scale $R$, $\delta(x, R)$ follows a Gaussian distribution, and that there is no correlation of $\delta(x, R)$ between different filter sizes (for correlated $\delta$, see Musso & Sheth (88)). Then we know A.) the distribution can be fully described by its variance $S$, and B.) when varying the filter size $R$ to $R - \mathrm{d}R$ or equivalently in hierarchical models, $S \to S + \mathrm{d}S$, the increment of $\delta(x, R)$ is independent from its previous value and should also follow a Gaussian distribution with the variance of $\mathrm{d}S$. Thus, $\delta(x, S)$ is just a Brownian motion with 'time' variable $S$. In the spherical collapse model, if a local density exceeds a certain barrier $\delta_c$, then it will collapse and form a virialized halo with all the mass $M'$ enclosed within $R'$ by some given time. In the $(S, \delta)$-plane, if we start the walk from the origin, walks that cross $\delta_c$ for the first time at $S' = \sigma^2(M')$ correspond to such objects. Walks which cross first at smaller values of $S$ form higher mass halos. Therefore, the fraction of mass that has collapsed and formed halos heavier than $M'$ is the fraction of random walks $\delta(x, S)$ that have crossed the barrier $\delta_c$ at $S < S'$. Alternatively, one can calculate the fraction of mass that is incorporated in halos at a given range of halo mass $[M,\ M + \mathrm{d}M]$, or equivalently, $[S, S + \mathrm{d}S]$ at a given redshift $z$:

$$f(S, z)\mathrm{d}S = \frac{1}{\sqrt{2\pi S}} \frac{D_+(0)\delta_c}{D_+(z)S} \exp\left[-\frac{D_+^2(0)\delta_c^2}{2D_+^2(z)S}\right] \mathrm{d}S, \tag{3.43}$$

where $f(S, z)$ the first-crossing distribution of the Brownian motion to the barrier $D_+(0)\delta_c/D_+(z)$, and $D_+$ is the linear growth factor. The first crossing distribution essentially gives the halo mass function (see Appendix C). There is equal chance for a random walk to go negative in $\delta$. Thus, once an appropriate first-crossing barrier for voids, $\delta_{\mathrm{v}}$, is given, one can also find the void size distribution function by the same method.

### 3.5.2 First crossing barrier for void

For halos, the first crossing barrier $\delta_c$ is usually defined as the linearly extrapolated initial overdensity at the time of collapse, i.e., when the mass shells reach zero radius. This time can be calculated using the spherical collapse model. Naively one can find the shell-crossing barrier for voids in a similar way. The shell at the radius of $r$ of a perturbed spherical underdense region will expand faster than the shell at $r' = r + \Delta r$, as the enclosed mass within the border shell is smaller. Shell-crossing for underdense regions occurs when the two shells collide. This occurs at the present day for underdense regions with $\delta_{\rm sc} = -2.76$ (the density contrast at the initial condition extrapolated to today) for the concordance ΛCDM model. Like $\delta_c$, $\delta_{\rm sc}$ depends on $\Omega_{\rm m}$ and is independent of smoothing scale. Moreover, the underdense region at shell-crossing happens to be very empty, i.e., its nonlinear underdensity is $\delta = -0.8$. Therefore, $\delta = -0.8$ serves nicely as an empirical definition of voids.

In modified gravity, however, the situation is more complicated. First, the shell-crossing barrier can depend on the environment, simply because the fifth force and hence the expansion history of shells depends on the environment. Therefore, one may expect voids (likewise halos (72)) to form differently depending on the environment. Second, even for the same environment, the population of voids may also be different from ΛCDM, due to the size dependence of the force which leads to scale dependence of the barrier.

In chameleon models, the fifth force does speed up the expansion of voids (as seen in Fig. 3.3), but the shell-crossing time usually occurs later than in ΛCDM with the same initial conditions. This is because the effect of the fifth force on the relative accelerations of neighboring shells is in the opposite direction from gravity. For $-1 < \eta < 0$ the fifth force opposes but does not overcome gravity, so that the pull of inner shells on outer ones is reduced, making the critical density for shell crossing in chameleon models harder to reach. If an observer is riding on the boundary shell, then all the nearby shells move closer with time, but more slowly than shells feeling only standard gravity. Furthermore, for some initial density perturbations, the shell crossing does not happen at all.

Since the epoch of shell crossing can be unreasonably late or undefined for these models, it is easier to use empirical criteria for void formation. We choose $\delta = -0.8$ as a common criteria for the following reasons, A.) it correspond to the first-crossing barrier in ΛCDM, making it easy to compare with results from ΛCDM; B.) Voids with $\delta = -0.8$ are indeed very empty, and can be defined by the same way in simulations and observations, thus enabling one to make direct comparisons. For example, in Hoyle & Vogeley (48) and Sutter et al. (125) they use similar threshold to define voids in the 2dFGRS and SDSS galaxy samples. Pan et al. (101) also find voids from SDSS7 having similar density contrast, $\delta < -0.85$ at the edges.

Thus, we use the requirement that the nonlinear density constrast today is $\delta = -0.8$, along with Eqs. (3.32, 3.33, 3.40, 3.42), to solve for the initial underdensity as a function of scale $S$ and environment $\delta_{\rm env}$. The resulting void-formation barrier is shown in Fig. 3.4. Unlike ΛCDM where the crossing barrier is flat, barriers in chameleon models are scale dependent. In general, barriers in chameleon models are lower (less negative). Smaller voids have shallower barriers to reach in order to form due to the fact that the fifth force in smaller voids is relatively stronger (see Fig. 3.3), which makes them to expand faster. In other words, for reaching the same $\delta = -0.8$ today, the necessary initial density contrast for smaller voids is smaller (less negative). The crossing barriers keep decreasing (becoming less negative) and steepening with the increase of $S$. This is very different from the collapsing barrier for halos in the same model, where they are leveling off at $S \sim 5$ (72). This difference is a direct result of the fifth force strength upper bound of $2\gamma^2$, which only applies to overdensities.

Fixing void size, the barrier is lower (less negative) and steeper for denser environment, where the difference from the flat barrier in ΛCDM is also larger. Therefore the difference of void population with ΛCDM should be more prominent in such regions. This environmental dependence of crossing barrier is the opposite for halos, where the collapsing barriers are higher (more positive), and closer to the ΛCDM barrier for denser environment (72). Qualitatively, these two opposite pictures in voids and halos can be understood by the same

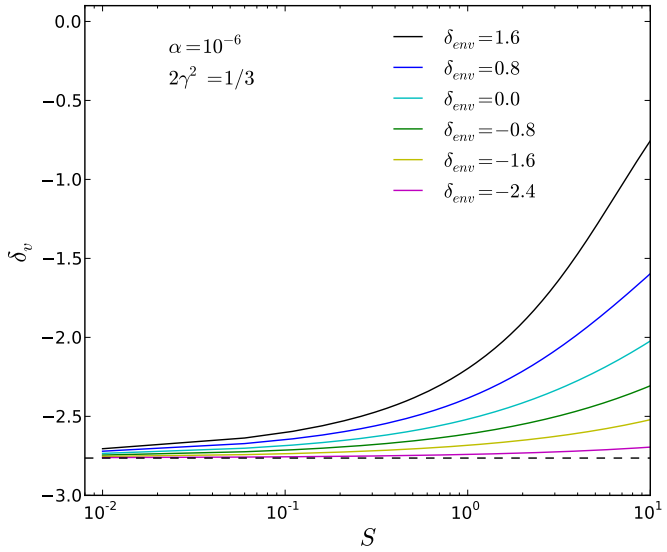


**Figure 3.4:** The linearly-extrapolated void formation barriers for various environments as a function of scale, $S = \sigma^2(M)$. Environment densities decrease from $\delta_{\rm env} = 1.6$ to $\delta_{\rm env} = -2.4$ from top to bottom. The dashed line shows the constant ΛCDM barrier, $\delta_{\rm v} = -2.76$ which results from the same void-formation criteria of nonlinear density $\delta = -0.8$.

reasoning, i.e., for voids or halos of the same mass given $\rho_{\rm in}$ (the mean density in the void or halo region), the strength of the fifth force is larger for larger differences between $\rho_{\rm in}$ and the background density outside the perturbed region, $\rho_{\rm out}$. For voids $\rho_{\rm in} < \rho_{\rm out}$, a larger $\rho_{\rm out}$ means $|\rho_{\rm out} - \rho_{\rm in}|$ is larger and hence a larger fifth force, while for halos $\rho_{\rm in} > \rho_{\rm out}$, a larger $\rho_{\rm out}$ means $|\rho_{\rm out} - \rho_{\rm in}|$ is smaller therefore a smaller fifth force.

### 3.5.3 Moving environment approximation

In calculating the void barriers in the previous section, the environment was specified only by its linear density perturbation, $\delta_{\rm env}$. In order to derive the first-crossing distributions and other void statistics it is necessary also to specify an environment length scale.

In treating spherical collapse in chameleon models, Li & Efstathiou (72) used an environment scale of 8 Mpc/$h$ for halos of every size. Such a fixed-environment scale works well for halos, since the range of interesting virial radii is fairly small, $\sim 0.1-1$ Mpc/$h$. Furthermore, since throughout collapse the proto-halo is always shrinking, there is little worry of its size becoming comparable to the environment scale. On the other hand, the interesting void sizes we are considering range from $\sim 1-30$ Mpc/$h$, and each will expand beyond its initial comoving radius by a factor 1.7 at formation. Thus we need to consider the definition of the environment more carefully.

First, the scale of the environment should at least be larger than the final size of the void. Secondly, it should also be large enough so that the scalar field in the environment has space to settle to its minimum. This is to guarantee that the boundary condition Eq. (3.29) for the scalar field profile equation holds. Third, it cannot be too large because this would simply mean using a value very close to the cosmological density $\bar{\rho}_m$ for all void environments. Bearing these considerations in mind, we introduce a moving environment approximation, in which the initial environment scale is a function of the initial void scale, specifically $R_{\rm env} = 5\,R$.

We notice that in the moving environment approximation, the expanding void shell and collapsing environment shell may cross for voids in very overdense environments. Therefore we also calculate the first-crossing distributions with a large fixed-environment scale of $R_{\rm env} = 75\,{\rm Mpc}/h$, so that the environment shell begins its collapse much farther from the void shell. The difference between the two approximations is less than 10% for the void scales of observational interest, i.e., those $\sim 1\,{\rm Mpc}/h$ and larger; details of the comparison can be found in Appendix D. It follows that the results for choices of $R_{\rm env} > 5\,R$ are also less than 10%, since such environment scales are between our fiducial choice $R_{\rm env} = 5\,R$ and the fixed environment scale. This level of difference, as we will see later, is negligible compared to the difference between GR and MG that we are considering. Thus, our main conclusions are insensitive to the definition of environment.

### 3.5.4 Conditional first-crossing distributions

#### 3.5.4.1 Unconditional First Crossing of a Moving Barrier

The distribution of the first crossing of a general barrier by a Brownian motion has no analytic solutions except for some simple barriers, *e.g.*, flat (4) and linear (119, 120). Unfortunately neither of these is a good approximation to our barriers in Fig. 3.4. As a result, we follow (140) and numerically compute this distribution. We briefly review their method for completeness.

Denote the unconditional probability that a Brownian motion starting off at zero hits the barrier $b(S) > 0$ for the first time in $[S, S + dS]$ by $f(S)\mathrm{d}S$. Then, $f(S)$, the probability density, satisfies the following integral equation

$$f(S) = g(S) + \int_0^S \mathrm{d}S' f(S') h(S, S'), \tag{3.44}$$

in which

$$\begin{aligned} g(S) &\equiv \left[\frac{b}{S} - 2\frac{\mathrm{d}b}{\mathrm{d}S}\right] P\left(b, S\right), \\ h(S, S') &\equiv \left[2\frac{\mathrm{d}b}{\mathrm{d}S} - \frac{b - b'}{S - S'}\right] P(b - b', S - S'), \end{aligned} \tag{3.45}$$

where for brevity we have suppressed the $S$-dependence of $b(S)$ and used $b' \equiv b(S')$ and

$$P(\delta, S)\mathrm{d}\delta = \frac{1}{\sqrt{2\pi S}} \exp\left[-\frac{\delta^2}{2S}\right] \mathrm{d}\delta. \tag{3.46}$$

Equation (3.44) can be solved numerically on an equally-spaced mesh in $S$: $S_i = i\Delta S$ with $i = 0, 1, \cdots, N$ and $\Delta S = S/N$. The solution is (140)

$$\begin{aligned} f_0 &= g_0 = 0, \\ f_1 &= (1 - \Delta_{1,1})^{-1} g_1, \\ f_{i>1} &= (1 - \Delta_{1,1})^{-1} \left[g_i + \sum_{j=1}^{i-1} f_j (\Delta_{i,j} + \Delta_{i,j+1})\right], \end{aligned} \tag{3.47}$$

where we have used $f_i = f(S_i)$ and similarly for $g_i$ to lighten the notation, and defined

$$\Delta_{i,j} \equiv \frac{\Delta S}{2} h\left(S_i, S_j - \frac{\Delta S}{2}\right). \tag{3.48}$$

We have checked that our numerical solution matches the analytic solution for the flat-barrier crossing problem.

#### 3.5.4.2 Conditional First Crossing of a Moving Barrier

The unconditional first crossing distribution, which relates directly to the void size distribution function in the ΛCDM model, is not particularly interesting in the chameleon model. This is because spherical underdensities in different environments will follow different evolution paths. If it is in the environment specified by $(S_{\rm env}, \delta_{\rm env})$, then $(S_{\rm env}, \delta_{\rm env})$ should be the starting point of the Brownian motion trajectory. In other words, we actually require the distribution *conditional on* the trajectory passing $\delta_{\rm env}$ at $S = S_{\rm env}$; we write this first-crossing distribution as $f(S, \delta_{\rm v}(S, \delta_{\rm env}) \mid S_{\rm env}, \delta_{\rm env})$, showing explicitly the $\delta_{\rm env}$ dependence of $\delta_{\rm v}$. The numerical algorithm to calculate the conditional first crossing probability is a simple generalization of the one used above to compute the unconditional first crossing probability (104) and is not presented in detail here.

Note that the preceding algorithm assumes the barrier $b(S) > 0$, while our void-formation barriers are strictly negative. However, if solving the problem by a Monte Carlo method we could note that the resulting first-crossing distribution is invariant under reflecting the Gaussian random walks about $\delta = 0$ (since each step of each walk is equally likely to move to higher or lower $\delta$). Thus, we can solve the distributions for our negative barriers by using $b(S) = |\delta_{\rm v}(S)|$ in the above algorithm.

Furthermore, the preceding algorithm describes the calculation of the first-crossing probability for the fixed-environment approximation, in which a single starting point $(S_{\rm env}, \delta_{\rm env})$ for a given barrier $\delta_{\rm v}(S, \delta_{\rm env})$ is sufficient. To implement the moving environment approximation we calculate a new first-crossing distribution for each underdensity scale $S$, where

the walk starts at $S_{\rm env}(R_{\rm env})$ and $R_{\rm env} = 5R(S)$ as described in Sec. 3.5.3. Our final result for the conditional first-crossing probability is then $f(S, \delta_{\rm v}(S, \delta_{\rm env}) \mid S_{\rm env}(S), \delta_{\rm env})$, where the dependence of $S_{\rm env}$ on $S$ is written explicitly.

In the special case where the barrier is flat, $\delta_v(S, \delta_{\rm env}) = \delta_{\rm sc}$, $f(S, \delta_{\rm v}(S, \delta_{\rm env}) \mid S_{\rm env}(S), \delta_{\rm env})$ is known analytically as

$$f = \frac{|\delta_{\rm sc} - \delta_{\rm env}|}{\sqrt{2\pi}\,(S - S_{\rm env})^{3/2}} \exp\left[-\frac{(\delta_{\rm sc} - \delta_{\rm env})^2}{2\,(S - S_{\rm env})}\right], \tag{3.49}$$

where again $S_{\rm env} = S_{\rm env}(S)$, so that in the next section we compare first-crossing distributions for GR and MG both calculated using the same moving environment scale.

#### 3.5.4.3 Results

Figure 3.5 shows the first-crossing distribution of voids in different environments. In general, we find all voids today with radii $R_f \gtrsim 1$ Mpc/$h$ are more numerous in chameleon models, for all environments. This difference from ΛCDM is larger for overdense environments. This is a consequence of previous results of this paper, namely that the fifth force is relatively stronger for denser environments.

Next, consider fixing the environment density. In this case, the fractional difference of the number density between chameleon models and GR tends to be greater for larger voids (larger $\nu \equiv \delta_{\rm sc}^2/S$ or smaller $S$), as indicated by the increase of $\Delta f/f$ with $\nu$ in the figure. For example, in the environment of $\delta_{\rm env} = 0.8$, voids with $R_f = 5$ Mpc/$h$ may be 2 to 3 times more common than those in ΛCDM, and 10 times more for $R_f = 25$ Mpc/$h$. This difference may seem surprisingly large, but such a case may be too rare to be observed. If one smooths the initial density field with a filter size much greater than $R = 15$ Mpc/$h$ (corresponding to $R_f = 25$ Mpc/$h$), the probability distribution of the overdensity will be a narrow Gaussian with zero mean. The chance of having a linearly-extrapolated $\delta_{\rm env} = 0.8$ should be very low; the odds of such an environment developing voids of $R_f = 25$ Mpc/$h$ or larger with $\delta = -0.8$ will be even less. Therefore, it might be difficult to find large voids in

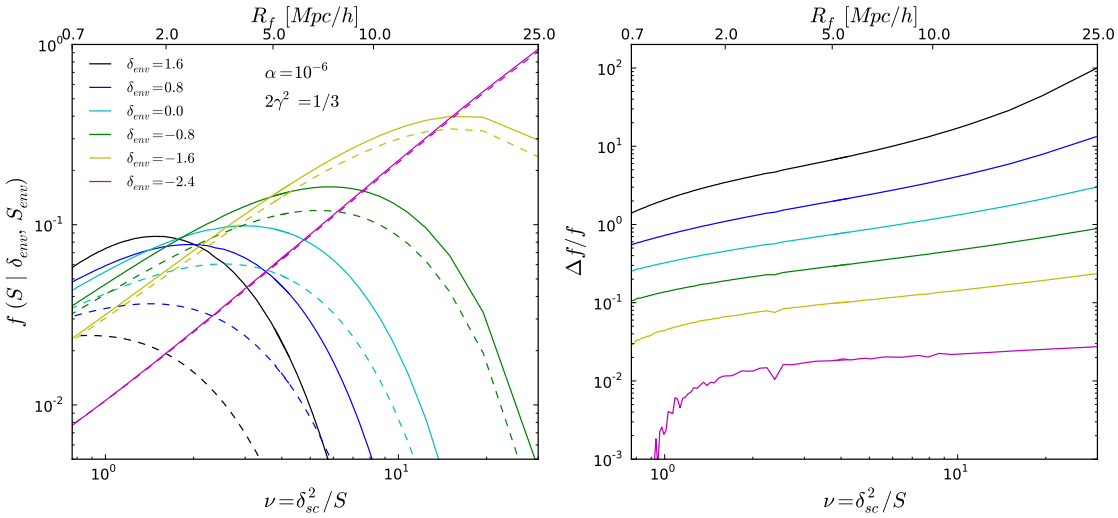


**Figure 3.5:** *Left:* First crossing distribution functions for different environments as indicated by $\delta_{\rm env}$. Solid lines are in chameleon cosmology with our fiducial model parameters. The top $x$-axis labels the corresponding final void radius when the density contrast of a void reaches $\delta = -0.8$. In bottom $x$-axis, $\delta_{\rm sc} = -2.76$ is the shell-crossing barrier for voids in ΛCDM, and $S = \sigma^2(M)$ is the variance of a spherical top-hat region. *Right:* Fractional differences of the first crossing distributions between GR and chameleon cosmology for different environments.

very overdense environments, where the predicted difference between models is expected to be larger. In reality, most large-scale environments are very close to the cosmic mean, i.e., $\delta_{\rm env} \sim 0$. In this case, the difference between models indicated by $\Delta f/f$ is less extreme but still very significant, being $\approx 100\%$ for $R_f = 5$ Mpc$/h$ and $\approx 300\%$ for $R_f = 25$ Mpc$/h$. We shall see in the next subsection that this difference is indeed close to the case where the average over all environments is taken.

The environmental dependence of model differences in the conditional first crossing distribution of voids is just the opposite as that for halos for reasons we have explained in Sec. 3.5.2. The halo mass function (72) is found to differ more from its ΛCDM counterpart in underdense environments.

The fact that $\Delta f/f$ is larger for larger voids might seem counter-intuitive, as we have shown that the relative strength of the fifth force is smaller for larger voids, hence the difference in their expansion velocities and sizes today are relatively smaller. However, the difference in the number density of voids is also related to the shape of the void size distribution function. Consider that $f$ is a very steep function of $\nu$ when $\nu$ is large. A small increment in $R_f$ or $\nu$ can therefore lead to a relatively large change in $f$.

In principle, if $f_{\rm MG}$ is larger than $f_{\rm GR}$ for large voids, the opposite should be true for small voids, namely the abundance of small voids will be lower in chameleon models. This is expected from the normalization of the first-crossing probability. Picturing this in the excursion set theory, in chameleon theories Brownian motions are likely to cross the barrier at a slightly earlier 'time', i.e. small $S$, corresponding to large voids. Correspondingly, the probability of a Brownian motion to survive for longer and cross the barrier at large $S$ is reduced – voids of smaller sizes are (relatively) rarer than in ΛCDM. Therefore, the solid and dashed lines in Fig. 3.5 will cross each other at some small $\nu$ that is not plotted, namely the abundance of small voids can be lower in chameleon models. In fact, such a crossing point is also expected for halos, which has been shown to be at $S \lesssim 10$ for the environments under consideration (72). For voids, the crossing points are found to appear at much larger

$S$. This is likely due to the halo barriers leveling off at $S \sim 5$, while the void barriers continue to steepen towards larger $S$.

In real observations, one needs to have tracers like galaxies or galaxy clusters to define void walls. If the size of the void is comparable to that of the tracers, then the walls will be lumpy. Voids with radii comparable or smaller than the typical size of virialized objects are therefore not well defined and of little interest. We do not show results deeply into this regime. In the range of empirical interest, we only see the lines of $f_{\rm MG}$ and $f_{\rm GR}$ crossing each other for the case of $\delta_{\rm env} = -2.4$ at $R \sim 1$ Mpc$/h$, which should be a rare situation. Thus, for denser environments we always expect to find more voids in chameleon models at all empirically meaningful sizes.

The environmental dependence of the differences between models may provide useful guidelines for testing gravity. In overdense environments, one may want to look at the statistics of large voids as the difference with ΛCDM may be larger, while in underdense regions, the difference in halo population may be larger therefore halo number densities may be more interesting to analyze. We summarize these two cases as void-in-cloud and cloud-in-void. However, both of these two cases are relatively uncommon to find in the real universe so that the statistics may be poor. In this case, using most of the observed volume could provide better constraints since the sample of voids and halos would be larger. It is therefore interesting to determine the overall difference between models once we average over all different environments.

### 3.5.5 Environment-averaged first-crossing

To get the average first crossing distribution of the moving barrier, we must integrate over all environments. The distribution of $\delta_{\rm env}$, denoted as $q(\delta_{\rm env}, \delta_{\rm c}, S_{\rm env})$, in which $\delta_{\rm c}$ is the critical overdensity for spherical collapse in the ΛCDM model, is simply the probability that the Brownian motion passes $\delta_{\rm env}$ at $S_{\rm env}$ and never exceeds $\delta_{\rm c}$ for $S < S_{\rm env}$ (because otherwise

the environment itself has collapsed already). This has been derived by (4):

$$q(\delta_{\rm env}, \delta_{\rm c}, S_{\rm env}) = \frac{1}{\sqrt{2\pi S_{\rm env}}} \exp\left[-\frac{\delta_{\rm env}^2}{2S_{\rm env}}\right] - \frac{1}{\sqrt{2\pi S_{\rm env}}} \exp\left[-\frac{(\delta_{\rm env}-2\delta_{\rm c})^2}{2S_{\rm env}}\right], \quad (3.50)$$

for $\delta_{\rm env} \leq \delta_{\rm c}$ and 0 otherwise. Again, we have $S_{\rm env} = S_{\rm env}(S)$, so that the distribution $q$ changes for each void size. For smaller smoothing length (larger $S_{\rm env}$), the pdf of $\delta_{\rm env}$ is wider so that the very overdense and very underdense environments are more likely to be sampled.

Then the environment-averaged first crossing distribution will be

$$f_{\rm avg}(S) = \int_{-\infty}^{\delta_{\rm c}} q \times f(S, \delta_{\rm v}(S, \delta_{\rm env}) \mid S_{\rm env}(S), \delta_{\rm env})\, {\rm d}\delta_{\rm env}. \quad (3.51)$$

The environment-averaged first-crossing distribution and void volume function are related by

$$\frac{{\rm d}n}{{\rm d}V}{\rm d}V = \frac{\bar{\rho}_m}{M} f_{\rm avg}(S) \left|\frac{{\rm d}S}{{\rm d}V}\right| {\rm d}V\,, \quad (3.52)$$

where V is the final volume of the void given by

$$V = \frac{M}{\bar{\rho}_m} \times (1.71)^3\,. \quad (3.53)$$

The factor of $1.71^3$ results from our void formation criteria of nonlinear density $\delta = -0.8$. By mass conservation, such an underdensity which was originally at the cosmic mean has grown to 1.71 times its initial comoving radius.

The left and right panels of Fig. 3.6 show the environment-averaged first-crossing distribution and the corresponding void volume function, respectively. Comparing the environment-averaged void distribution functions between our fiducial chameleon model and ΛCDM, we find the fractional difference in the number density of voids between the two models increases with void size. At $R_f \sim 25$, one may expect to find 2 to 3 times more voids in chameleon

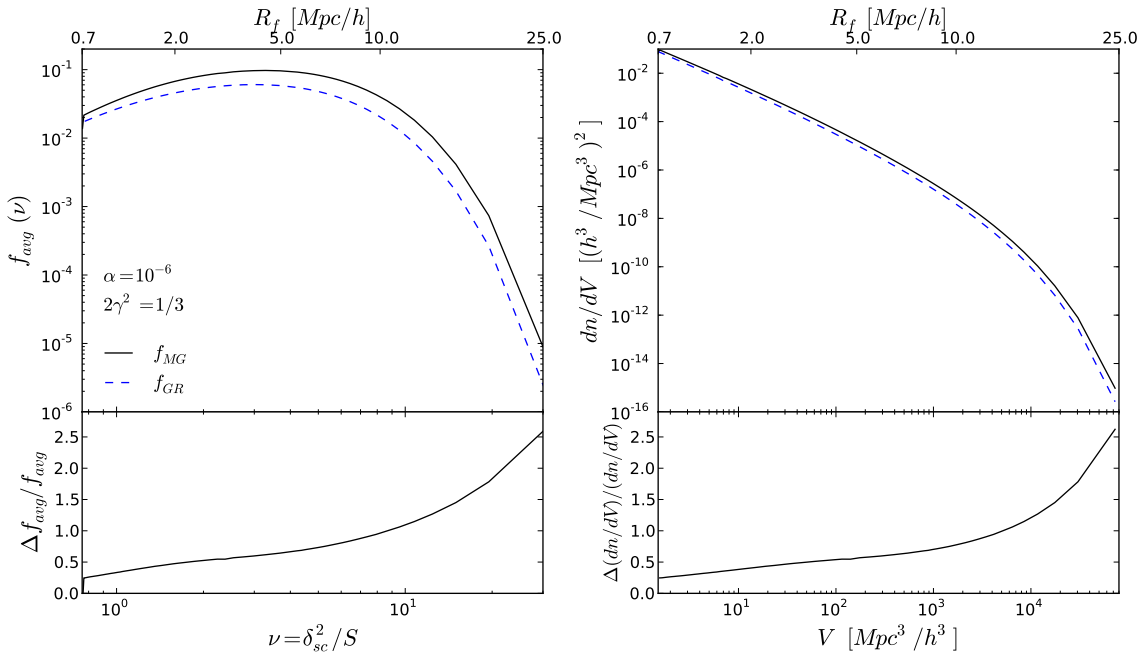


**Figure 3.6:** *Left panel:* Compares the averaged first crossing distribution functions between chameleon model (solid line) and GR (dashed line). The fractional difference is shown in the bottom panel. *Right panel:* Void volume distribution functions and their fractional difference. The difference in the number density of voids between the two models increases monotonically with void size.

models, and such a difference will keep increasing for larger voids. This level of difference in the void population is much greater than that in halos, where the difference of mass function is found to be no more than 20% (72): a factor of 10 times smaller difference. The boost of probability for having large voids in chameleon models has interesting implications for observation, thus serving as a powerful test of gravity theories. Given a finite survey volume, one can simply count the number of voids greater than a certain radius, e.g., $R_f > 25$ Mpc/$h$ to find out the number density of them and then compare it with different models.

### 3.5.6 Theory Variations

Up to this point, we have only shown results for our fiducial chameleon theory, with parameters $\alpha = 10^{-6}$ and $2\gamma^2 = 1/3$. Figure 3.7 shows the effect of varying these two parameters on the volume function, $\mathrm{d}n/\mathrm{d}V$. Focusing on the leftmost panels we see the models with $2\gamma^2 = 1/3$, which correspond most closely to the $f(R)$ class of theories. In moving from $\alpha = 10^{-5}$ to $10^{-7}$ the fractional difference changes by a factor $\sim 3$ for small voids ($V = 7{\times}10^2$ (Mpc/$h$)$^3$) and by $\sim 25$ for voids two orders of magnitude larger ($V = 7 \times 10^4$ (Mpc/$h$)$^3$).

A direct comparison of this chameleon theory with $f(R)$ models is not possible, but comparing the compton wavelengths can give some idea of the differences. For the $f(R)$ model of Hu & Sawicki (52), the compton wavelength in the background density today is $\sim 3$ Mpc/$h$ for $|f_{R0}| \sim 10^{-6}$. Our fiducial model has a longer compton wavelength: for $2\gamma^2 = 1/3$ we have $\lambda \sim 2\sqrt{10^8\alpha}$. Thus for $\alpha = 10^{-6}$, $\lambda \sim 20$ Mpc/$h$.

As it is also interesting to put constraints on the coupling $2\gamma^2$ (e.g., (**?** )), we show such variations in the center and right panels of Fig. 3.7. As we expect, for fixed $\alpha$ the deviations are much larger for stronger couplings. Again the largest, rarest voids are most sensitive to these changes due to the steepness of the volume function there: for $\alpha = 10^{-5}$ the deviation of the volume function from the GR result grows by a factor of 10 in moving from $2\gamma^2 = 1/3$ to $2\gamma^2 = 1$.

The comparison to results for the excursion-set mass function highlights the promise of using voids to constrain modified gravity. Consider the case in Fig. 3.7 with the smallest deviations from GR, $\alpha = 10^{-7}$ and $2\gamma^2 = 1/3$. The fractional difference in the volume function is 30-60% over at least two decades in void volume. The deviation of the mass function predicted by this model peaks at 5% for halo masses $\sim 10^{13} M_\odot/h$, falling quickly for smaller and larger halos (72). Thus, if the difference between models is integrated over the entire range of halo and void number densities, the total constraining power of the void statistics will be much greater. This larger difference in the void statistics is a result of several effects: A.) the upper bound in the ratio of gravity and the fifth force does not apply to underdensities and B.) the crossing point of GR and MG first-crossing distributions expected due to the normalization of the distribution occurs for voids which are too small to be empirically relevant. Thus, the MG void volume function shows large deviations at all void sizes.

In Appendix E we discuss the effect of varying $\alpha$ and $\gamma$ on the conditional first-crossing distributions, i.e., before the environment averaging is carried out.

## 3.6 Discussion

We have explored the physics of the fifth force in voids for chameleon models and applied it to understand the impact on void properties. In scalar-tensor theories, such as chameleon MG, the smooth part of the scalar field is the source of the cosmological constant, known to act like a repulsive force. This is common in both a ΛCDM universe and a chameleon universe. The coupling of the scalar field to mass density causes an additional spatial fluctuation of gravity, i.e., the fifth force. This is the only difference for void evolution between chameleon and ΛCDM models. The evolution of voids in MG is affected by the Newtonian force, the dark energy force and the fifth force.

The following interesting features are found in comparison to a ΛCDM universe, some of which may be used to test gravity in laboratory experiments and observational data, or

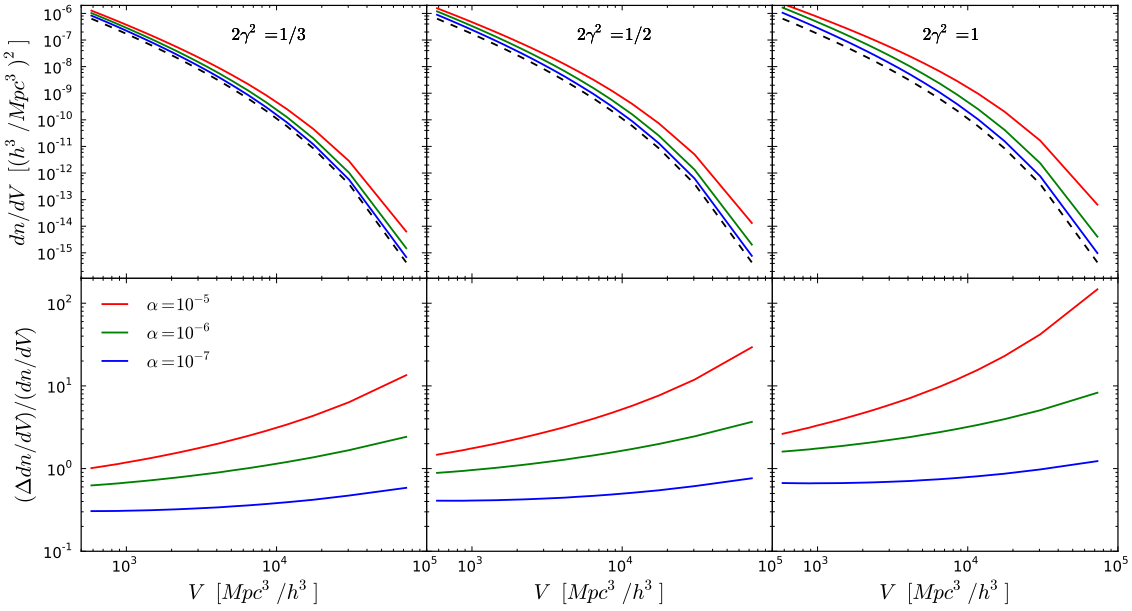


**Figure 3.7:** *Left panels*: The void differential volume function for our chameleon model with $2\gamma^2 = 1/3$ (solid lines) compared to GR (dashed). Various values of $\alpha$ are shown, ranging over $10^{-5}, 10^{-6}$, and $10^{-7}$, from top to bottom. The lower panel shows the fractional difference from the GR result. *Center panels*: The same, but for coupling $2\gamma^2 = 1/2$. *Right panels*: The same, but for coupling $2\gamma^2 = 1$. Even for $\alpha = 10^{-7}$, $2\gamma^2 = 1/3$ where the deviation is weakest, it is above 30% for all empirically interesting void sizes.

to guide more precise predictions from cosmological $N$-body simulations.

1.) The fifth force in voids is a type of 'anti-gravity'. It points outwards from the center of the void, opposite to the direction of normal gravity. This is because the slope of the scalar field profile is negative in voids.

2.) In principle, the amplitude of the fifth force can be very large in voids. In halos, its magnitude can be no more than $2\gamma^2$ (1/3 in our fiducial model) of normal gravity. Due to the breakdown of Birkhoff's theorem, the scalar field profile and hence the fifth force are functions of the matter density inside and outside the void region, as well as its size.

This property leads us to suggest a possible laboratory test of gravity using a vacuum chamber. To create a chamber inside of which the fifth force is dominant, it should have a thick chamber wall made of high density material. This is to enlarge the density contrast between the chamber interior and the wall so that fifth force strength is maximized. The wall needs to be thick to have enough space for the scalar field to reach its minimum in the wall. Walls of the chamber and test particles (detectors) in the chamber should feel the fifth force pushing outwards, but very little gravity (as long as the chamber is close to real vacuum). In the neighborhood of the earth, the background density is non-zero. There is dark matter from the Milky Way halo, and maybe some baryonic dust; these two should contribute a haze of mass density inside any vacuum chamber. This may set the limit for the density contrast and the amplitude of the fifth force. Furthermore, although the ratio $F_5/F_{\rm N}$ may be large in this case, we know that $F_{\rm N}$ is quite small in the chamber, so that the large ratio does not necessarily imply a large fifth force. The effect of the dark energy force also needs to be accounted for. We leave the quantitative investigation of this experiment to future work.

3.) Driven by the additional fifth force, individual voids expand faster and grow larger

than their ΛCDM counterparts. The fractional difference in void radius and expansion velocity is larger for small voids in overdense environment (void-in-cloud), at the level of $\lesssim 10\%$ and $20-30\%$ respectively, for voids of a few Mpc/$h$. For the same reason, voids of the same size should be emptier in chameleon models. This leads to interesting observational consequences. A.) In redshift space, due to the faster expansion of voids, a small void-in-cloud may be more elongated along the line-of-sight due to redshift space distortion. B.) Void profiles may be steeper as voids empty themselves more quickly, as has been shown in Martino & Sheth (80). We plan to investigate both of the above by stacking voids in simulations. Recent work has shown that the lensing signal from stacked voids in future surveys will provide information on their radial profile (65). This may provide a complimentary probe to void statistics for distinguishing between gravity models.

4.) For individual voids, the largest difference between GR and MG is found in void-in-cloud systems, while for voids statistics, the large voids differ more. The fractional difference in the number density of voids increases with size and is ∼10 times larger than the corresponding difference for halos. The chance of having voids with $\delta \sim -0.8$ with $R \sim 25$ Mpc/$h$ is 2.5 times larger than in ΛCDM. A conceptually simple observational test would be to count the number of very large halos in a volume limited sample, and find out the probability for that count to occur within different gravity models.

In fact, the detection of the CMB Cold Spot in the WMAP data, if interpreted as the ISW signal, has already imposed a constraint on this probability. The size of the void in the large-scale structure needed to generate the size and amplitude of the Cold Spot is estimated to be at the order of 100 Mpc/$h$ in radius, which may not be consistent with a ΛCDM universe (e.g. 9, 23, 54, 82, 110). Similarly, the detected ISW signal from the stacking of 4-deg$^2$-size regions of the CMB corresponding to the SDSS super clusters and super voids is found to be $2-3\sigma$ higher than that expected in a ΛCDM universe (35, 102). Recent work has shown that the abundance of the largest voids in ΛCDM simulations may be too small

to match observations (130). All of these discrepancies, if confirmed, seem to indicate that very large structures in the universe are perhaps larger and more abundant than expected in a ΛCDM universe. The fact that the abundance of large voids in modify gravity can be much greater than in ΛCDM suggest that modify gravity can somewhat release the tension imposed by those observations, but precise quantitative predictions are beyond the reach of the spherical collapse model and excursion set theory.

Intriguingly, there are also observations suggesting that galaxies are less common in low density regions than expected in the standard cosmology (e.g. 131). The Local Void (within the radius of 1-8 Mpc from the center of the local group) also seems far too empty based on the galaxy number density (e.g. 105, 106, 131), but see Tinker & Conroy (132) for a different view. There is also an unexpected presence of large galaxies on the outskirts of the Local Void (106). "These problems would be eased if structure grew more rapidly than in the standard theory, more completely emptying the Local Void and piling up matter on its outskirts" (106). Voids in chameleon models seem to coincide qualitatively with these observations. However, the complexity of galaxy formation, especially its dependence on environment, is a hard barrier to overcome before any conclusive results can be drawn.

We note that our results for void statistics should be qualitatively similar in other models with chameleon screening, such as $f(R)$ (52). Furthermore, while symmetron (42, 43) and environmentally-dependent dilaton (7, 24) theories rely on conceptually different mechanisms to screen the fifth force, the qualitative picture of Fig. 3.1 is unchanged. The minimum of the symmetron and dilaton fields will again be higher inside an underdensity than outside, thus leading to a repulsive fifth force which will aid the dark energy in speeding up void growth.

**Caveats:**

Throughout the paper, we employ the spherical collapse model and excursion set theory for studying the evolution of individual voids and their distribution functions. However:

1. Voids in the real universe are not perfectly spherical. (e.g. 116).

2. The excursion set theory for voids may not be able to match precisely voids found from simulation or observation. There are obvious reasons for this:. A.) It has been noticed that the total volume of voids given by this model exceeds that of the universe (121). This is certainly not physical. One obvious reason is that some 'voids' may be embedded in overdense regions whose density reaches the collapsing barrier. This is the void-in-cloud problem, which is more acute for small voids. Accounting for it can resolved the problem to some extent, but not fully (103, 121). Another reason is that there is an underlying assumption that voids can expand forever, which is also unphysical. The expanding walls of voids will certainly meet their neighbors and cross each other. This is probably more complicated to fix and is beyond the scope of this paper.

3. Our results are for voids in the dark matter distribution, whereas observed voids must be defined with respect to galaxies. The excursion set theory of the void population has been extended to these more empirically relevant voids by Furlanetto & Piran (33).

In this paper, we are mostly comparing the difference between two models rather than the accuracy of each model itself. Thus, these well-known limitations of the basic excursion set theory of voids may affect MG and ΛCDM in roughly the same way, leaving the difference mostly unaffected. We therefore neglect these problems, and leave the calibration of the theory to simulation for future work.

# Chapter 4

# Detection of Stacked Filament Lensing Between SDSS Luminous Red Galaxies

## 4.1 Introduction

One of the most striking features of N-body simulations is the network of filaments into which dark matter particles arrange themselves. Some attempts to quantify this network have been made (13, 124). Other work has attempted to study the largest filaments, those between close pairs of large dark matter halos (18). Such filaments are likely the easiest to identify in data, e.g., Zhang et al. (141) look for overdensities in the galaxy distribution between close pairs of galaxy clusters. However, since filaments include both dark and luminous matter, weak lensing techniques are useful to understand the entire structure: Dietrich et al. (26) and Jauzac et al. (59) both identify single filaments by focusing on a weak lensing analysis of individual cluster pairs.

In this study we measure the weak lensing signal of filaments between stacked Luminous Red Galaxy (LRG) pairs in Sloan Digital Sky Survey (SDSS) data. The mass distribu-

tion and therefore weak lensing shear in the neighborhood of LRG pairs is dominated by the massive halos themselves. Methods which aim at filament detection, e.g., Maturi & Merten (83), may have large degeneracy with the signal from these nearby halos. In the face of this degeneracy, we construct an estimator of the lensing signal which removes the shear due to these halos, assuming only that they are spherically symmetric. We will show that this technique is sufficient to obtain a detection, and some physical implications on filament size and shape can be extracted by comparison to filament models. Systematic errors which are expected to be spherically symmetric with respect to the halos, such as intrinsic alignments, are nulled simultaneously.

Other work has attempted to estimate the feasibility of weak lensing stacked filament detection. Maturi & Merten (83) make optimistic choices for survey parameters and find that $\sim 2-4\sigma$ detections are possible for single clusters but state that their method has difficulties in application to stacked filament detection. In another study (84) use lens and source redshifts that make their lensing strength a factor of 2 greater than ours, and a galaxy number density at least a factor of 30 higher. The lower mass limit of their stacked clusters is $M_{200} = 4 \times 10^{14} M_{\odot}/h$, much larger than the dark matter halos associated with our LRGs. With these parameters, they estimate that $\sim 20$ cluster pairs are necessary to obtain a detection. We have $\sim 200,000$ pairs of LRG halos, and have been able to obtain a detection without new ground or space data.

Filaments can also be characterized using the language of higher-order correlations. In this case, one would describe the filament as the part of the matter-matter-matter three point function in the neighborhood of the halos forming a cluster pair. A detection of the halo-halo-matter 3-point function around such cluster pairs was made using the Red Cluster Survey (122). More recently Simon et al. (123) used CFHTLens survey to measure the galaxy-galaxy-shear correlation function and attempted to measure the average mass distribution around galaxies. This measurement was done by subtracting off the two point contribution of the lensing signal. As these authors discovered, the three-point signal peaks at the cluster

locations. However, for our purposes of identifying filaments, such a location of the three point function's peak makes the technique of two-point subtraction unsatisfactory. Just as our nulling estimator removes two-point contributions which are spherically symmetric about the halo centers, it also removes any three-point contribution which is centered on these points.

The outline of this paper is as follows: section 4.2 describes the basic nulling technique for removing spherically symmetric components, as well as an additional subtraction for removing constant biases in the shear catalog. In section 4.3 the LRG pair catalog and background source shear catalog used in this work are described. Section 4.4 contains a derivation of the halo model's expected filament signal, which arises due to the three-halo term. In addition we describe an alternative thin-filament model. In section 4.5 we present our main results, including the results of the filament measurement, null tests, and comparison of the halo model prediction to the data. Finally, section 4.6 discusses the implications of our results, and summarizes what we have learned about dark matter filaments.

Throughout this work we use cosmological parameters $\Omega_{\rm m} = 0.3$, $\Omega_\Lambda = 0.7$, and $\sigma_8 = 0.83$.

## 4.2 Measurement Technique

In this section, we describe the nulling technique for spherically symmetric components, which includes most of the two-point signal and the peak of the three-point signal. We also describe an additional subtraction which removes contributions from constant shear biases.

### 4.2.1 Nulling spherical components

We bin the data in such a way as to null the shear signal from any spherically symmetric source at the location of either member of the halo pair. To first order, such halos are

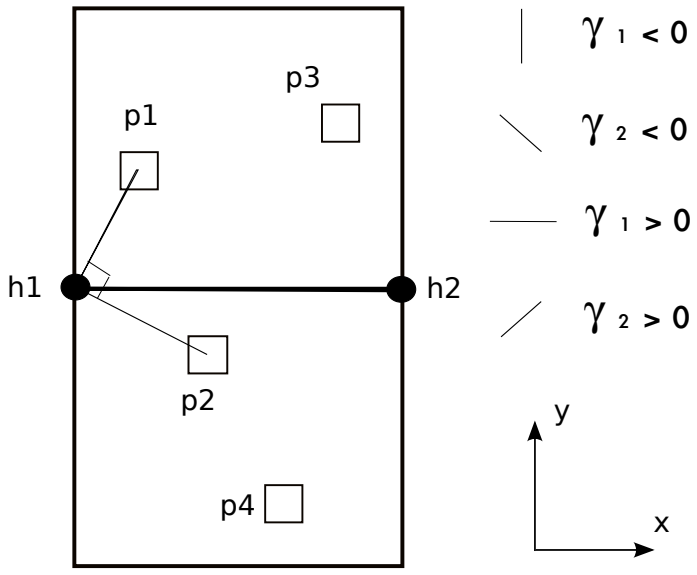


**Figure 4.1:** Combining data in points p1-p4, the average shear signal from spherical halos h1 and h2 is zero. The point "p2" is the counter point of "p1" with respect to halo "h1", while the points "p3" and "p4" are the counterparts of p2 and p1 with respect to halo "h2", respectively. This nulling method only works when all shears are measured relative to the fixed Cartesian coordinate system on the sky (as indicated at bottom right). Our convention for the sign of the two shear components is given by the $\gamma_1$ and $\gamma_2$ whiskers.

expected to follow a spherically-symmetric NFW density distribution (92) when stacked. However our technique is not dependent on the precise shape of the halo profile, only on its spherical symmetry. We note that halo anisotropy which is preferentially aligned with the inter-pair direction would not be nulled by the following procedure, but its small contribution is treated in Appendix F.

First consider just one spherically symmetric halo, h1, as pictured in Fig. 4.1. Pick any point p1 nearby. Draw another point p2 which is (i) 90 degrees away from p1 with respect to the halo, and (ii) at the same distance from the halo as p1. The tangential shears $\gamma_t$ from these points add, while the cross component $\gamma_\times$ is zero. This is the standard galaxy-

galaxy lensing measurement. But if the shear components at p1 and p2 are measured with respect to a fixed coordinate system on the sky, they average out to zero. We denote the shear components relative to this fixed Cartesian coordinate system $\gamma_1$ and $\gamma_2$. As shown in Fig. 4.1, we choose this coordinate system such that $\gamma_1 < 0$ is perpendicular to the $x$-axis, and $\gamma_1 > 0$ is parallel.

Now add a second halo, h2. We need to null the h2 shear signal in both p1 and p2 as well. To do so, rotate both points by 90 degrees about h2 to make points p3 and p4. By construction, the average $\gamma_1$ and $\gamma_2$ shear signal measured at these four points has no contribution from a spherical halo at h2. Furthermore, one can check that rotating p3 by 90 degrees about h1 brings it into p4, so that this set of four points is null with respect to both halos. Again note that we are summing the *Cartesian* components of the four shears.

Such sets of four points are the building blocks for a number of possible binning schemes which attempt to null the spherically-symmetric halo signal. Note that any set of bins which exploit this property will necessarily mix scales relative to the hypothesized filament. However, since the most likely location for an inter-halo filament is on the line connecting the halo pair, we choose bins which will minimize this mixing of scales. The background shears are separated into bands that run parallel or perpendicular to the filament direction: these are marked as the "Signal region" on the left side of Fig. 4.2. The first two such bins are numbered on the figure. This binning scheme also exploits the expected symmetries about the center of the filament, in both horizontal and vertical directions. To verify that a bin does indeed fulfill the conditions for nulling the spherical signal mentioned above, imagine rotating the part of the bin above the $R_{\rm pair}$ line about either halo, and see that it goes into the same colored bin in the region below the line. Note also that each background source is counted twice due to the overlap between different bins. This means a naive shape noise accounting of errors would underestimate the noise by a factor $\sqrt{2}$.

In what follows, we describe our measurement procedures of filament lensing. Following the method in Mandelbaum et al. (79), we use, as the lensing observable, the stacked surface

mass density field at the pixel $(x, y)$ in the region around each LRG pair (see Fig. 4.2), estimated from the measured shapes of background galaxies as

$$\Delta\Sigma_k(x, y; z_{\rm L}) = \frac{\sum_j \left[ w_j \left( \left\langle \Sigma_{\rm crit}^{-1} \right\rangle_j (z_{\rm L}) \right)^{-1} \gamma_k(\vec{x}_j) \right]}{\sum_j w_j}, \tag{4.1}$$

where the summation $\sum_j$ runs over all the background galaxies in the pixel $(x, y)$, around all the LRG pairs, the indices $k = 1, 2$ denote the two components of shear, and the weight for the $j$-th galaxy is given by

$$w_j = \frac{\left[ \left\langle \Sigma_{\rm crit}^{-1} \right\rangle_j (z_{\rm L}) \right]^2}{\sigma_{\rm shape}^2 + \sigma_{{\rm meas},j}^2}. \tag{4.2}$$

We use $\sigma_{\rm shape} = 0.32$ for the typical intrinsic ellipticities and $\sigma_{{\rm meas},j}$ denotes measurement noise on each background galaxy. Again notice that, when computing the average shear field, we use the same coordinate system for each LRG pair: taking one LRG at the coordinate origin and taking the $x$-axis to along the line connecting two LRGs as pictured in Fig. 4.1. $\left\langle \Sigma_{\rm crit}^{-1} \right\rangle_j$ is the lensing critical density for the $j$-th source galaxy, computed by taking into account the photometric redshift uncertainty:

$$\left\langle \Sigma_{\rm crit}^{-1} \right\rangle_j (z_{\rm L}) = \int_0^\infty {\rm d}z_{\rm s} \Sigma_{\rm crit}^{-1}(z_{\rm L}, z_{\rm s}) P_j(z_{\rm s}), \tag{4.3}$$

where $z_{\rm L}$ is the redshift of the LRG pair and $P_j(z_{\rm s})$ is the probability distribution of photometric redshift for the $j$-th galaxy. Note that $\Sigma_{\rm crit}^{-1}(z_{\rm L}, z_{\rm s})$ is computed as a function of lens and source redshifts for the assumed cosmology as

$$\Sigma_{\rm crit}^{-1}(z_{\rm L}, z_{\rm s}) = \frac{c^2}{4\pi G} \frac{D_A(z_{\rm s})}{D_A(z_{\rm L}) D_A(z_{\rm L}, z_{\rm s})} \tag{4.4}$$

and we set $\Sigma_{\rm crit}^{-1}(z_{\rm L}, z_{\rm s}) = 0$ for $z_{\rm s} < z_{\rm L}$ in the computation.

To increase statistics, we will measure the stacked weak lensing signal of filaments as a function of distance $R$ from the line connecting the two LRGs, rather than the two-dimensional mass distribution (see Fig. 4.2). Based on our nulling method in Fig. 4.1, each "p1" point at distance $R$ has its counterparts with coordinate values

$$\mathrm{p1}(x,R) \to \{\mathrm{p2}(R,-x), \mathrm{p3}(1-x,1-R), \mathrm{p4}(1-R,x-1)\}\,, \tag{4.5}$$

where we set the first LRG position "h1" as the coordinate center $(x,y)=(0,0)$, and we have used the units of $R_{\rm pair}=1$ for convenience. Hence we employ the following estimator of filament lensing signal for the $a$-th distance bin, $R_a$, in the signal region of Fig. 4.2:

$$\begin{aligned}\widehat{\Delta\Sigma}_k^{\rm signal}(R_a) \equiv \sum_{x_b;0<x_b<0.5} & [\Delta\Sigma_k(x_b,R_a)+\Delta\Sigma_k(R_a,-x_b) \\ & +\Delta\Sigma_k(1-x_b,1-R_a)+\Delta\Sigma_k(1-R_a,x_b-1) \\ & +\Delta\Sigma_k(x_b,-R_a)+\Delta\Sigma_k(R_a,x_b) \\ & +\Delta\Sigma_k(1-x_b,R_a-1)+\Delta\Sigma_k(1-R_a,1-x_b)]\,,\end{aligned} \tag{4.6}$$

where $\Delta\Sigma_k(x,y)$ denotes the $k$-th component of projected mass density at the position $(x,y)$ (see Eq. 5.3, but note that the sum in the denominator of Eq. 5.3 runs over all lens-source pairs in the bin when plugged into Eq. 4.6 or 4.7); the summation is over the $x$-axis bins, and the summation range is confined to $0<x_b<0.5$ in order to avoid a double counting of the same background galaxies in the different quads of points p1, ..., p4. Note however that the above binning does put each galaxy in two different bins. The third and fourth lines of Eq. (4.6) exploit the symmetry about the line joining the LRG pair, by letting $\Delta\Sigma_k(x,y)\to\Delta\Sigma_k(x,-y)$. Putting each galaxy in two bins in this way does add to our covariance between bins, but even so there is a gain in information. This is because when a galaxy is put in, say, bin 1 it is averaged together with a different set of galaxies compared to when it is placed in bin 2.

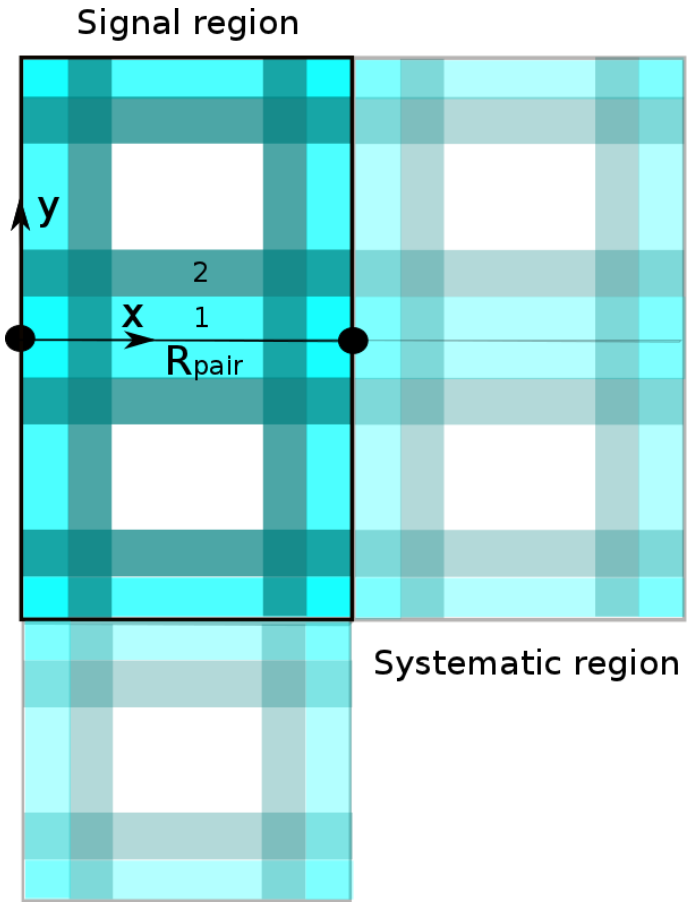


**Figure 4.2:** The lensing measurement (cross-component null test) is performed by combining all background shears' $\gamma_1$ ($\gamma_2$) components in bins, such as the pictured bins 1 and 2. We call the region including the LRG pairs the "Signal" region, where we expect the filament exists along the line connecting the two LRGs denoted by bold points. We also use the regions surrounding the Signal region, called "Systematic" regions, in order to estimate a possible coherent spurious shear signal. We will estimate the filament lensing signal by subtracting the shear signal of Systematic regions from the shear of the Signal region, as described in the text. (Note that the left and top Systematic regions of Eq. (4.7) are not pictured.)

### 4.2.2 Systematic and halo ellipticity subtraction

The standard g-g lensing measurement of tangential shears about halos is immune to some effects which are worrisome for our method. Constant spurious shear on scales larger than the halo automatically cancels out in such tangential shear measurements. The logic is very similar to that used above to null the spherically-symmetric signal: a constant shear which is present at two points rotated by 90 degrees about the halo relative to each other is cancelled when those two points are averaged in a single bin.

Since we are not measuring the tangential shear $\gamma_t$ relative to some center, another way of mitigating spurious constant shears is needed. We do this by repeating the measurement in the "Systematic region" surrounding the Signal region, as pictured on the right and lower sides of Fig. 4.2. Note that we use, but do not picture, identical systematic regions on the left and top of the Signal region. The layout of these systematic regions was chosen such that they also null the spherically symmetric signal from both halos.

Similarly to the estimator for the signal region (Eq. 4.6), we can define the estimator for the systematic regions as

$$\begin{aligned}
\widehat{\Delta\Sigma}_k^{\rm sys.}(R_a) \equiv & \sum_{x_b;0<x_b<1} [\Delta\Sigma_k(1+x_b,R_a)+\Delta\Sigma_k(1+R_a,x_b) \\
& +\Delta\Sigma_k(2-x_b,1-R_a)+\Delta\Sigma_k(2-R_a,1-x_b) \\
& +\Delta\Sigma_k(x_b,1+R_a)+\Delta\Sigma_k(R_a,1+x_b) \\
& +\Delta\Sigma_k(1-x_b,2-R_a)+\Delta\Sigma_k(1-R_a,2-x_b) \\
& +\Delta\Sigma_k(x_b-1,R_a)+\Delta\Sigma_k(R_a-1,x_b) \\
& +\Delta\Sigma_k(-x_b,1-R_a)+\Delta\Sigma_k(-R_a,1-x_b) \\
& +\text{ repeat all terms with } \Delta\Sigma_k(x,y)\rightarrow\Delta\Sigma_k(x,-y)]
\end{aligned} \tag{4.7}$$

where we again set the "h1" (first LRG) position as the coordinate center. The first and second lines on the r.h.s. denote the average shear in the right-side region from the LRG

pair (see Fig. 4.2), where we measure "fake" filament signal as a function of distance $R_a$ from the line connecting the "h2" position $(1, 0)$ and the point $(2, 0)$. Lines three and four denote the average in the upper-side region. The fifth and sixth lines denote the average in the left-side region, where we measure the signal as a function of distance $R_a$ from the line connecting the $(-1, 0)$ and the "h1" position $(0, 0)$.

Hence our estimator of the filament lensing is

$$\Delta\Sigma_k^{\rm fil}(R_a) = \sum_{\text{all LRG pairs}} \left[\widehat{\Delta\Sigma}_k^{\rm signal}(R_a) - \widehat{\Delta\Sigma}_k^{\rm sys.}(R_a)\right] \tag{4.8}$$

Note that using these regions automatically assures that our systematic regions will have the same distribution in redshift $z$, pair separation $R_{\rm pair}$, and pair orientation angle as the halo pairs themselves.

The nulling technique and systematic subtraction have the extra benefit of mostly removing contributions from halo ellipticity, expected to point along the line joining the LRG pair. The ellipticity-direction cross-correlation of Lee et al. (69) has shown that simulated dark matter halos tend to point towards other halos in their vicinity. While the intrinsic alignment of LRGs has been measured at a less significant level, the smallness of the intrinsic alignment of the galaxy ellipticity is more likely due to misalignment of the light and mass profiles (98), rather than the lack of alignment between neighboring massive halos. But if we let the virial radii of these halos be $\Delta \leq 1$ Mpc$/h$ and the pair separation be $R_{\rm pair} \geq 6$ Mpc$/h$, then the ratio of these $\Delta/R_{\rm pair}$ is a small quantity, and we show in Appendix F that contributions to the signal are highly suppressed as this ratio gets smaller.

### 4.2.3 Jackknife Realizations

We perform the measurement and all null tests by first dividing up the survey area of 8,000 sq. deg. into 32 approximately equal area regions, as shown in Fig. 4.3. We then measure each quantity multiple times with each region omitted in turn to make $N = 32$ jackknife

realizations. The covariance of the measurement (97) is given by

$$C[\Delta\Sigma_i^{\rm fil},\Delta\Sigma_j^{\rm fil}] = \frac{(N-1)}{N} \times \sum_{k=1}^{N} \left[(\Delta\Sigma_i^{\rm fil})^k - \overline{\Delta\Sigma_i^{\rm fil}}\right] \left[(\Delta\Sigma_j^{\rm fil})^k - \overline{\Delta\Sigma_j^{\rm fil}}\right] \quad (4.9)$$

where the mean value is

$$\overline{\Delta\Sigma_i^{\rm fil}} = \frac{1}{N}\sum_{k=1}^{N}(\Delta\Sigma_i^{\rm fil})^k\,, \quad (4.10)$$

and $(\Delta\Sigma_i^{\rm fil})^k$ denotes the measurement from the $k$-th realization and the $i$-th spatial bin. The covariance is measured for both components of shear; for clarity we do not denote the separate components in Eqs. 5.7 and 5.8.

## 4.3 Data

### 4.3.1 Pair catalog

We use the SDSS DR7-Full LRG catalog of Kazin et al. (62), which contains 105,831 LRGs between $0.16 < z < 0.47$. The sky coverage is approximately 8,000 sq. deg. The pair catalog is constructed by choosing each LRG in turn, and finding all neighboring LRGs within a cylinder of physical (or proper) radius 18 Mpc/$h$ and physical line-of-sight distance $\pm 6$ Mpc/$h$. The redshift distribution of our pairs is in the left panel of Fig. 4.4. The distribution in line-of-sight distance differences between the pair members is roughly uniform, as shown in the bottom right panel of Fig. 4.4. The cut-off of $\Delta r_{\rm los} < 6$ Mpc/$h$ corresponds roughly to a redshift separation of $\Delta z < 0.004$ between pairs. Note that this line-of-sight separation assumes the LRG velocity is only due to Hubble flow; in other words, the redshift difference can arise from the difference of line-of-sight peculiar velocities ($\Delta v = 1200$km/s for $\Delta r_{\rm los} = 6$ Mpc/$h$) even if the two LRGs are in the same distance. This is the so-called

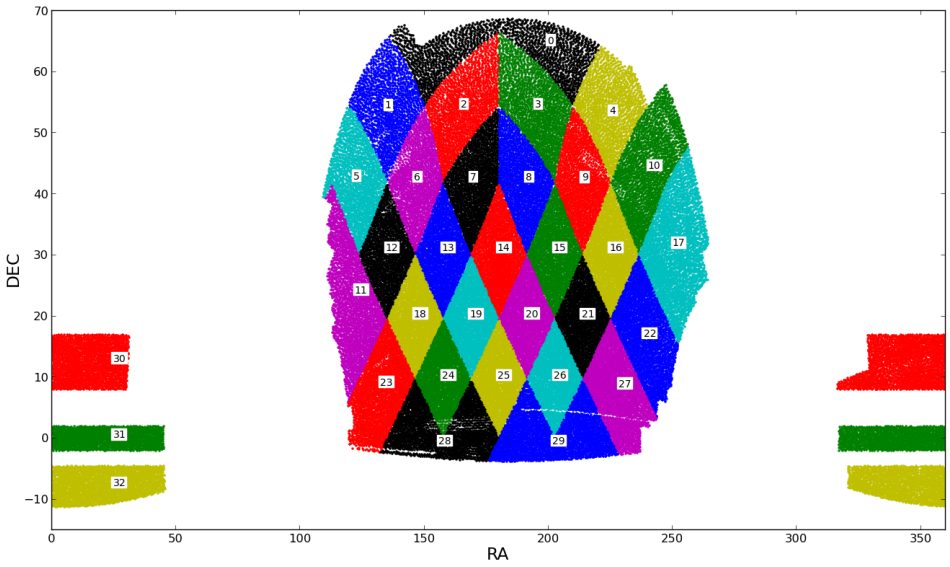


**Figure 4.3:** The SDSS footprint covered by our LRG catalog and background source galaxies. The total area is approximately 8,000 square degrees. We divide the area into 33 jackknife regions as pictured, repeating the measurement 33 times with each region omitted once, giving an estimate of the covariance matrix.

redshift space distortion (RSD), and we will discuss the effect of RSD on our weak lensing measurements.

We obtain $\sim 220,000$ pairs with the separation cutoffs given above: since each LRG can be a member of multiple pairs, this is about twice the number of objects as in the original LRG catalog. With $R_{\rm pair}$ defined to be the physical projected separation between the LRGs, for pairs between 6 Mpc/$h < R_{\rm pair} < 18$ Mpc/$h$ we have a distribution $P(R_{\rm pair})$ which grows very slightly with $R_{\rm pair}$ (Fig. 4.4, top right panel). The virial radii of these halos are $\sim 0.5 - 1.0$ Mpc/$h$, so our selection of objects with $R_{\rm pair} \geq 6$ Mpc/$h$ ensures that these LRGs live in different dark matter halos. We have checked that the measurement is insensitive to the choice of physical vs. comoving distances.

In Fig. 4.5 we show the stacked shear whiskers for the smallest $R_{\rm pair}$ bin; each lens-source pair is optimally weighted as in Eqs. (5.3) and (5.4), and we convert back to $\gamma$ by assuming fiducial redshifts $z_{\rm L} = 0.25$ and $z_{\rm s} = 0.4$. The tangential shear signal around each member of the LRG pair is clearly visible. The nearest whisker to each LRG has magnitude $\approx 0.003$. Note that due to the large distance between whiskers ($0.1 R_{\rm pair} \sim 1$ Mpc/$h$) even the closest ones to each halo are far from the center at $\sim R_{\rm vir}/2$. The dominance of the LRG halos in these fields motivates our use of the nulling scheme to isolate the relatively tiny filament lensing signal.

### 4.3.2 Background source catalog

The shear catalog is composed of 34.5 million sources, and is nearly identical to that used in Sheldon et al. (117). The source redshift distribution is shown in the left panel of Fig.and is obtained by stacking the posterior probability distribution of photometric redshift for each source, $P(z_{\rm s})$. While the peak of this source catalog is approximately at the same redshift as the peak of our LRG pairs, $z \sim 0.35$, the source distribution has a substantial tail extending out to higher redshifts. For further details of the shear catalog, see Sheldon et al. (117).

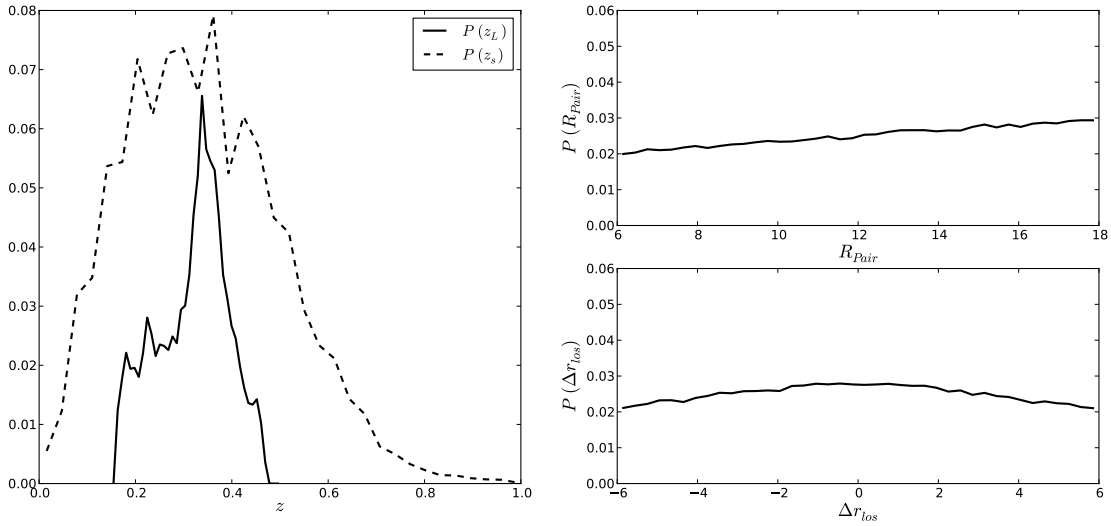


**Figure 4.4:** (*left panel*): The redshift distribution of LRG pairs used as lenses (solid line) and background sources (dashed line). (*top right panel*): The distribution of physical distances in the plane of the sky between the two members of each galaxy pair. The number of pairs rises very slowly with increasing distance. (*lower right panel*): The distribution of differences in line-of-sight distance for our LRG pairs. Note that a correction for RSD does not enter in these distances.

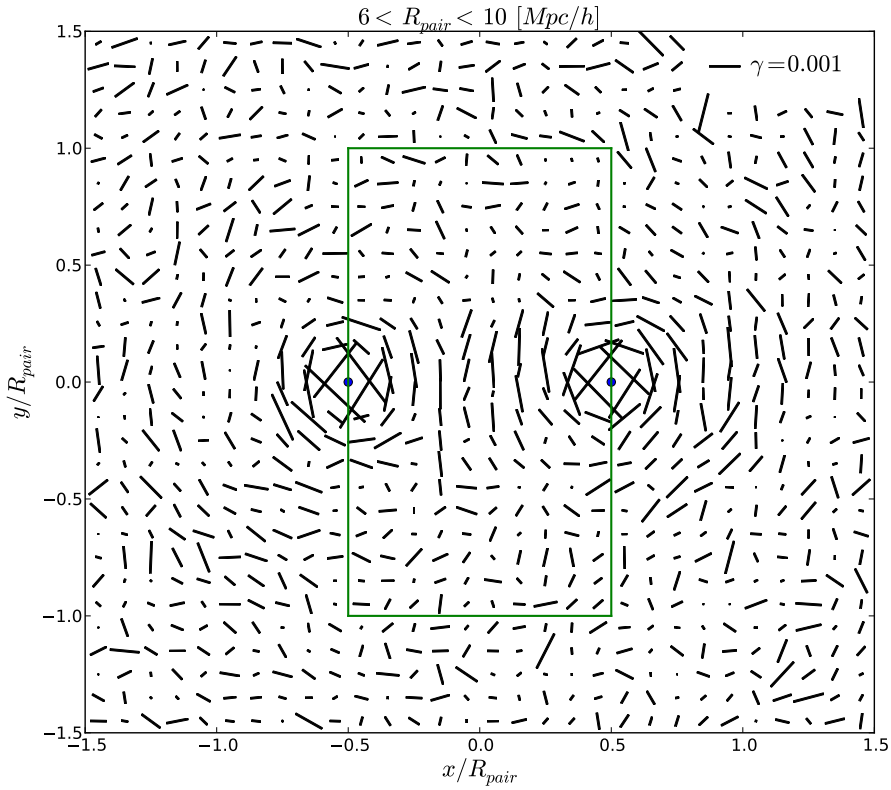


**Figure 4.5:** The stacked shear field for our smallest separation bin, 6 Mpc/$h$ < $R_{\rm pair}$ < 10 Mpc/$h$, obtained by stacking the background galaxy ellipticities in the same Cartesian coordinate system around each LRG pair region (see Fig. 4.1 and Eq. 5.3). The tangential shear signal of the LRG halos is clearly visible at the location of the blue dots. The green box pictures the Signal region of Fig. 4.2. We seek to measure the small lensing signal of filaments in these fields dominated by massive halos.

## 4.4 Theory: Thick- and thin-filament models

We compare the measurement to the following two models, which generally predict "thick" or "thin" filaments, respectively:

- the three-point halo model prediction using the halo-halo-matter bispectrum based on the perturbation theory of structure formation;
- a one-dimensional string of less massive NFW halos (a collection of NFW halos along the 1D filament).

### 4.4.1 Thick-filament from the halo model

Here we use the halo model (22, 129) to make a prediction for the size and shape of filaments between LRG pairs. We first obtain the projected mass density map around the pair of halos, based on the halo-halo-matter three-point correlation function, and then Fourier-transform the mass map to compute the shear field in order to compare with the measurements.

#### 4.4.1.1 Surface Density Map from three-point correlations

We are interested in the three-point correlation among halos at $\vec{\theta}_1, \vec{\theta}_2$ and $\kappa$ at $\vec{\theta}_3$,

$$\zeta_{\rm hh\kappa} \equiv \langle \delta_{\rm h}(\vec{\theta}_1)\, \delta_{\rm h}(\vec{\theta}_2)\, \kappa(\vec{\theta}_3) \rangle \,, \tag{4.11}$$

where the 2D halo overdensity $\delta_{\rm h}$ and convergence field $\kappa$ can be written in terms of the matter overdensity $\delta_{\rm m}$ as follows

$$\delta_{\rm h} = \int {\rm d}\chi\; p(\chi)\; \delta_{\rm h}^{(3D)}(\chi) = \int {\rm d}\chi\; p(\chi)\; b\, \delta_{\rm m}(\chi) \tag{4.12}$$

and

$$\kappa = \int {\rm d}\chi\, \Sigma_{\rm cr}^{-1}(\chi, \chi_{\rm s})\; \bar{\rho}_{\rm m,0}\, \delta_{\rm m}(\chi) \,, \tag{4.13}$$

with $\chi_s$ taken to be a fixed source plane. Here the halo bias $b \sim 2$ for the large host halos of LRGs, and $p(\chi)$ is the line-of-sight probability distribution of our LRG halos.

Under the flat-sky approximation, the projected correlation function $\zeta_{\rm hh\kappa}$ is given in terms of the 3D matter three-point correlation function as

$$\begin{aligned}\zeta_{\rm hh\kappa}(\theta_1,\theta_2,\theta_3) &= \int {\rm d}\chi_1 {\rm d}\chi_2 {\rm d}\chi_3\; p_1(\chi_1) p_2(\chi_2) \\ &\times \Sigma_{\rm cr}^{-1}(\chi_3,\chi_{\rm s}) \bar{\rho}_{\rm m,0} b^2 \langle \delta_{\rm m}(\chi_1\vec{\theta}_1)\; \delta_{\rm m}(\chi_2\vec{\theta}_2)\; \delta_{\rm m}(\chi_3\vec{\theta}_3)\rangle,\end{aligned} \tag{4.14}$$

with

$$\begin{aligned}&\langle \delta_{\rm m}(\chi_1\vec{\theta}_1)\; \delta_{\rm m}(\chi_2\vec{\theta}_2)\; \delta_{\rm m}(\chi_3\vec{\theta}_3)\rangle \\ &= \int \frac{{\rm d}^3\vec{k}_{\rm A}{\rm d}^3\vec{k}_{\rm B}{\rm d}^3\vec{k}_{\rm C}}{(2\pi)^3(2\pi)^3(2\pi)^3} B^{\rm PT}_{\rm mmm}(\vec{k}_{\rm A},\vec{k}_{\rm B},\vec{k}_{\rm C}) \\ &\quad \times (2\pi)^3 \delta^3_{\rm D}(\vec{k}_{\rm A}+\vec{k}_{\rm B}+\vec{k}_{\rm C})\, e^{i(\vec{k}_{\rm A}\cdot\vec{x}_1+\vec{k}_{\rm B}\cdot\vec{x}_2+\vec{k}_{\rm C}\cdot\vec{x}_3)},\end{aligned} \tag{4.15}$$

where $\vec{x}_i \equiv \chi_i\vec{\theta}_i$. We choose the line-of-sight LRG distributions to closely follow the measurement method. Since the measurement involves one LRG at essentially known line-of-sight comoving distance $\chi$, we set the first distribution $p_1$ to a delta function. The second LRG also has known redshift, which is fixed to be nearby the first LRG, but has some finite width due to the uncertainty of RSD. Thus we use the following distributions for the two LRGs:

$$p_1(\chi_1) = \delta_{\rm D}(\chi_1-\chi) \tag{4.16}$$

$$p_2(\chi_2) = \frac{1}{\sqrt{2\pi}\sigma} e^{-(\chi_1-\chi_2)/(2\sigma^2)}\,, \tag{4.17}$$

where $\sigma$ denotes the line-of-sight width of the distribution of the second LRG around the first.

Since we are interested in weak lensing due to filaments that arises from the matter distribution in the weakly nonlinear regime, we employ perturbation theory (3, 34) to compute

the matter bispectrum:

$$\begin{aligned}
B^{\rm PT}_{\rm mmm}(k_{\rm A},k_{\rm B},-k_{\rm AB}) &= P(k_{\rm AB})\times \\
&\left\{\left[\frac{10}{7}-\left(\frac{k_{\rm A}}{k_{\rm AB}}+\frac{k_{\rm B}\mu}{k_{\rm AB}}\right)\left(\frac{3}{7}\frac{k_{\rm A}}{k_{\rm AB}}+\frac{k_{\rm AB}}{k_{\rm A}}-\frac{4}{7}\frac{k_{\rm B}\mu}{k_{\rm AB}}\right)\right]P(k_{\rm A})\right. \\
&\left.+\left[\frac{10}{7}-\left(\frac{k_{\rm B}}{k_{\rm AB}}+\frac{k_{\rm A}\mu}{k_{\rm AB}}\right)\left(\frac{3}{7}\frac{k_{\rm B}}{k_{\rm AB}}+\frac{k_{\rm AB}}{k_{\rm B}}-\frac{4}{7}\frac{k_{\rm A}\mu}{k_{\rm AB}}\right)\right]P(k_{\rm B})\right\} \\
&\quad+\left[\frac{10}{7}+\mu\left(\frac{k_{\rm A}}{k_{\rm B}}+\frac{k_{\rm B}}{k_{\rm A}}\right)+\frac{4}{7}\mu^2\right]P(k_{\rm A})P(k_{\rm B})\,, \qquad (4.18)
\end{aligned}$$

where $\mu\equiv\cos\phi$ (see Fig. 4.6), $k_{\rm AB}=\sqrt{k_{\rm A}^2+k_{\rm B}^2+2k_{\rm A}k_{\rm B}\mu}$, and $P(k)$ is the linear matter power spectrum.

Employing Limber's approximation sets $\chi_3\approx\chi_2\approx\chi_1$, and the three-point function can be simplified as

$$\begin{aligned}
\zeta_{\rm hh\kappa} &= \int {\rm d}\chi_3\; p_1(\chi_3)\; p_2(\chi_3)\; \Sigma_{\rm cr}^{-1}(\chi_3,\chi_{\rm s})\; \bar{\rho}_{\rm m,0} b^2 \\
&\quad\times\int\frac{{\rm d}^2\vec{k}_{\rm A}{\rm d}^2\vec{k}_{\rm B}}{(2\pi)^2(2\pi)^2}B^{\rm PT}_{\rm mmm}(k_{\rm A},k_{\rm B},-k_{\rm AB}) \\
&\quad\times e^{i\chi_3[\vec{k}_{\rm A}\cdot(\vec{\theta}_1-\vec{\theta}_3)+\vec{k}_{\rm B}\cdot(\vec{\theta}_2-\vec{\theta}_3)]}\,, \qquad (4.19)
\end{aligned}$$

where $k_{\rm A}\equiv|\vec{k}_{\rm A}|$, and the vectors $\vec{k}_{\rm A},\vec{k}_{\rm B}$ are now two-dimensional, lying in the plane of the sky. The line-of-sight LRG distributions are now

$$p_1(\chi_3) = \delta_{\rm D}(\chi_3-\chi) \qquad (4.20)$$

$$p_2(\chi_3) = \frac{1}{\sqrt{2\pi}\sigma}e^{-(\chi_3-\chi_3)/(2\sigma^2)}=\frac{1}{\sqrt{2\pi}\sigma} \qquad (4.21)$$

The delta function $p_1(\chi_3)$ thus removes the last $\chi$ integral, leaving

$$\begin{aligned}
\zeta_{\rm hh\kappa} &= \frac{\Sigma_{\rm cr}^{-1}(\chi,\chi_{\rm s})}{\sqrt{2\pi}\sigma}\bar{\rho}_{\rm m,0}b^2\int\frac{{\rm d}^2\vec{k}_{\rm A}{\rm d}^2\vec{k}_{\rm B}}{(2\pi)^2(2\pi)^2} \\
&\quad\times B^{\rm PT}_{\rm mmm}(k_{\rm A},k_{\rm B},-k_{\rm AB})e^{i\chi[\vec{k}_{\rm A}\cdot(\vec{\theta}_1-\vec{\theta}_3)+\vec{k}_{\rm B}\cdot(\vec{\theta}_2-\vec{\theta}_3)]}\,, \qquad (4.22)
\end{aligned}$$

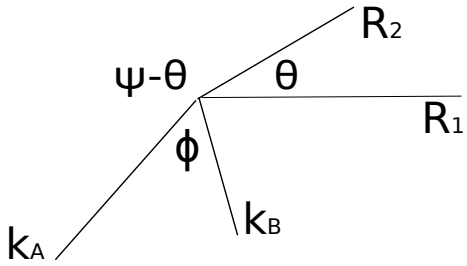


**Figure 4.6:** LRGs are located at $\vec{R}_1$ and $\vec{R}_2$, while the matter point of interest is at the origin. We integrate over the magnitude of the wavevectors, $k_{\rm A}$ and $k_{\rm B}$, the angle between them $\phi$, and the angle $\psi$ between $\vec{k}_{\rm A}$ and $\vec{R}_1$.

with again, $\vec{k}_{\rm AB} \equiv \vec{k}_{\rm A} + \vec{k}_{\rm B}$.

Choose the shear point to be at the origin, $\vec{\theta}_3 = 0$, and use comoving distances in the lens plane, $R_i = \chi\theta_i$, as in Fig. 4.6. Then the two $\mathrm{d}^2\vec{k}$ integrals can be written in terms of the magnitude of the wavevectors $k_{\rm A}$ and $k_{\rm B}$, the angle between them $\phi$, and the angle $\psi$ between $\vec{k}_{\rm A}$ and $\vec{R}_1$:

$$\int \mathrm{d}^2\vec{k}_a \mathrm{d}^2\vec{k}_b = \int_0^\infty \mathrm{d}k_{\rm A} k_{\rm A} \int_0^\infty \mathrm{d}k_{\rm B} k_{\rm B} \int_0^{2\pi} \mathrm{d}\phi \int_0^{2\pi} \mathrm{d}\psi \,.$$

In terms of these variables, the argument of the exponential is proportional to

$$\begin{aligned} \chi[\vec{k}_{\rm A}\cdot\vec{\theta}_1 + \vec{k}_{\rm B}\cdot\vec{\theta}_2] &= k_{\rm A}R_1\cos\psi + k_{\rm B}R_2\cos(\psi+\phi-\theta) \\ &= \alpha\cos\psi + \beta\sin\psi\,, \end{aligned} \tag{4.23}$$

where

$$\begin{aligned} \alpha &\equiv k_{\rm A}R_1 + k_{\rm B}R_2\cos(\phi-\theta)\,, \\ \beta &\equiv k_{\rm B}R_2\sin(\phi-\theta)\,. \end{aligned}$$

Then the three-point function can be rewritten as

$$\begin{aligned} \zeta_{\rm hh\kappa} &= \frac{\Sigma_{\rm cr}^{-1}(\chi,\chi_{\rm s})}{\sqrt{2\pi}\sigma}\bar{\rho}_{\rm m,0}b^2\frac{1}{(2\pi)^4}\int_0^\infty \mathrm{d}k_{\rm A}\int_0^\infty \mathrm{d}k_{\rm B}\int_0^{2\pi}\mathrm{d}\phi \\ &\quad \times k_{\rm A}k_{\rm B}\,B_{\rm mmm}^{\rm PT}(k_{\rm A},k_{\rm B},-k_{\rm AB})\,I_\psi(\alpha,\beta), \end{aligned} \tag{4.24}$$

where

$$I_\psi(\alpha,\beta) \equiv \int_0^{2\pi} \mathrm{d}\psi\, e^{i(\alpha\cos\psi+\beta\sin\psi)}\,.$$

It can be shown that this integral is a Bessel function of the first kind,

$$I_\psi = 2\pi \mathrm{J}_0(\sqrt{\alpha^2+\beta^2})\,,$$

so that

$$\begin{aligned}\zeta_{\mathrm{hh}\kappa} &= \frac{\Sigma_{\rm cr}^{-1}(\chi,\chi_s)}{\sqrt{2\pi}\sigma}\bar{\rho}_{\mathrm{m},0}b^2\frac{1}{(2\pi)^3}\int_0^\infty \mathrm{d}k_\mathrm{A}\int_0^\infty \mathrm{d}k_\mathrm{B}\int_0^{2\pi}\mathrm{d}\phi \\ &\quad \times k_\mathrm{A}k_\mathrm{B}\,B^{\rm PT}_{\mathrm{mmm}}(k_\mathrm{A},k_\mathrm{B},-k_\mathrm{AB})\,J_0(\sqrt{\alpha^2+\beta^2}),\end{aligned} \tag{4.25}$$

where $J_0(x)$ is the zero-th order Bessel function.

As can be seen from Eq. (4.25), the line-of-sight spread of the second LRG around the first, parametrized by $\sigma$, causes a dilution of the three-point correlation function; the wider spread reduces the amplitude due to the projection of different-direction structures. On the other hand, using a wider spread gives a larger sample of paired LRGs reducing the statistical noise. Hence the net signal-to-noise ratio is determined by a trade-off of these competing effects, as we will explicitly study below.

Although the LRGs of each pair are selected by the difference of their redshifts (see § 4.3.1), the line-of-sight spread $\sigma$ is statistically given by a sum of the redshift difference and the RSD effect:

$$\sigma = \sqrt{(\Delta r_{\rm los})^2+\sigma^2_{\rm RSD}} \tag{4.26}$$

where $\Delta r_{\rm los}$ is the rms separation inferred from the redshift difference of LRG pairs, $\Delta r_{\rm los} \simeq \Delta z/H(z_{\rm LRG})$, and $\sigma_{\rm RSD}$ is the width due to RSD. For our fiducial choice of LRG pair selection, we employ $\Delta r_{\rm los} \leq 6$ Mpc/$h$. However, the RSD is not a direct observable, and causes an uncertainty in the model prediction. The RSD has two contributions: bulk motions of halos in large-scale structure and virial motions of LRG within its host halo, where the latter is the so-called Finger-of-God (FoG) effect. The RSD due to halo bulk motions is

estimated as $\sigma \sim 4$ Mpc/$h$ from $N$-body simulations of the ΛCDM model (e.g., 95). For the virial motion contribution, recently (41) used the DR7 LRG catalog to measure the g-g weak lensing and clustering measurements in order to study the FoG. For *multiple LRG systems*, which are massive halos (with $\sim 10^{14} M_{\odot}/h$ and $b \sim 3$) hosting multiple LRGs inside, the FoG effect is estimated as $\sigma \sim 9$ Mpc/$h$ for LRGs at $z \simeq 0.35$. For other LRGs residing in less massive host halos, the virial motions are smaller.

Summing up these effects, the line-of-sight spread of LRGs in the pairs can be as large as $\sigma \sim 10$ Mpc/$h$. However, since the majority (above 90%) of the LRGs are only single-LRG systems, for which $\sigma_{\rm RSD} \sim 6$, our best estimate is $\sigma \sim 8$ Mpc/$h$. However, for any reasonable estimate of the RSD effect, the amplitude of the theory prediction is significantly larger than our measurement from the data. With the choice of $\sigma = 8$ Mpc/$h$, the magnitude of the offset is a factor of 10 (see § 4.5). This requires further investigation with simulated lensing maps on which the measurement procedure is applied. In all plots involving the halo model prediction, we scale the amplitude to match the data.

In Fig. 4.7, we show the perturbation theory prediction for the kappa maps around hypothetical halo pairs hosting LRGs, for various choices of $R_{\rm pair}$. In these figures, we employ $b = 2$ for linear bias of LRGs, and $z_{\rm L} = 0.25$ and $z_{\rm s} = 0.4$ for LRG redshift and source redshift, respectively. As described above, the amplitude is scaled to match the data.

#### 4.4.1.2 Shear Map

To compare the two, we bin the prediction in the same way as the data. We begin by transforming the predicted kappa maps into shear maps. Due to symmetry, the resulting map of the cross-component $\gamma_2$, when binned in the same way as our data, gives identically zero signal. This provides one of our null tests. However, in order to visualize the shear map resulting from the three-point function, we go ahead and calculate the shear map for both $\gamma_1$ and $\gamma_2$.

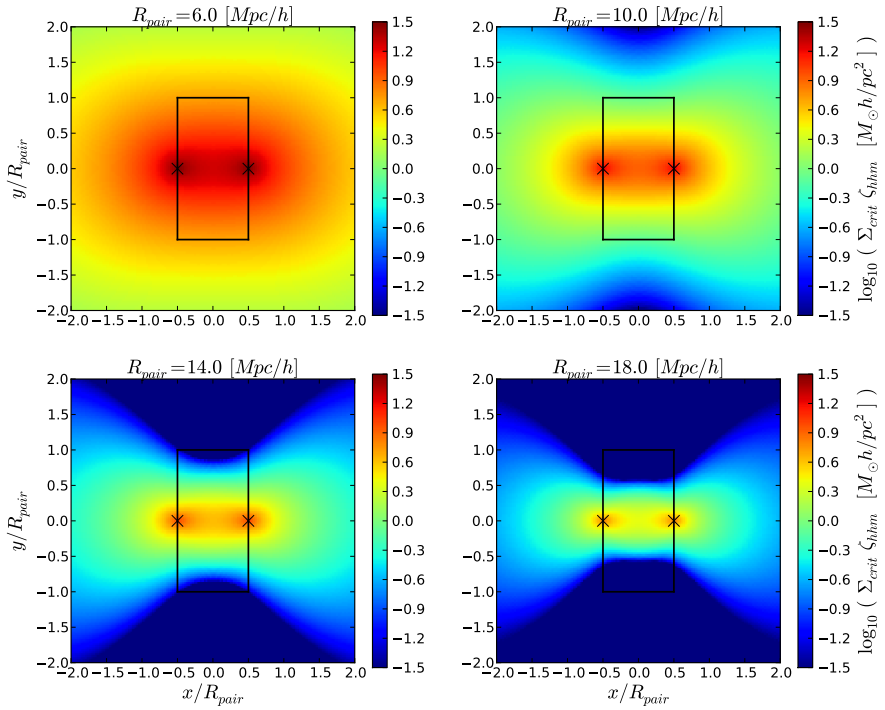


**Figure 4.7:** Here we plot the halo model prediction for the surface mass density contributed by the three point function in the neighborhood of LRG pairs (positions marked by "×"). The amplitude is a strong function of $R_{\rm pair}$, with the peak density dropping by about an order of magnitude from $R_{\rm pair} = 6$ Mpc/$h$ to $R_{\rm pair} = 18$ Mpc/$h$. However, the shape is roughly the same for all pair separations. Note that spatial scales are plotted in units of $R_{\rm pair}$. The amplitudes of this and all other theory plots are scaled to match the data. Note that, for this plot, we did not include the mass contribution from LRG halos, so the mass distribution is purely from the perturbation theory of the halo-halo-matter correlation function.

The shear and convergence fields are related in Fourier space by

$$\tilde{\gamma}_1(\vec{l}) = \tilde{\kappa}(\vec{l})\cos 2\phi_{\vec{l}} \quad (4.27)$$

$$\tilde{\gamma}_2(\vec{l}) = \tilde{\kappa}(\vec{l})\sin 2\phi_{\vec{l}}, \quad (4.28)$$

where $\phi_{\vec{l}}$ is the angle between the wavevector $\vec{l}$ and the $x$-axis of the coordinate system. We zero-pad the $\zeta_{\mathrm{hh}\kappa}$ map out to a spatial scale 5 times larger than the map itself. This ensures that there is no spurious shear due to the periodic boundaries assumed in an FFT. After zero padding, we perform the FFT, then apply Eqs. (4.27, 4.28), and finally carry out the inverse FFT.

Note that for close pairs, such as in the top left panel of Fig. 4.7, the surface density is still significant at the edge of the pictured region. If such a map is zero-padded and the above process is applied to obtain $\gamma$ maps, they will contain spurious shear due to the steep fall in density at the beginning of the zero-pad region. We find that the FFT converges for $R_{\mathrm{pair}} \geq 6$ Mpc/$h$ as long as the $\zeta_{\mathrm{hh}\kappa}$ map is calculated out to $\pm 16\, R_{\mathrm{pair}}$ from the center of the line joining the pair of halos. We also check convergence of the FFT as a function of resolution, and find that spacing between grid points of $0.1\, R_{\mathrm{pair}}$ is sufficient.

An example of the resulting whisker plot is shown in Fig. 4.8, for $R_{\mathrm{pair}} = 10$ Mpc/$h$. The largest magnitude shears of $\gamma_1 \sim -0.001$ lie between the two peaks of the three-point function. At radial distances beyond $0.5\, R_{\mathrm{pair}}$ from the line connecting two halos, the shear direction is parallel to the line ($\gamma_1 > 0$ for our definition as given in Fig. 4.1), as expected in the thin filament. Moving closer to the midpoint of the halos, the shear vanishes at about $0.5\, R_{\mathrm{pair}}$, and the direction then becomes flipped, now perpendicular to the connecting line ($\gamma_1 < 0$), which looks like "tangential shear" with respect to each halo. However, the width of the perpendicular shear region is about $0.5\, R_{\mathrm{pair}} \sim 5$ Mpc/$h$, wider than the virial radius of the halos. Hence we call this model the "thick-filament" model. These features are from the perturbation theory matter bispectrum, thus reflecting the nature of large-scale structure in the weakly nonlinear regime. The shear pattern is qualitatively the same for

other $R_{\rm pair}$ values, being well described by a decreasing amplitude for larger $R_{\rm pair}$. The green box outlines the Signal region of Fig. 4.2.

#### 4.4.1.3 Averaging over $R_{\rm pair}$, $z_{\rm L}$ and $z_{\rm s}$ distributions

The PT 3pt function has a trivial redshift dependence according to the linear growth rate, $\propto D^4_{\rm lin}(z_{\rm L})$. Therefore we only have to do the time-consuming $k_{\rm A}, k_{\rm B}$ and $\phi$ integrals in Eq. (4.25) once for some arbitrary redshift values (here $z_{\rm L} = 0.25, z_{\rm s} = 0.40$).

The measurement is of $\Delta\Sigma_1^{\rm fil}$ and to this point we are still working with the dimensionless $\zeta_{\rm hh\kappa}$. We should rather compare the data with $\zeta_{\rm hh\kappa}\Sigma_{\rm crit,eff}$; therefore we next obtain the effective lensing strength from the data. It is simply

$$\Sigma_{\rm crit,eff} = \int {\rm d}z_{\rm L}\, p(z_{\rm L}) \int {\rm d}z_{\rm s}\, p(z_{\rm s})\, \Sigma_{\rm crit}(z_{\rm L}, z_{\rm s})\,, \tag{4.29}$$

a redshift weighting over the lens and source redshift distributions shown in Fig. 4.4.

The $R_{\rm pair}$ distribution within a given bin is essentially flat (see Fig. 4.4). The combination of different $R_{\rm pair}$ predictions is therefore easily modeled by a geometric factor accounting for the relative number of source galaxies which enter the measurement for each pair separation. This difference in area sampled by each pair goes as $R^2_{\rm pair}$, so the prediction for a given bin is

$$\langle \zeta_{\rm hh\kappa}\Sigma_{\rm crit}\rangle_{R_{\rm pair}} = \frac{\int_{R_{\rm min}}^{R_{\rm max}} {\rm d}R_{\rm pair} R^2_{\rm pair}\zeta_{\rm hh\kappa}\Sigma_{\rm crit}}{\int_{R_{\rm min}}^{R_{\rm max}} {\rm d}R_{\rm pair} R^2_{\rm pair}}\,. \tag{4.30}$$

We apply this weighting when comparing data and theory in § 4.5.

The last step in obtaining predictions for our binning scheme (Fig. 4.2) involves generating random points within the pictured area to imitate source galaxies. Then we interpolate over the $\gamma_1$ grid as pictured in Fig. 4.8 to obtain the shear for each random point. Finally, the shears are binned together in the same way as the data.

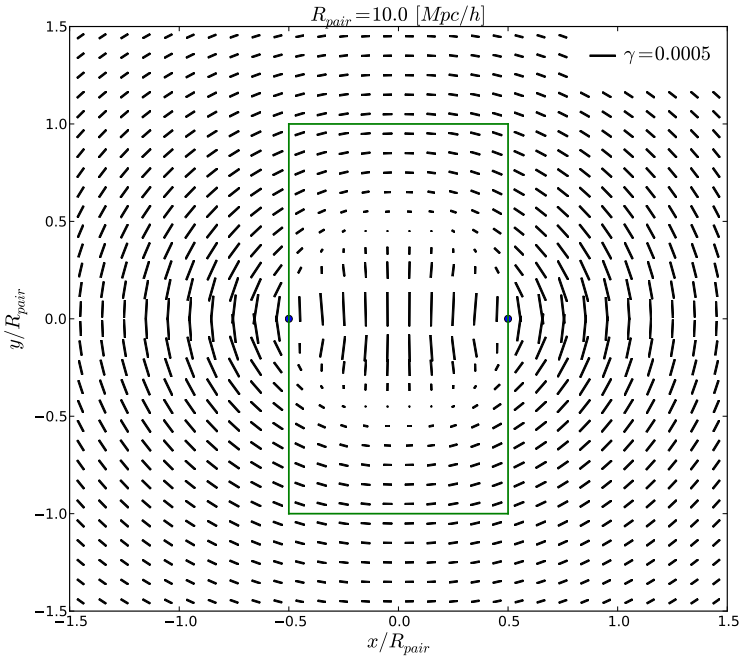


**Figure 4.8:** An example of the halo model shear map prediction for LRGs separated by $R_{\rm pair} = 10$ Mpc/$h$. Starting at the filament midpoint and moving on a line perpendicular to the filament, we see $\gamma_1$ transition from a large negative amplitude, to a smaller positive amplitude after passing through zero at $\sim 0.5\, R_{\rm pair}$. The shear maps of other $R_{\rm pair}$ values are qualitatively similar. The green rectangle shows the Signal region of Fig. 4.2. Two rows of the innermost whiskers have been removed for clarity. Note that the amplitude of the whiskers is scaled to match the data. After this scaling, the shear values are of order 0.1%, with scale shown in the upper right corner.

### 4.4.2 Thin-filament model

Here we consider a "string of halos" as an independent model from the halo model. For this simple model, we use a 1D line of NFW halos as in Maturi & Merten (83). The shear induced by an NFW profile has an exact solution given by Wright & Brainerd (139):

$$\Delta\Sigma_{\rm NFW} = r_s\,\delta_c\,\rho_c\,g(x) \tag{4.31}$$

where $g(x)$ is given by

$$g(x) = \begin{cases} g_< & \text{for} \quad x<1 \\ (10/3)+4\ln(1/2) & \text{for} \quad x=1 \\ g_> & \text{for} \quad x>1 \end{cases}, \tag{4.32}$$

with

$$\begin{aligned} g_<(x) &= \frac{8\,\mathrm{arctanh}\sqrt{(1-x)/(1+x)}}{x^2\sqrt{1-x^2}} + \frac{4}{x^2}\ln(x/2) \\ &\quad -\frac{2}{x^2-1} + \frac{4\,\mathrm{arctanh}\sqrt{(1-x)/(1+x)}}{(x^2-1)\sqrt{(1-x^2)}} \end{aligned} \tag{4.33}$$

$$\begin{aligned} g_>(x) &= \frac{8\arctan\sqrt{(x-1)/(1+x)}}{x^2\sqrt{x^2-1}} + \frac{4}{x^2}\ln(x/2) \\ &\quad -\frac{2}{x^2-1} + \frac{4\arctan\sqrt{(x-1)/(1+x)}}{(x^2-1)^{3/2}}\,. \end{aligned} \tag{4.34}$$

The model has just two parameters: $M_{\rm fil}$, the total mass in the string of halos, and $N_{\rm fil}$, the number of halos in the string. Each halo is given a mass $M_{\rm halo} = M_{\rm fil}/N_{\rm fil}$, and different halos are equally-spaced along the string between two LRGs. We use $M_{\rm fil} = 2\times10^{14}M_\odot/h$ and $N_{\rm fil} = 20$, so that the mass per halo is $10^{13}M_\odot/h$. However, we have checked that the prediction is not very sensitive to the choice of $N_{\rm fil}$. To generate predictions for this model, we calculate the shear profile at any given point by adding up the contribution for each halo in the string, with each halo's contribution calculated according to Eq. (4.31). The overall

shear amplitude depends on the total mass $M_{\rm fil}$. This model generally predicts the shear pattern that is parallel to the string (i.e. $\gamma_1 > 0$), at the distance $R \gtrsim 1$ Mpc/$h$. Hence we call this the "thin-filament" model.

## 4.5 Results

We have detected at $10\sigma$ a stacked filament lensing signal by comparing the measurement to the null hypothesis that there is no excess mass extending between the LRGs. Under that hypothesis, we expect a lensing signal consistent with zero. The null has an expected chi-square of

$$\langle \chi^2 \rangle = N - n \pm \sqrt{2N + 2n} = 18 \pm 6 \tag{4.35}$$

where $N = 18$ is the number of bins and $n = 0$ the number of model parameters. To validate our detection, we first show four separate null tests which are consistent with the null hypothesis, before moving on to show the measurement itself and comparison to theory.

For all null tests, we repeat the measurement of our Eq. (4.8) estimator for $\Delta\Sigma_1^{\rm fil}$ using the same jackknife regions. The difference is that rather than using close LRG pairs to define the measurement regions of Fig. 4.2, we choose the "pair center," $R_{\rm pair}$, and angle of the Cartesian coordinate system on the sky $\phi$ in such a way that the result should be consistent with the null hypothesis of no excess mass lying along the center of the Fig. 4.2 Signal region. The summary of all chi-square results for our null tests and the measurement itself is shown in Table 4.1.

### 4.5.1 Null tests: Unpaired LRG, Separated pairs, and Cross-component

Our first three null tests pass straightforwardly. First, the unpaired LRG test involves removing one LRG of the pair. In other words, we use the entire catalog of LRGs, assign each one a random $R_{\rm pair}$ and orientation angle, then calculate $\Delta\Sigma_1^{\rm fil}$ as if it has a partner LRG at that $R_{\rm pair}$ and angle. While we expect many LRGs to have filaments, the random

| Null hypothesis | $\langle\chi^2\rangle = 18 \pm 6$ | |
|---|---|---|
| | $\chi^2$ | significance |
| Separated pair test | 19.5 | 0.2 $\sigma$ |
| Unpaired LRG test | 19.8 | 0.3 $\sigma$ |
| Cross-component | 16.3 | 0.3 $\sigma$ |
| Random points (larger errors) | 37.3 (23.6) | 3.2 (0.9) $\sigma$ |
| LRG pair (larger errors) | 89.7 (78.0) | 12.0 (10.0) $\sigma$ |

**Table 4.1:** Summary of the chi-square results for the filament lensing measurement. In parentheses we show the $\chi^2$ and significance results after accounting for systematic errors. All null tests are passed, and the measurement shows a $10\sigma$ deviation from the null hypothesis.

orientations used in this test should stack individual filaments such that the final mass distribution is isotropic, and thus nulled by our procedure. The result is shown in Fig. 4.9 (red triangles), and with a $\chi^2 = 19.8$ is consistent with zero. The detection significance of $0.3\sigma$ shown in Table 4.1 is calculated as

$$\text{significance} = \frac{\chi^2 - \langle\chi^2\rangle_{\rm null}}{\sigma_{\rm null}} = \frac{19.8 - 18}{6} = 0.3\sigma\,, \tag{4.36}$$

and is well under $1\sigma$.

The separated pair test involves using two LRGs at the "h1" and "h2" positions of Fig. 4.1, but with line-of-sight separation 100 Mpc/$h$ $< \Delta r_{\rm los} <$ 120 Mpc/$h$. The 3D distance of such pairs is so large that we expect no excess mass to build up between them. For the lens redshift $z_{\rm L}$, we use the average of the two LRG redshifts. The result is shown in Fig. 4.9 (green diamonds) and is consistent with zero, with $\chi^2 = 19.5$ and significance $0.2\sigma$. Furthermore, this test shows that the spherically symmetric shear signal from both LRGs in the measurement is truly nulled, as claimed.

As in tangential shear measurements, where the cross-component of shear rotated by 45° has no first-order contribution from gravitational lensing, our cross-component (the $\Delta\Sigma_2^{\rm fil}$

component of Eq. 4.8) has no contribution from a filament. This statement holds as long as the stacked mass distribution around the LRG pairs has reflection symmetry about the line joining the pairs. For such a mass distribution, in the Cartesian coordinate system of Fig. 4.1, $\gamma_2(y) = -\gamma_2(-y)$. Since background sources at $y$ are always put in the same bin with sources at $-y$, (see Fig. 4.2), $\Delta\Sigma_2^{\rm fil} = 0$ on average. This is what we find in Fig. 4.10, where the magenta triangles show the result of this null test. The $\chi^2 = 16.3$ for a significance of $0.3\sigma$, consistent with the null hypothesis.

### 4.5.2 Null test: Random points

Finally, for the random points test, we repeat the measurement on $\sim 10$ times as many random points with the same distribution in $\phi$, $z$, and $R_{\rm pair}$ as the pair catalog. The result shown in Fig. 4.9 (blue circles) has a small magnitude $\sim 0.1\,M_\odot h/{\rm pc}^2$, but with a $\chi^2 = 37.3$ it is $3.2\sigma$ inconsistent with zero. We assume that this inconsistency is the result of some unknown systematic error(s) in the measurement. We account for this systematic error by adding to each error bar a constant $\sigma_{\rm syst} = 0.039\,M_\odot h/{\rm pc}^2$; this is smaller than the jackknife error on any individual bin of the random points measurement, and corresponds on average to an increase of 36% on each error bar. (In other words, we assume that this systematic acts only on the diagonal of the covariance matrix, and so we add $\sigma^2_{\rm syst}$ to each diagonal element of the covariance matrix.) The total error on any given bin $i$ becomes $\sqrt{\sigma^2_{i,{\rm JK}} + \sigma^2_{i,{\rm syst}}}$, yielding a $\chi^2 = 23.6$ for the random points test, within $1\sigma$ of the null hypothesis.

### 4.5.3 Measurement

Now we turn to the filament measurement itself, using LRG pairs which are likely to have excess mass in between. Our initial measurement with covariance directly from the jackknife realizations yields a $\chi^2 = 89.7$ and corresponding significance $12.0\sigma$. However, we need to take account of the fact that the random points measurement was inconsistent with zero until the errors were increased to account for unknown systematics. Thus, we add in quadrature

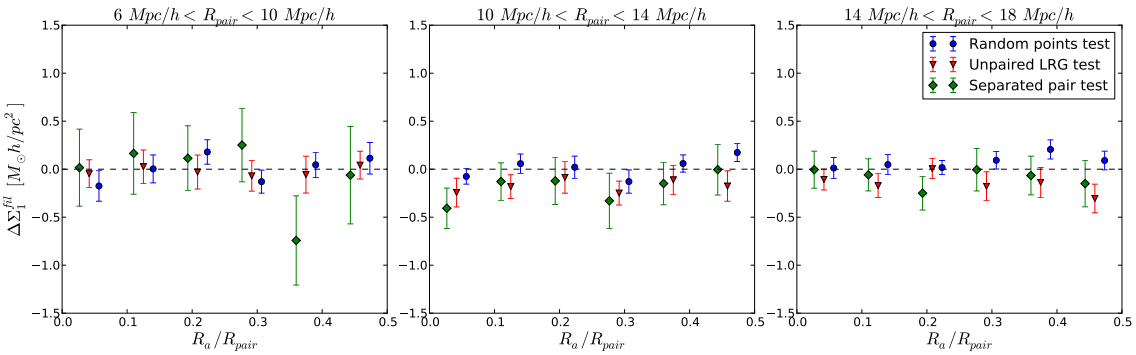


**Figure 4.9:** The results of three null tests (labelled in the legend) for our closest set of pairs *(left panel)* and more widely separated pairs *(middle and right panels)*. The unpaired LRG test and separated pair test are both consistent with the null hypothesis, showing that our estimator does null the spherically symmetric signal from the LRG halos.

the same constant $\sigma_{\rm syst} = 0.039\,M_\odot h/{\rm pc}^2$ to the measurement error bars. This addition made the random points test consistent with zero, but since the magnitude of the error bars on the measurement itself is much larger, this constant diagonal error only increases the uncertainty on each data point by $< 2\%$. The resulting $\chi^2$ is then 78.0, decreasing the detection significance to $10.0\sigma$, still a robust detection of filament lensing. The black circles of Fig. 4.10 show the measurement with these larger error bars.

Note that in addition to the measurement of Fig. 4.10 using the estimator of Eq. (4.8), we have repeated the measurement using only Eq. (4.6). Some signal is still present in this case without the systematic region subtraction, but the significance of the detection is somewhat less without this subtraction.

In Fig. 4.11 we show the normalized covariance matrix of $\Delta\Sigma_1^{\rm fil}$, $r_{ij} \equiv C_{ij}/\sqrt{C_{ii}C_{jj}}$. Most off-diagonal elements are near zero, with a scattered few of magnitude $r_{ij} \sim 0.5$. The highest covariance with $r_{ij} > 0.5$ is found in the top right corner of the matrix, corresponding to pairs with 14 Mpc/$h$ $< R_{\rm pair} <$ 18 Mpc/$h$. For comparison, we also show the cross-component $\Delta\Sigma_2^{\rm fil}$ covariance.

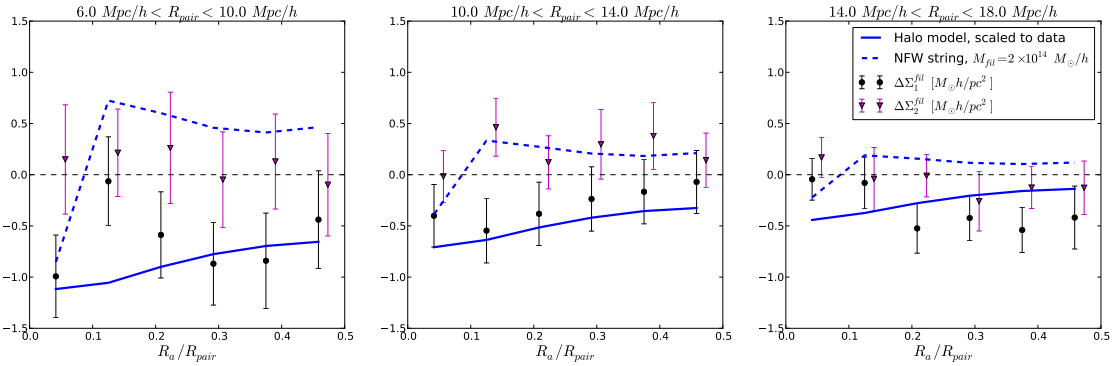


**Figure 4.10:** Same as Fig. 4.9, but showing the cross-component null test $\Delta\Sigma_2^{\rm fil}$ (purple points) and measurement $\Delta\Sigma_1^{\rm fil}$ (black points). The cross-component is consistent with zero, while the measurement deviates by $10\sigma$. We compare the measurement to two theoretical models, the halo model (solid blue line) and NFW string (dashed blue), both of which have an amplitude adjusted to match the measurement. The shape of the halo model prediction is supported by the data, while the NFW string is clearly ruled out.

### 4.5.4 Comparison to theory

In Fig. 4.10 we compare the halo-model and thin-filament models to the data. With a sign-flip relative to the data, the thin-filament model (blue dashed line) is difficult to support, but the thicker filament predicted by a halo model calculation (blue solid line) is more accurate. For the halo model, our best estimate of the contribution from redshift space distortions (with a dispersion of $\sigma_{\rm RSD} = 5$ Mpc/$h$) is $\sigma = 8$ Mpc/$h$. Even with this dilution of the signal, we need to scale the halo model amplitude down by a factor of ten to match the data. Thus, the combination of bias in the measurement, dilution of the signal, and error in the halo model prediction leads to a large offset between theory and measurement. As for the NFW string prediction, the magnitude is controlled by the total filament mass, $M_{\rm fil}$. For this plot, it was adjusted to $M_{\rm fil} = 2 \times 10^{14} M_\odot/h$, giving a magnitude roughly equal to the halo model prediction. (Although clearly the shape is still wrong.)

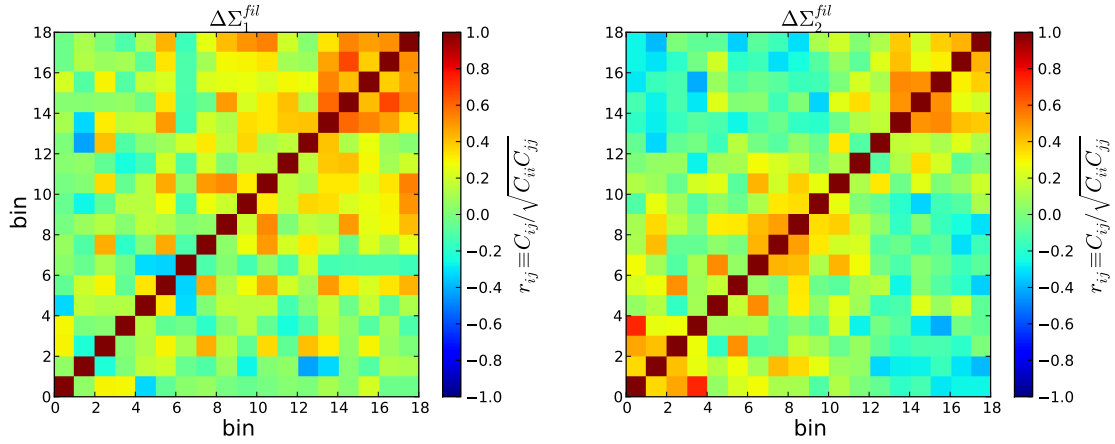


**Figure 4.11:** (*left panel*): The normalized covariance matrix of $\Delta\Sigma_1^{\rm fil}$. The pairs separated by the largest distance of 14 Mpc/$h$ $< R_{\rm pair} <$ 18 Mpc/$h$ (top right corner of $r_{i,j}$) show the strongest correlations between bins. (*right panel*): The same, but for $\Delta\Sigma_2^{\rm fil}$. We use the full covariance matrices when calculating the significance of the deviation from the null hypothesis for the measurement and each null test.

We calculate the average mass and density in the region between the halos using the halo model mass maps of Fig. 4.7. However, note that these results should be taken with caution, as again the amplitude has been scaled to match the measurement. The result is shown as a function of $R_{\rm pair}$ in Fig. 4.12. The different curves show the results for different choices of $y_{\rm max}$, the maximum distance which we include in the average. The averaging along the x-axis includes all mass which is both between the two halos, and at least 1 Mpc/$h$ from either halo center. In other words, we do not count mass that would be within either halos' virial radius in the estimate of the filament mass.

## 4.6 Discussion

We have presented a technique for the statistical measurement of properties of dark matter filaments between LRG halos separated by $\sim$ 10Mpc. We use an empirical approach to cancel out the contribution of spherical halos and constant shear patterns in the data. The residual shear patterns are attributed to filamentary structures and the mass and thickness of the filament are estimated. We find the data prefer thick filaments that contain at least twice as much mass as the halos that set at their end points.

There are several approximations and sources of error in our analysis.

- The stacking of hundreds of thousands of LRG pairs leads to a smearing of the mass distribution. This means that we cannot make definitive statements about the typical filament structures in the universe, in particular the limits we obtain on the thickness of the filament only apply to the stacked profile.

- The binning scheme we use to null out the contribution of spherical halos and other considerations mixes scales. It also preserves the signal only from perfect cylindrical symmetry. So even genuine structures beyond spherical mass distributions are nulled out.

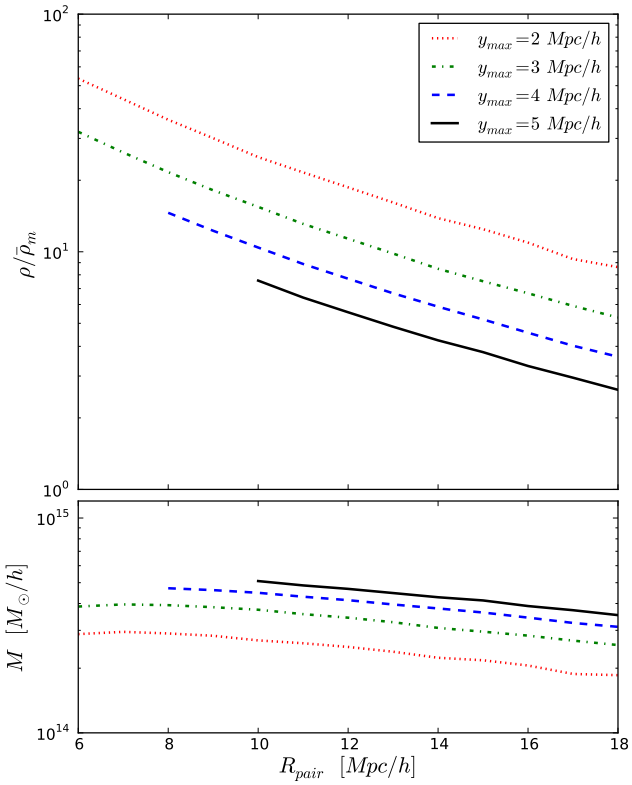


**Figure 4.12:** Estimates of the mass density (*upper panel*) and the enclosed mass (*lower*) in the filament, using the best-fit halo model predictions to the measurements in Fig. 4.10. To estimate these quantities, we integrate the projected mass density over the rectangular area that is defined by the separation distance of paired LRGs outside their virial radii ($x$-axis) and the distance from the line connecting the two LRGs ($y_{\rm max}$ denoted by the legend). The estimated volume in the top panel is taken to be a cylinder of radius $y_{\rm max}$, with four choices indicated in the legend. With density contrasts $\rho/\bar{\rho}_m \sim 10$, the component of matter we measure falls between the regimes of high density halos and the low density linear regime.

- Errors in shear estimates from the intrinsic ellipticities of background galaxies dominate the statistical error in our measurement. The other major source of statistical error is the variations in the mass distribution between different LRG pairs – this cannot be quantified from the data, so we intend to study it with simulations.

- The calibration of the shear, which relies on a correction for the smearing due to the PSF, introduces a redshift dependent bias that propagates to the filament mass estimate. Uncertainties in the photometric redshifts of background galaxies have a similar effect.

- Redshift space distortions: the line of sight separation of the LRG's is uncertain owing to their relative peculiar velocity. We have attempted to account for it in our discussion above.

- The inevitable contamination of the LRG sample with other galaxies and stars leads to a dilution of the signal. This should be controlled to better than the 10% level.

- Finally, the theoretical model is based on halo-halo-mass correlations in the halo model. This model is known to have limitations, with the amplitude being consistent with N-body simulations only at the 30% level. In particular, the halo model tends to overestimate the clustering amplitude over a range of 1-10Mpc, the transition regime between the weakly and strongly nonlinear regimes. The regime also involves theoretical approximations such as the linear halo bias assumption.

In future work several improvements can be made that address nearly all the above points. In addition forward modeling of the measurement can be done using simulations and the halo model, so that comparisons can be made without use of our nulling technique. Such an approach may allow for more detailed tests of the halo model and of filamentary properties, though care will need to be exercised to distinguish systematic errors. Finally, an

obvious complement to our study is to compare the mass distribution inferred from lensing shears with the distribution of foreground galaxies and hot gas.

# Chapter 5

# Lensing Measurements of the Mass Distribution in SDSS Voids

## 5.1 Introduction

The first measurement of lensing from stacked galaxies was observed almost twenty years ago by Brainerd et al. (6). Since then, applications of this technique to the Sloan Digital Sky Survey (SDSS) have made stacked galaxy lensing an indispensable measure of galaxy halo masses, e.g., Mandelbaum et al. (77) and Sheldon et al. (117). More recently, in Clampitt et al. (17), we measured the stacked lensing signal of filaments connecting neighboring Luminous Red Galaxies (LRGs). In that work, we made a significant detection of a filament lensing signal, and thus were able to study the thickness and mass density of filaments. With the goal of obtaining a the analogous measurement for voids, we construct a void catalog from holes in the LRG distribution of SDSS, measure the void tangential shear profile, and constrain their density profiles.

There are many void finders in the literature, all differing in implementation and the resulting set of voids found. Colberg et al. (19) makes a comparison of 13 algorithms. In recent years, methods involving a Voronoi tessellation coupled with a watershed transform

have become popular (68, 93, 108). These methods have also been successfully applied to data, yielding void catalogs from surveys such as SDSS (125). A lensing analysis of the Sutter et al. (125) catalog was carried out by Melchior et al. (85). However, despite careful attention to details of the shear measurement, the small number of voids in the catalog was likely a factor in the marginal detection significance.

Recent work has studied in more detail the properties of dark matter voids in simulations. Hamaus et al. (37) found that previous fits to simulation density profiles were too simple and provide fitting formulae with parameters that can be adapted to voids with a range of sizes. Sutter et al. (127) and Sutter et al. (128) have worked to connect the theory of voids found in the dark matter to those found in galaxies by using Halo Occupation Distribution models to mimic realistic surveys. Excursion set work has focused on providing semi-analytical models of void abundances (103, 121), as well as connecting these models to void counts from simulations (61).

Once void catalogs are constructed, they have numerous other applications. Hoyle et al. (49) used a different void finder (47, 101) to study the photometric properties of void galaxies. They find that void galaxies are bluer than those in higher density environments, but do not vary much within the void itself. Cosmological probes such as the Alcock-Paczynski test (68, 126) and void-galaxy correlations (36) have been proposed. Finally, voids also provide a sensitive test of some modified gravity theories (16, 74).

Section 2 describes our basic void-finding algorithm, as well as our cuts to select a subsample useful for lensing. Section 3 explains our weak lensing measurement, null tests, and expected signal-to-noise. Section 4 presents our results on void density profiles, including both a fitted model and model-independent statements. Finally, Section 5 summarizes our results, caveats, and directions for future work.

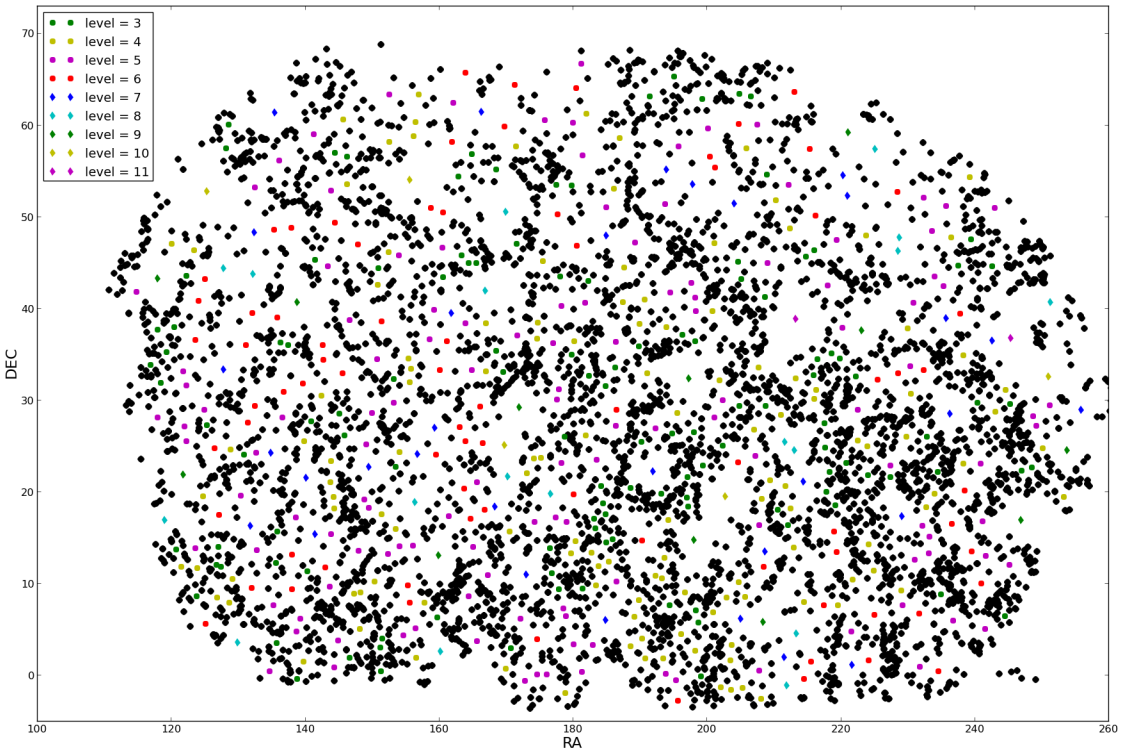


**Figure 5.1:** Slice thickness of 50 Mpc/$h$, corresponding to voids with line of sight size radius $s_{\rm v} = 25$ Mpc/$h$. The black points show pixels containing LRGs in this slice. This is an intermediate redshift ($z \sim 0.25$) slice with intermediate volume and 2D LRG density. The colored circles and diamonds show the output of our void finder for various iteration levels, as marked in the legend. Note that not all objects found at this stage remain in the final catalog.

## 5.2 Void finding

For lensing purposes, the two numbers output by a void finder that matter most are the void center location and radius on the sky. The center is needed for the stacked tangential shear measurement, and the radius so that the background sources for each void in the stack can be placed in the appropriate bin relative to that void's edge.

### 5.2.1 Algorithm

#### 5.2.1.1 Redshift slices

We use the SDSS DR7-Full LRG catalog of Kazin et al. (62), which contains $\sim 66,500$ LRGs between $0.16 < z < 0.37$, a roughly volume limited part of the sample. The sky coverage is approximately 7,500 sq. deg. The problem with using the deeper magnitude-limited sample is that too many false voids will be found, i.e., voids which are due to gaps in LRG coverage rather than real density minima. These false voids would dilute the lensing signal when stacked.

We begin by cutting the volume probed by LRGs into slices of comoving thickness $2s_{\rm v}$ in the line-of-sight direction. For a slice centered at $r_{\rm los}$, we assign (i) $r_{\rm los}$ as the center for all candidate voids found within that slice, and (ii) $s_{\rm v}$ as the radius in the line-of-sight direction. That these values are reasonable estimates for the void location and size will be verified later (Fig. 5.4). We use values of $s_{\rm v}$ between 10 Mpc/$h$ and 50 Mpc/$h$; as described in § 5.2.2.4, for any void found in multiple slices we use the largest slice size to assign $s_{\rm v}$. We show an example of the LRG distribution within a slice in Fig. 5.1 at $z \sim 0.25$ and with thickness $2s_{\rm v} = 50$ Mpc/$h$. The black points show all LRGs in the slice.

#### 5.2.1.2 2D hole-finding algorithm

The next step is to select the holes in that slice. Our algorithm is as follows:

1. Pixelize the redshift slice using a fine HEALpix grid with nside=256.

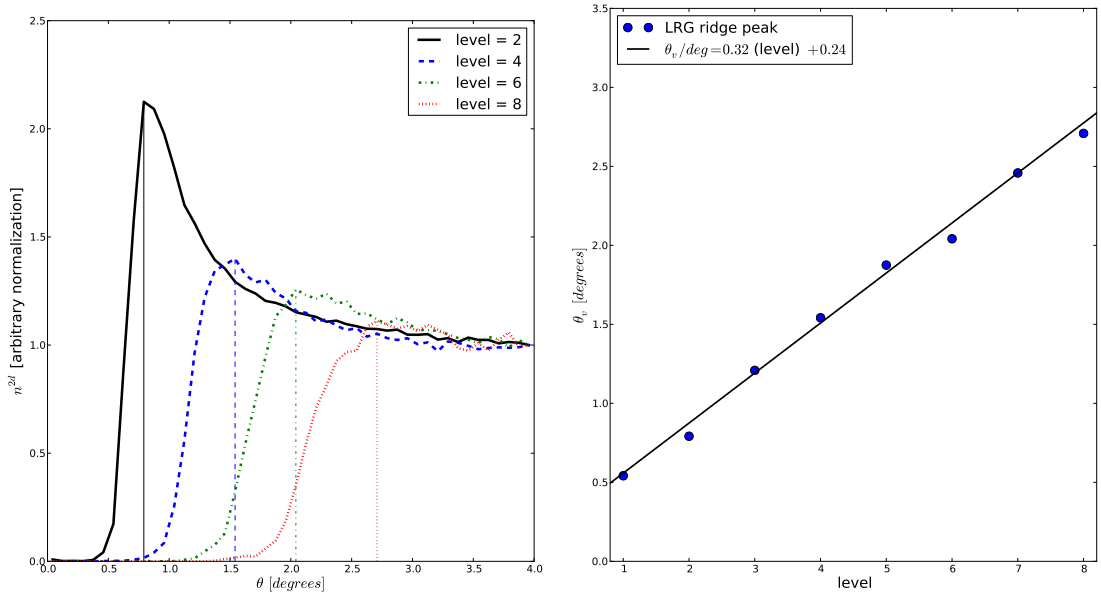


**Figure 5.2:** (*left panels*): The 2D LRG density within the void slices, stacked over all candidate voids found at the given iteration level of the algorithm. The void candidates with smallest transverse size show a prominent ridge: we take the angular scale of the ridge maximum as the void radius $\theta_{\rm v}$. (*right panel*): The blue points show the LRG ridge locations identified in the left panels as a function of iteration level. This relationship is clearly linear, allowing us to extrapolate the solid line beyond level = 8 where the LRG ridge vanishes.

2. Define the set of pixels containing LRGs as $L_1$. To define $L_i$ for $i > 1$, take the set of pixels which touch at least one of the $L_{i-1}$ pixels on a side or corner (each pixel has 8 possible neighbors) and add this set of neighbors to $L_{i-1}$ to obtain $L_i$.

3. Call the set of pixels in the survey area $U$. Define the set of empty pixels as the set difference $P_1 = U - L_1$.

4. Divide $P_1$ into N sets of disconnected pixels, $P_{1,j}$ where $j \in \{1, ..., N\}$. Two sets of pixels are disconnected from each other if they share no pixels and no neighboring pixels.

5. Define $N_{\rm th}$ as the threshold number of pixels required for a void candidate. Any of the $P_{1,j}$ with $N_{\rm th}$ or fewer pixels are removed from $P_1$ and a void candidate with RA, DEC given by the average RA, DEC of those pixels is recorded. Define $P_1'$ as the set of pixels which are part of any disconnected set with $N_{\rm th}+1$ or greater pixels. We use $N_{\rm th} = 23$, but the results are not very sensitive to this number: if any set of pixels go from above the threshold to vanishing between iteration levels, we also count those as a void candidate.

6. Now define $P_2 = P_1' - L_2$. To recap, $P_2$ contains all pixels which are are at least 2 pixels away from an LRG, and were not already counted as part of a void candidate in step (v).

7. Steps (iv) - (vi) are repeated using $P_2$, finding more void candidates and giving $P_3$. This process continues until no more pixels remain in $P_{i'}$ for some $i'$.

The centers of the resulting void candidates for one slice are plotted as the colored points in Fig. 5.1. For each void candidate, we keep track of the iteration level at which it was identified, i.e., if found in set $P_i$ that object has an iteration level of $i$. Different colors and symbols indicate different iteration levels. For example, the green circles were all identified

during the third iteration level. The two purple diamonds in Fig. 5.1 were identified much later, at level 11. The number of objects found at various iterations of the algorithm is shown in the top left panel of Fig. 5.3. The number drops quickly with iteration level.

#### 5.2.1.3 Assigning radii to different iterations

Before cuts can be made on the properties of the candidate voids, we need to assign to each a comoving radius on the sky. The void-finding algorithm naturally works in angular space, so we begin by mapping each iteration level at which a void was found to a specific angle. This is done empirically by binning the 2D LRG density around the candidate void centers for each iteration level, and taking the maximum of the LRG density ridge as the typical angle for that iteration. The LRG ridge around all voids from a given level is shown for four levels in Fig. 5.2. If the angle of the peak is plotted as a function of iteration level, as in the right panel of Fig. 5.2, the points all lie on a line, $\theta_{\rm v}/{\rm deg} = 0.32 \times ({\rm level}) + 0.24$. Above iteration level 8, the ridge becomes smeared out and the linear relationship has more scatter. However, since each level removes one more layer of pixels around the LRGs, the slope calibrated using the lower iterations can be extrapolated to the higher ones. Note also that the number of objects falls off quickly with iteration level (Fig. 5.3) so that any inaccuracies beyond level 8 are of diminishing importance. Thus, we use this linear relationship to assign $\theta_{\rm v}$ for all the void candidates. This angle is then converted to comoving distance according to

$$R_{\rm v} = r_{\rm los}\, \theta_{\rm v}\,, \tag{5.1}$$

where again $r_{\rm los}$ is the comoving distance to the void center.

### 5.2.2 Cleaning the catalog

Having found a large set of candidate voids numbering $\sim 68,000$ objects, we next remove those which are not likely to be legitimate large scale structures. These include chance

alignments of LRGs in the projection, fake voids due to the survey masks and edges, double holes joined by thin "necks," and multiple detections of the same holes.

#### 5.2.2.1 Cutting out chance projections

Objects with line-of-sight and transverse sizes which are very different in magnitude are likely to be chance alignments of holes in the sparse LRG sample. Thus we remove these with the requirement

$$s_{\rm v}/3 < R_{\rm v} < 3s_{\rm v}\,. \tag{5.2}$$

The vertical lines on the top center panel of Fig. 5.3 display this cut.

#### 5.2.2.2 Random point density

An unusually high number of candidate voids will be found at the survey edges and in regions where the LRG coverage is incomplete due to masking. In order to remove such spurious voids, we use the LRG random catalog from Kazin et al. (62), which has $\sim 16$ times as many objects as real LRGs. For each void candidate, we find the density of random points inside its angular radius $\theta_{\rm v}$. The histogram of densities is shown in the lower left panel of Fig. 5.3. The distribution is tightly peaked at 150 points/deg$^2$, with the densest voids having up to 200 points/deg$^2$. On the low-density end, there is a long tail stretching all the way to zero due to fake voids formed from unobserved regions. We remove the few hundred objects with density less than 100 points/deg$^2$ in this tail.

#### 5.2.2.3 Distance between pixels within a void

Recall that each candidate void was selected when a group of disconnected pixels fell below a pixel count threshold (§ 5.2.1.2). The arrangement of these remaining pixels tells us something about the nearby LRGs: if they are roughly circular around the void candidate center, then all pixels will be relatively close to that center. At the other extreme, the pixels

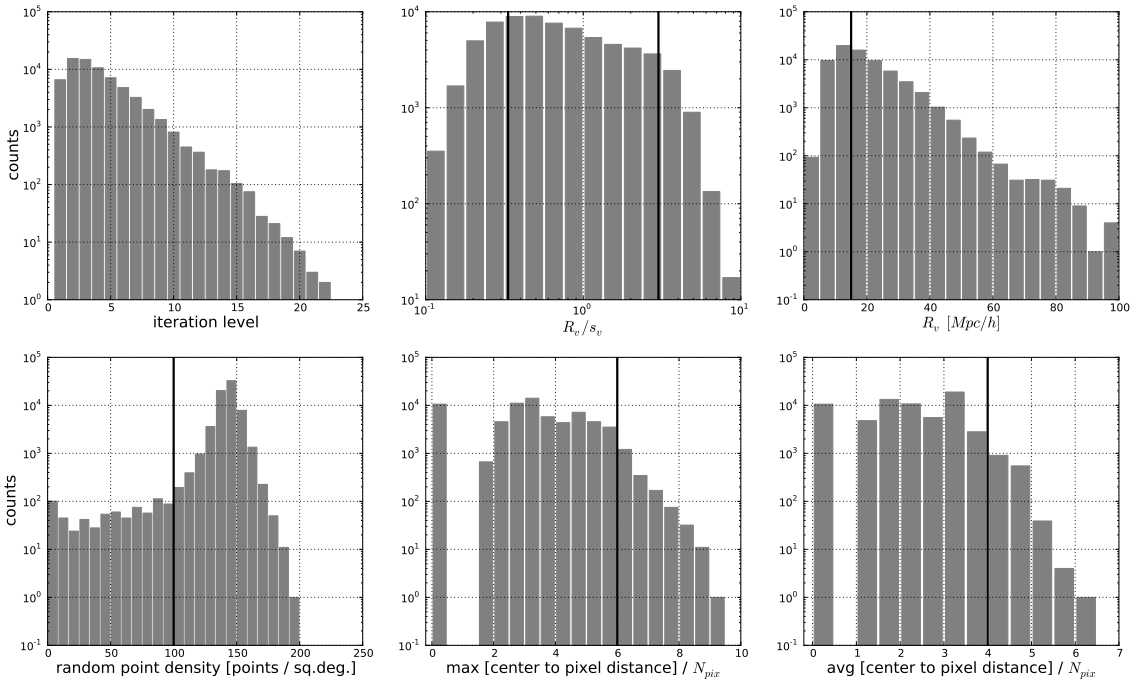


**Figure 5.3:** Histograms of various void candidate properties which we use to make cuts (solid vertical lines). The first panel shows the number of objects found at each iteration level of our algorithm. The second panel requires that the ratio of the void transverse to line-of-sight size $R_{\rm v}/s_{\rm v}$ be near unity, specifically $1/3 < R_{\rm v}/s_{\rm v} < 3$. In the third panel we remove the smallest voids, requiring 15 Mpc/$h$ $< R_{\rm v}$. The fourth panel cuts out false voids which appear near survey masks and edges, by looking at the density of random points within $R_{\rm v}$. The fifth and sixth panels cut on the maximum and average distance between void center and the remaining pixels which compose it (see text for details): the purpose is to remove objects which are far from circular on the sky. These cuts, plus those on volume overlap (see text for details) trim the void candidates down to a catalog of $\sim 19,000$ objects.

may lie along a line, so that some pixels will be much farther from the center than others. In the first case, the distance to the nearest LRGs will be nearly the same in all directions; in the second, the LRG ridge will be indistinct after azimuthally averaging. We expect a better lensing signal for the first case, prompting another set of quality cuts.

For each set of disconnected pixels that make up a void, we calculate the maximum and average of the center to pixel distance (in arcminutes), and divide by the total number of pixels in that set, $N_{\rm pix}$. These distributions are shown in the lower center and right panels of Fig. 5.3, respectively. The distances peak at $3' \times N_{\rm pix}$ but have a long tail stretching towards larger distances. We require a maximum distance below 6' $\times N_{\rm pix}$ and an average distance below 4' $\times N_{\rm pix}$ for each void, removing $\sim 3,000$ objects.

#### 5.2.2.4 Volume overlap between voids

Many 3D void finders assign each volume element uniquely to one void. (Even if an algorithm allows for sub-voids, these may be underdensities delineated from their parent voids by a small density wall or ridge.) In contrast, our method of finding voids in projected 2D slices requires oversampling the same volume using many different slice thicknesses. This is not a failure of the algorithm, but it does require an extra step to remove objects which are duplicates of the same underdensity. While we do not expect cosmological voids to be cylindrical, our algorithm finds cylindrically shaped regions free of galaxies. Thus for the purpose of removing duplicates we assign a volume $V = 2s_{\rm v} \times \pi R_{\rm v}^2$ to each object and the fractional volume overlap $f_{\rm vol}$ based on the neighbor with maximum overlap. Note that this is a significant overestimate of the actual overlap fraction for elliptical or irregularly shaped voids. Based on this metric, we discard voids that overlap completely with a larger voids.

Voids are not perfectly spherical and there are random variations in the LRG distribution. Many void finders aggressively join underdensities into a new void, and calculate a new center and effective radius. Our approach is quite different, but we can get some approximation to such algorithms by lowering $f_{\rm vol}$. However, since our main purpose is to make a lensing

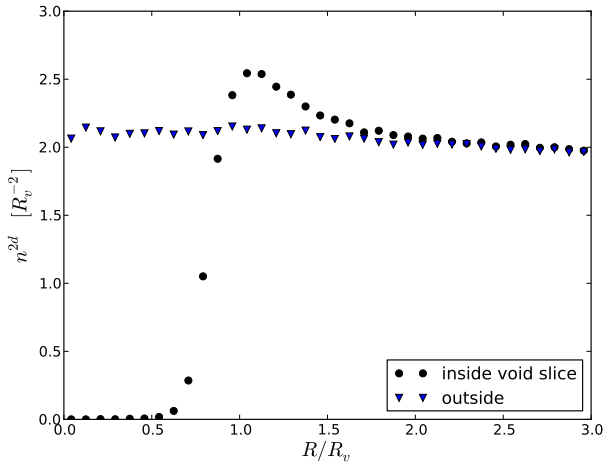


**Figure 5.4:** The average surface density of LRGs within the void slices, as well as in slices on either side of the void slice. This is a stack of all voids used in our lensing measurement. Note that for the outside regions the lowest density bin is only different from the highest by $\lesssim 10\%$. Thus, since the density of LRGs outside the slice is roughly the same at small and large $R/R_{\rm v}$, our estimate of the line-of-sight void size $s_{\rm v}$ is reasonable.

measurement of void density profiles, we do not want to give up the substantial reduction in shape noise relative to using just one center for each void, as discussed in § 5.3.4. Note that this is analogous to galaxy-galaxy lensing, where a given source galaxy contributes to the density profile of multiple lens galaxies since its shape is projected along different directions for different lens centers. The volume overlap for galaxy-galaxy lensing also exceeds ours for the scales of interest.

We find that the volume fraction in our void sample is about 0.7. Requiring $f_{\rm vol} < 0.5$ our volume fraction drops below 0.5, close to the results in the literature. We have checked that our measured density profiles are not sensitive to the change in the $f_{\rm vol}$ cutoff: presumably since voids have very shallow profiles they are not affected by the exact location of the center. The shift in the parameter contours for voids with $f_{\rm vol} < 0.5$ is less than $1\sigma$, as will be shown in Fig. 5.8.

### 5.2.3 LRG surface density

We have sought to assign the line-of-sight and projected void sizes, $s_{\rm v}$ and $R_{\rm v}$, based purely on the LRG distribution. However, since we have only considered the LRGs within the void's own slice, it is not clear that the assigned $s_{\rm v}$ is a good choice. We expect that if the $s_{\rm v}$ values assigned by the preceding algorithm are accurate, then the 2d LRG density at the void radius, just outside the void slice should not have a significant decrement relative to the value far from the void center.

In Fig. 5.4 we show the LRG density within the slice of interest, i.e., LRGs within $r_{\rm los} - s_{\rm v} < r_{\rm lrg} < r_{\rm los} + s_{\rm v}$, where $r_{\rm lrg}$ is the line-of-sight comoving distance of the LRG and $r_{\rm los}$ is the same for the void center. This results in a smoothed out version of the high peaks in Fig. 5.2, since it includes voids found at all iterations of the void-finder. The peak is lined up for all voids by binning in units of the void radius $R_{\rm v}$. By $3R_{\rm v}$ the LRG density has leveled off near the cosmic mean.

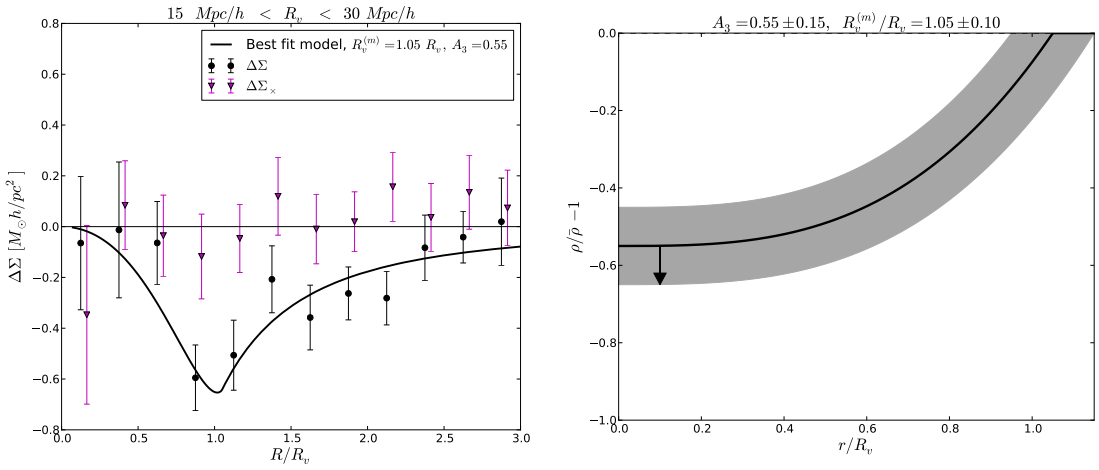


**Figure 5.5:** The left panel shows our measurement of the tangential shear (black circles) and cross-component (magenta triangles) around our void centers, stacked in units of $R_{\rm v}$. Our best-fit model (solid line) has $R_{\rm v}^{(m)} = 1.05\,R_{\rm v}$ and $A_3 = 0.55$. Our estimated 3d density profile is shown in the right panel, along with the estimated $1\sigma$ uncertainty. The arrow gives a sense of our model independent estimates, which prefer a lower central density (by up to $0.1\bar{\rho}$) than allowed by our model.

We also show the LRG surface density just outside the void slice, $r_{\rm los} - 2s_{\rm v} < r_{\rm lrg} < r_{\rm los} - s_{\rm v}$ or $r_{\rm los} + s_{\rm v} < r_{\rm lrg} < r_{\rm los} + 2s_{\rm v}$. This range is chosen so that the integrated line-of-sight distance, $2s_{\rm v}$, is the same both inside and outside the void slice. Even at the innermost bin, the LRG density outside has risen back to a comparable value to that at $3R_{\rm v}$. This is good evidence that the slice thickness of $2s_{\rm v}$ is a reasonable value for the void size in the line-of-sight direction.

## 5.3 Lensing Measurement

The shear catalog is composed of 34.5 million sources, and is nearly identical to that used in Sheldon et al. (117): see that work for further details of the catalog. The source redshift

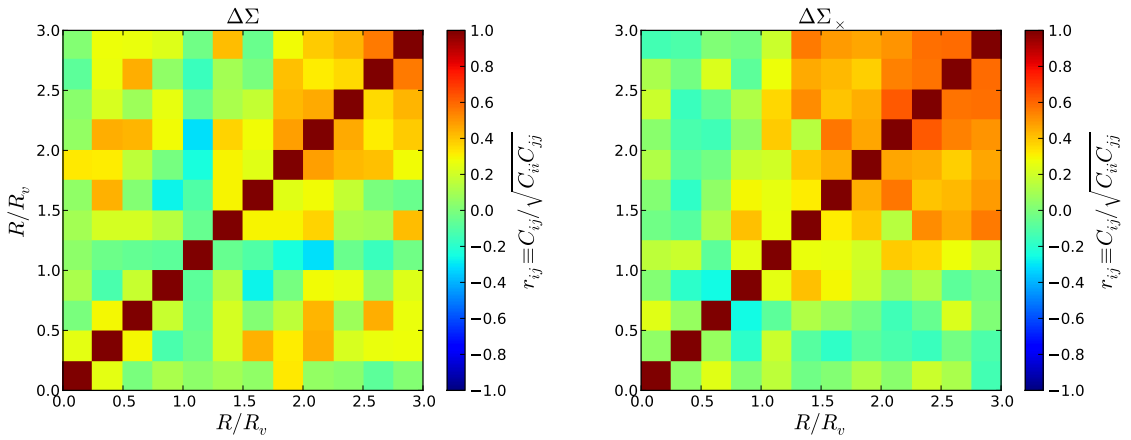


**Figure 5.6:** Our covariance matrices for $\Delta\Sigma$ (*left panel*) and $\Delta\Sigma_\times$ (*right panel*). Off diagonal correlations are significant beyond $2R_\mathrm{v}$, since source galaxies in these bins are shared among multiple voids.

distribution is obtained by stacking the posterior probability distribution of the photometric redshift for each source, $P(z_\mathrm{s})$. Its peak is at $z \sim 0.35$, and it has a substantial tail extending out to higher redshifts. The full distribution is shown in Fig. 4 of Clampitt et al. (17), which uses precisely the same source catalog.

In what follows, we describe our lensing measurement procedure. Following the method in Mandelbaum et al. (79), we use, as the lensing observable, the stacked surface mass density field at the radial distance $R$ in the region around each void, estimated from the measured shapes of background galaxies as

$$\Delta\Sigma_k(R; z_\mathrm{L}) = \frac{\sum_j \left[ w_j \left( \left\langle \Sigma_\mathrm{crit}^{-1} \right\rangle_j (z_\mathrm{L}) \right)^{-1} \gamma_k(R) \right]}{\sum_j w_j} \tag{5.3}$$

where the summation $\sum_j$ runs over all the background galaxies in the radial bin $R$, around all the void centers, the $k$ indices denote the two components of shear (tangential or cross),

and the weight for the $j$-th galaxy is given by

$$w_j = \frac{\left[\left\langle \Sigma_{\rm crit}^{-1} \right\rangle_j (z_{\rm L})\right]^2}{\sigma_{\rm shape}^2 + \sigma_{{\rm meas},j}^2}. \tag{5.4}$$

We use $\sigma_{\rm shape} = 0.32$ for the typical intrinsic ellipticities and $\sigma_{{\rm meas},j}$ denotes measurement noise on each background galaxy ellipticity. $\left\langle \Sigma_{\rm crit}^{-1} \right\rangle_j$ is the lensing critical density for the $j$-th source galaxy, computed by taking into account the photometric redshift uncertainty:

$$\left\langle \Sigma_{\rm crit}^{-1} \right\rangle_j (z_{\rm L}) = \int_0^\infty {\rm d}z_{\rm s} \Sigma_{\rm crit}^{-1}(z_{\rm L}, z_{\rm s}) P_j(z_{\rm s}), \tag{5.5}$$

where $z_{\rm L}$ is the redshift of the void and $P_j(z_{\rm s})$ is the probability distribution of photometric redshift for the $j$-th galaxy. Note that $\Sigma_{\rm crit}^{-1}(z_{\rm L}, z_{\rm s})$ is computed as a function of lens and source redshifts for the assumed cosmology as

$$\Sigma_{\rm crit}^{-1}(z_{\rm L}, z_{\rm s}) = \frac{c^2}{4\pi G} \frac{D_A(z_{\rm s})(1+z_{\rm L})^{-2}}{D_A(z_{\rm L}) D_A(z_{\rm L}, z_{\rm s})}\,, \tag{5.6}$$

where the $(1+z_{\rm L})^{-2}$ factor is due to our use of comoving coordinates, and we set $\Sigma_{\rm crit}^{-1}(z_{\rm L}, z_{\rm s}) = 0$ for $z_{\rm s} < z_{\rm L}$ in the computation.

### 5.3.1 Jackknife Realizations

We divide the voids into 30 spatial jackknife regions, shown in Fig. 3 of Clampitt et al. (17). Note that we exclude the low-DEC stripes from our analysis: they are sub-optimal for void finding due to a high ratio of perimeter to area. The remaining area is approximately 7,500 square degrees. We perform the measurement multiple times with each region omitted in turn to make $N = 30$ jackknife realizations. The covariance of the measurement (97) is given by

$$C[\Delta\Sigma_i,\Delta\Sigma_j] = \frac{(N-1)}{N} \times \sum_{k=1}^{N} \left[(\Delta\Sigma_i)^k - \overline{\Delta\Sigma_i}\right] \left[(\Delta\Sigma_j)^k - \overline{\Delta\Sigma_j}\right] \tag{5.7}$$

where the mean value is

$$\overline{\Delta\Sigma_i} = \frac{1}{N}\sum_{k=1}^{N}(\Delta\Sigma_i)^k\,, \tag{5.8}$$

and $(\Delta\Sigma_i)^k$ denotes the measurement from the $k$-th realization and the $i$-th spatial bin. The covariance is measured for both components of shear; for clarity we do not denote the separate components in Eqs. 5.7 and 5.8.

### 5.3.2 Null tests

We measure the tangential shear around random points and cross-component around voids, both of which should be consistent with the null hypothesis. For $N = 12$ bins and no model parameters ($n = 0$), the null has expected $\chi^2$:

$$\begin{aligned}\langle\chi^2\rangle_{\rm null} &= N - n \pm \sqrt{2N + 2n} \\ &= 12 \pm 4.9\,.\end{aligned} \tag{5.9}$$

We perform the random points test by giving each void with radius $R_{\rm v}$ and redshift $z$ a random location in the survey area, avoiding masked regions in the same way as the LRG catalog. Often tests involving random points use many more random points than lens galaxies, but since void lenses are so large and many source galaxies fall in each radial bin, we need only use as many random points as we have void positions. The result for the tangential shear around random points is a $\chi^2 = 16.7$, within $1\sigma$ of the null hypothesis.

The cross-component is shown in Fig. 5.5 (pink triangles), and with a $\chi^2 = 8.2$ it is also within $1\sigma$ of the null hypothesis.

### 5.3.3 Tangential shear profile

We show the stacked lensing profile of the voids in the left panel of Fig. 5.5. The most significant and largest amplitude $\Delta\Sigma$ values of $\sim -0.6 M_\odot h/pc^2$ occur at the void radius $R_{\rm v}$. The signal remains significant out to $\sim 2.5 - 3R_{\rm v}$. The covariance, shown in Fig. 5.6, is

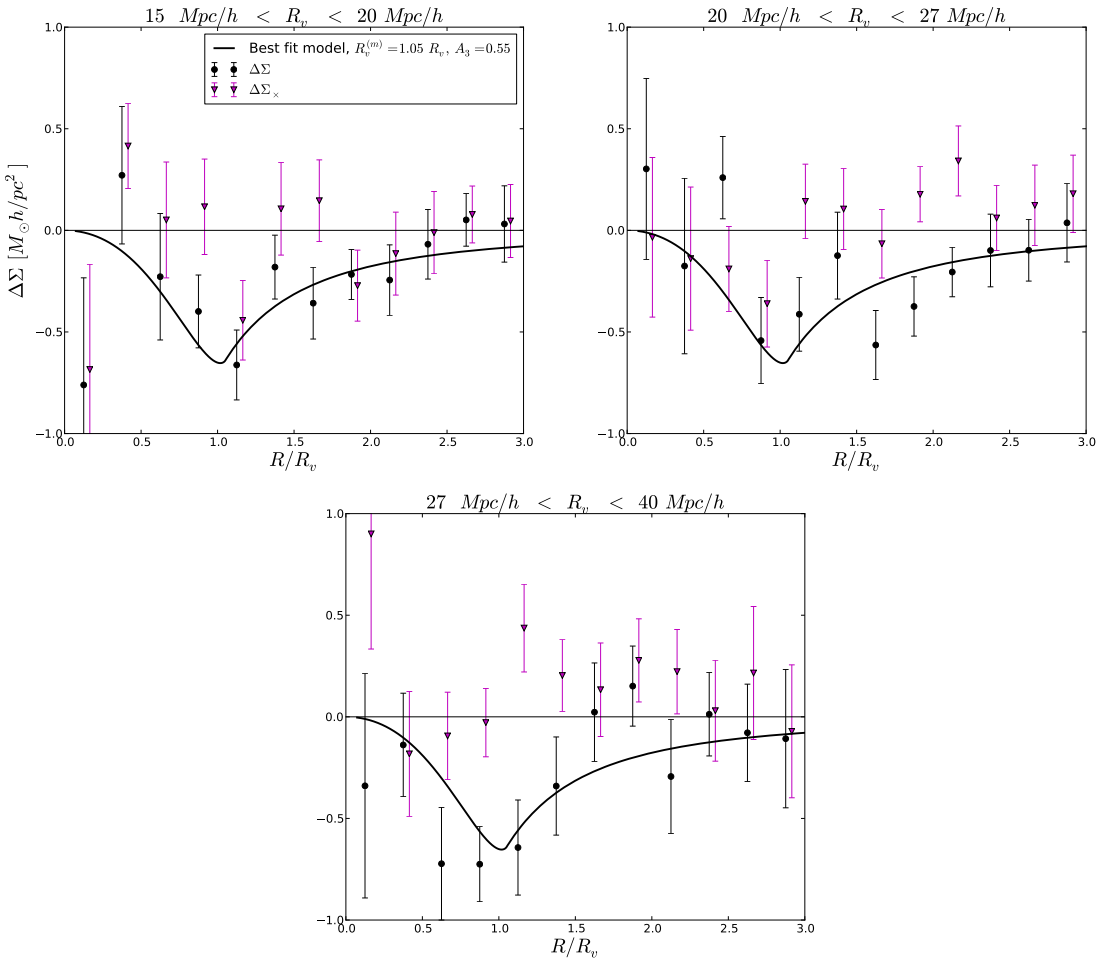


**Figure 5.7:** Dependence of lensing signal on void size $R_{\rm v}$. We divide our fiducial measurement (Fig. 5.5) into several bins, and also extend the range to $R_{\rm v} = 40$ Mpc/$h$. The signal is clearly consistent over a wide range of void sizes, which is a useful test. It has no significant trend with $R_{\rm v}$. This may be due to the small number of voids above $\sim 30$ Mpc/$h$, as well as their large covariance between bins.

used to calculate the detection significance. Comparing the signal to the null hypothesis, we have $\chi^2 = 94.2$ (78.7), a $16.7\sigma$ ($13\sigma$) inconsistency for the pictured fiducial case (overlaps well below 50% case).

This high significance detection is further supported by the null tests described above. We check our measured statistical significance with a rough analytical estimate of the signal-to-noise below. We then discuss the implications for void density profiles.

The covariance matrix is largely diagonal up to 1.5 $R_{\rm v}$. At large $R$ the off diagonal elements are mostly positive, presumably since multiple projections of source galaxies provide less independent information about the voids. In Fig. 5.7 we show three size bins. No systematic trend in magnitude or shape of the signal is visible from these plots. The consistency of the signal across size bins that span nearly a factor of three in void radius validates the lensing interpretation.

### 5.3.4 Analytical signal-to-noise estimate

We present two checks of our measurement: an analytical estimate of signal-to-noise for void lensing as well as a comparison to the signal-to-noise in SDSS galaxy-galaxy lensing. The tangential shear around a void is given by

$$\gamma_t = \frac{\Delta\Sigma}{\Sigma_{\rm crit}} = \frac{\Sigma(<R) - \Sigma(R)}{\Sigma_{\rm crit}} \tag{5.10}$$

where $\Sigma_{\rm crit}$ is defined above and is $\Sigma_{\rm crit} \approx 6000 M_\odot/pc^2$ for our typical lens and source redshifts. Inside the void radius the signal can be anticipated using the results of Krause et al (2013): $\Delta\Sigma \approx -0.6 M_\odot/pc^2$ (adjusted for the fact that our mean void radius is larger than the range considered in Krause et al). Hence the typical tangential shear is $\gamma_t \approx 10^{-4}$.

Since our voids and therefore source galaxies are at high redshift, shape and measurement noise both contribute to the errors. We take the noise on the *shear* of a given background source to be $\sigma = \sqrt{\sigma^2_{\rm shape} + \sigma^2_{\rm m}} \sim 0.3$. With a source number density $n \approx 0.5/{\rm arcmin}^2$, we can then estimate the noise contribution on a stacked void lensing measurement. For

$N_v$ voids of radius $\theta_v$, we get a sky coverage that exceeds $N_v\pi(2\theta_v)^2$ since the signal is measured out to at least twice the void radius. This gives a total effective number of sources $N_{\rm source} = nN_v\pi(2\theta_v)^2 \approx 1 - 2 \times 10^9$. This is at least thirty times larger than the actual number of source galaxies since each galaxy shape is used multiple times: it is projected along different directions for different void centers. As discussed above in Section is a valid procedure in cross-correlations such as ours and galaxy-galaxy lensing. The estimated shape noise is then $\sigma_{\rm shape}/\sqrt{N_{\rm source}} \approx 0.7 - 1 \times 10^{-5}$. The uncertainty is mainly due to the choice of a single void size to represent the distribution. The estimated signal to noise is:

$$\mathrm{S/N} \approx 12. \tag{5.11}$$

While the estimate above involves several approximations, it gives us a reality check on our measurement. One might still worry that shears at the $10^{-4}$ level are dominated by systematic errors. Indeed for shear-shear correlations from SDSS, that appears to be the case due to additive systematics that are spatially correlated. Such terms however cancel out of cross-correlations. Published measurements of galaxy-galaxy lensing demonstrate this: at distances greater than 10 Mpc the signal falls below $10^{-4}$, see e.g. Figure 6 in Mandelbaum et al (2013). We have checked that the signal-to-noise of that measurement is consistent with ours, adjusting for the smaller number of source galaxies in their angular bin. Of course closer to the center the galaxy halo overdensity far exceeds the amplitude of the void underdensity, so integrated over all scales the significance of the galaxy-galaxy lensing measurement is higher.

### 5.3.5 Comparison with other work

The strength of our detection may be surprising given other work on void lensing. In particular, Melchior et al. (85) used a conservative sample of a relatively conservative void finder (125) which was not optimized for lensing purposes. All these factors make a difference in the potential S/N:

- Melchior et al. (85) used the "central" sample of Sutter et al. (125); for *lrgdim* (the sample most comparable to ours) the usable volume is only 75% of the total. Furthermore, the void volume fraction is less in the central sample than in the total, where both volume fractions are calculated with respect to their own usable volumes. We make a related quality cut, but which only removes $\sim 1\%$ of our sample (Fig. 5.3, lower left panel).

- Over most of the volume where Sutter et al. (125) can compare with Pan et al. (101), the former finds only half as many voids. This is for the main SDSS galaxy sample, but it is indicative of a difference in void finder aggressiveness between the two methods.

- Another point worth noting is that our assignment of void radii on the sky is optimized for lensing by setting $R_{\rm v}$ to the distance to the LRG ridge in the plane of the sky. Sutter et al. (125) starts with the void volume and then assign the void radius as $R_{\rm eff} = (3V/4\pi)^{1/3}$, which is used by Melchior et al. (85) to bin the background shears. Converting in this way from volume to an effective void radius assumes all three dimensions are the same, but for lensing purposes the line-of-sight size of the void is much less important than its size on the sky. We have tested the effect of assigning an $R_{\rm eff}$ as described above to each of the voids in our fiducial sample and then remeasuring $\Delta\Sigma$ binned in $R/R_{\rm eff}$. The result is an increase in our errors such that the detection significance drops from $16.7\sigma$ to $12.5\sigma$.

## 5.4 Void density profile

### 5.4.1 Model constraints

The 3-dimensional density profiles of voids have been studied using simulations and other theoretical approaches. One of the subtle issues is how to transition from the underdensity of the void to the cosmic mean density $\bar{\rho}$ at a sufficiently large distance from the void

center. Typically a small transition zone outside the void radius allows for some degree of compensation of the profile, i.e., a region of density higher than $\bar{\rho}$. In perfectly compensated voids models, the enclosed mass at about two times the void radius is exactly the same as the mass enclosed in a region of the same size with constant density $\bar{\rho}$.

Lavaux & Wandelt (68) fit a cubic profile inside the void radius using simulations, and Krause et al. (65) gives the lensing prediction for this model. We use the cubic profile up to the void radius, but outside the void we use a constant density profile. Thus we require continuity at the void radius but not exact compensation. The resulting profile is given by

$$\rho(r, R_{\rm v}) = \begin{cases} \bar{\rho}[A_0 + A_3(r/R_{\rm v}^{(m)})^3] \text{ for } 0 < r < R_{\rm v}^{(m)} \\ \bar{\rho}[A_0 + A_3] \qquad \text{for } R_{\rm v}^{(m)} < r \end{cases} , \tag{5.12}$$

where $A_0, A_3$, and $R_{\rm v}^{(m)}/R_{\rm v}$ are model parameters. However, we are not sensitive to $A_0$, and so have assumed its value is set by requiring that the 3d density returns to the cosmic mean density outside the void, thus $A_0 = 1 - A_3$. Then our fit just involves two parameters, $A_3$ and $R_{\rm v}^{(m)}/R_{\rm v}$, which are constrained as in Fig. 5.8. For our two parameter model the expected chi-square is $\langle\chi^2\rangle = 10 \pm 5.3$ so that the $\chi^2 = 13.8$ of the best-fit model is acceptable. The right panel of Fig. 5.5 shows the corresponding 3d density profile for our best-fit parameters.

If we were to require compensation, as in some models explored by Krause et al. (65), we would put some constraints on $A_0$. Note also that Higuchi et al. (40) apply the (47) void finder to ray-traced simulations, and their tangential shear profiles look compensated just beyond the void radius. However, assuming that $\Sigma = \bar{\Sigma}$ by $2R_{\rm v}$ (see below), the data clearly prefers an uncompensated void inside $2R_{\rm v}$. This is shown by the negative values of the measured $\Delta\Sigma$ up to and beyond $2R_{\rm v}$ (it should be zero for a compensated void if $\Sigma(2R_{\rm v}) \to \bar{\Sigma}$). We see no evidence for a ridge of density well above $\bar{\rho}$ just beyond $R_{\rm v}$, as suggested by the LRG profiles for the small voids. The data in fact support a projected density below the mean at $R_{\rm v}$. More work is needed to understand the relationship of the LRGs to the mass profile as we expect that our void finder played some role in the details of the LRG profile.

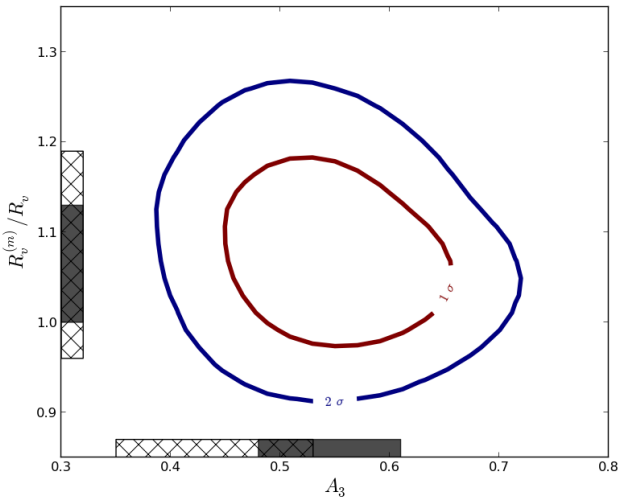


**Figure 5.8:** Contours show the limits on our model parameters. $R_{\rm v}^{(m)}$, the radius at which the density profile transitions from cubic to constant, is constrained to be near the LRG ridge determined from the data. Solid gray bands on the x- and y-axes show 1d marginalized constraints for both parameters. The constraints for the case requiring volume overlaps of less than 50% are consistent with our fiducial model (hatched bands).

While the minimum density at the center of the void is formally not constrained by the data, we find that the requirement that the density approach the mean at large radii, coupled with measurements between $R_{\rm v}$ and $2R_{\rm v}$, leave little freedom. We explored modifications to the density profile beyond $R_{\rm v}$ and find that $A0$ can be lowered by at most 0.1. The arrow in Fig. 5.5 (right panel) pointing to lower central densities indicates this possibility.

The solid gray bands on the x- and y-axes of Fig. 5.8 show 1d marginalized constraints for both parameters. The hatched bands of Fig. 5.8 compare the effect of stricter criteria for void overlap, for the case with overlaps well below 50%. The constraints are degraded due to throwing away a large fraction of overlapping voids, but the shift in the contours is negligible for $R_{\rm v}^{(m)}$ and just over $1\sigma$ for $A_3$.

### 5.4.2 Estimated mass deficit inside the voids

Since the measured $\Delta\Sigma = \Sigma(< R) - \Sigma(R)$, we can estimate $\Sigma(< R_{\rm v})$ once we require $\Sigma$ to approach $\bar{\Sigma}$ at some large radius. At radii above $2R_{\rm v}$ both the galaxy distribution and the mass in simulations are close to the mean density. These are large scales, typically above 40 Mpc/$h$, so it is reasonable to expect that there aren't departures at more than a few percent level from mean density in the data as well. We therefore use our measurements at about $2R_{\rm v}$ to estimate $\Sigma(< R_{\rm v})$ with this assumption. We test it by checking the range $1.5 - 2.5R_{\rm v}$, at which our signal to noise is still reasonable.

The results for the mass deficit and fractional mass deficit are shown in Table 1. Three methods are used: directly from the data as described above, using our best fit for $\rho(r)$, and using the best fit $\rho(r)$ from voids in N-body simulations with a similar tracer to our LRG halos (such tracers enclose voids with more mass in small scale structure than in voids identified using dark matter particles – Sutter et al. (128) and Sutter, private communication). Each estimate involves some assumptions or caveats which are briefly described in the table. The mass deficit

$$\delta M = \frac{4\pi}{3} R_{\rm v}^3 \left[\rho(< R_{\rm v}) - \bar{\rho}\right] \tag{5.13}$$

| **Method** | $\delta M(< R_{\rm v})$ | $\rho(< R_{\rm v})/\bar{\rho} - 1$ | $\Sigma(< R_{\rm v})/\bar{\Sigma} - 1$ | **Assumptions** |
|---|---|---|---|---|
| Measured $\Delta\Sigma$ | – | – | -0.3 | $\Sigma(R) \rightarrow \bar{\Sigma}$ at $R \approx 2R_{\rm v}$ |
| Best fit model | $-1 \times 10^{15} M_{\odot}$ | -0.4 | -0.32 | Recover $\bar{\rho}$ at $R \approx R_{\rm v}$ |
| Simulations fit | $-1.4 \times 10^{15} M_{\odot}$ | -0.5 | -0.44 | Different void finder. |

**Table 5.1:** Estimated mass deficit $\delta M$ and the fractional deficit in the 3d density $\rho$ and projected density $\Sigma$ at the void radius $R_{\rm v}$. The measurements, interpreted without a model in the first row, give us only projected quantities. For the model fits we give both 2d and 3d versions of the fractional density contrast. We set $R_{\rm v} = 20$ Mpc/$h$ to estimate $\delta M$; for voids with other values of $R_v$, $\delta M$ scales approximately as $R_v^3$. See text for discussion of the dependence on the LRG sample and the simulation fits.

is estimated for the 3d model fit and the fit to simulations.

While we have not attempted to place rigorous bounds on our estimated $\delta M$ values, we can see the trends between data and simulations: the two methods of estimation from the data are in reasonable agreement, and involve more mass inside voids than in simulations (the deficit is about 40% higher in the simulation fits). Projection effects and flaws in the void finder would lead us to overestimate the mass enclosed. We also note that we extended the profile from $R_{\rm v}$ to $2R_{\rm v}$ using different models, including a possible ridge of density above the mean, but find that the measurements leave little wiggle room.

Our measurements indicate significant levels of underdensity inside the void radius: the inferred 3d fractional under density is $\approx -0.3$ to $-0.4$ inside $R_{\rm v}$. This corresponds to mass deficits comparable to the masses of the most massive clusters in the universe. The bigger voids in our sample will have up to ten times the mass deficit. Given that our LRG sample has a bias factor of about 2, we expect that voids using a less biased tracer would have lower central densities. Simulations with mock catalogs also support this trend (128). We leave for future work the details of the mass profile and its relationship to the galaxy sample and void finder.

## 5.5 Discussion

*Void Lensing Detection.* We have made the first statistically significant measurement of gravitational lensing by large voids (Fig. 5.5), ruling out the null hypothesis with a significance of about $13 - 16\sigma$ depending on the cuts made on the void finder. This detection may be surprising given that theoretical work (65) predicted that ambitious future surveys (in particular, Euclid) would be needed for measurements with comparable signal-to-noise. We differ from previous work in that our void finder and void characterization is optimized for lensing. We work with projected 2d slices and have a flexible criterion that allows for some overlap between voids. Our stacked shear measurement is analogous to galaxy-galaxy lensing in that it projects a source galaxy shape along multiple void centers. This greatly increases the total number of lens-source pairs and reduces shape noise by a factor of several. Other improvements described in Section 2 contribute to the size and quality of our void sample.

We validate our detection of void lensing in several ways, using both the LRG positions around voids and standard galaxy-shear tests. Figures 5.3 and 5.4 show the validation and improvements based on the LRG distribution. We verify that the tangential shear around random points and the lensing cross-component around void centers are consistent with the null hypothesis. The error analysis is analogous to that for our measurement of filament lensing with the same dataset presented in Clampitt et al. (17).

*Void density profiles.* We measure the stacked density profile of voids with radii $R_v = 15 - 40$ Mpc$/h$ in 12 radial bins. We can make some model-independent statements about void properties (see Table 1). By requiring the projected density to approach the mean density at radii of $2R_{\rm v}$ or larger, we can convert our measured $\Delta\Sigma$ to estimates of $\Sigma(< R_{\rm v})$ and therefore to the fractional density contrast at $R_{\rm v}$. We further estimate the mass deficit $\delta M$. In addition, we find that our voids are uncompensated within twice the void radius. By $3R_{\rm v}$ however, the measurements are consistent with fully compensated voids, but we see

no evidence for overcompensated voids of the kind seen in simulations (at the lower end of our $R_{\rm v}$ range).

By fitting our measurements with a model motivated by simulations, we can draw conclusions about the voids' 3d density profile and mass deficit $\delta M$ as summarized in Table 1. Our data is consistent with a central density of $\approx 0.6\bar{\rho}$. At the edge of the void, it is also consistent with a density below the mean density at the LRG ridge, though the corresponding 2d density of LRGs is above the mean (Fig. 5.4).

*Caveats.* The standard disclaimer with void-related work is that the results can be quite sensitive to the specific void-finder used. As highlighted above, this holds true also for our work which is designed to find voids for gravitational lensing. Our use of multiple potential void centers is helpful for lensing S/N reasons, but also makes interpretation of the resulting density profile less straightforward. We expect some miscentering between the lowest dark matter density and the emptiest places in the sparse galaxy density, and our multiple centers may also add to this miscentering in some instances. However since the density profiles are very flat between the center and half the void radius, these effects are far less problematic than for galaxy or cluster lensing.

We expect our error bars accurately account for shape noise and sample variance. However, we have not accounted for possible shear calibration errors, which could bias the signal by up to 5%. In addition, two effects could result in a dilution of the signal and thus underestimation of $A_3$: inaccurate source redshifts or fake voids from chance LRG projections. We have not estimated the contribution of these effects.

*Future Work.* We can attempt a void lensing measurement with several different variants of the void sample. Going beyond our sparse sample of LRGs, we can apply this void finder to the SDSS Main sample. Although the volume probed will be significantly smaller, this disadvantage is offset in part by the larger number of background sources available behind lower redshift voids. Furthermore, Sutter et al. (128) find that the voids identified using

a lower galaxy luminosity threshold have a lower central dark matter density (as expected based on their lower galaxy bias as well), which should increase the lensing effect.

Nearly all detailed applications will require a careful study of our void selection via mock catalogs that create galaxies from HOD prescriptions or dark matter halos. Our measurements are now confined to $R_{\rm v} > 15$ Mpc$/h$, in part because the contamination from fake voids due to projection effects gets worse as the void size gets smaller than the 2d tracer density. Mock catalogs will allow us to go down to smaller radii and estimate the number of fake and real small voids. With those numbers we can take into account the expected dilution of the signal.

The comparison of the galaxy distribution with the mass distribution is of great interest. The question of galaxy biasing can be understood better by having measurements in under dense regions to complement those in over dense regions. Many other questions can be posed by stacking voids in different ways: along the major axis of the galaxy distribution, varying the environment and the properties of the galaxy population, and so on. The measurement of a magnification signal behind voids would be of interest, in particular to provide a direct measurement of $\Sigma(R)$.

Void mass functions, mass profiles, and the cross-correlation with galaxy profiles are the key ingredients in cosmological applications of voids. The velocity profiles measured in SDSS have an anisotropy and relationship to the mass profile that carry cosmological information (68). Modified gravity theories in particular predict differences in these observables. In many respects modeling voids is less problematic than massive nonlinear objects like galaxy clusters, and the measurements are not affected by foreground galaxies, but the use of mock catalogs to understand the selection effects in the data is likely to be essential to interpreting survey measurements.

# Appendices

# Appendix A

# Newtonian force of host

Here we show the result of integrating the density profile of eq. (2.20) to find the Newtonian force of the host component. We have

$$\begin{aligned}
\frac{d\Psi_N}{dr}(r) &= \frac{G}{r^2}M(<r) \\
&= \frac{G}{r^2}4\pi\int_0^r dr' r'^2 \langle\rho_{\rm h}\rangle(r') \\
\frac{d\Psi_N}{dr}(r) &= \frac{16\pi G\rho_0 r_{\rm s}^3}{r^2}\left[-\frac{r}{d}+\left(1+\frac{r_{\rm s}}{d}\right)\ln\left(\frac{r+d+r_{\rm s}-\sqrt{(d+r_{\rm s})^2-r^2}}{r-d-r_{\rm s}+\sqrt{(d+r_{\rm s})^2-r^2}}\right)\right], \quad r\le d \\
&= \frac{16\pi G\rho_0 r_{\rm s}^3}{r^2}\left[-1+\left(1+\frac{r_{\rm s}}{d}\right)\ln\left(\frac{2d+r_{\rm s}-\sqrt{2dr_{\rm s}+r_{\rm s}^2}}{-r_{\rm s}+\sqrt{2dr_{\rm s}+r_{\rm s}^2}}\right)\right. \\
&\quad \left.+\frac{1}{2}\left(1-\frac{r_{\rm s}}{d}\right)\ln\left(\frac{r+r_{\rm s}-d}{r_{\rm s}}\right)+\frac{1}{2}\left(1+\frac{r_{\rm s}}{d}\right)\ln\left(\frac{r+r_{\rm s}+d}{2d+r_{\rm s}}\right)\right], \quad d\le r
\end{aligned} \tag{A.1}$$

# Appendix B

# Variations of host-satellite separation

Although using the averaged host profile of eq. (2.20) preserves spherical symmetry, we must still solve the nonlinear eq. (2.14) for each choice of host-satellite separation $d$. To see the effect of varying this parameter continuously, we make a different approximation. If the symmetron profile of the host at the location of the satellite has value $\phi_{\rm host}(d)$, and this value varies little across the diameter of the satellite, we can instead solve the approximately equivalent system of an isolated satellite with asymptotic field value $\phi(r \to \infty) = \phi_{\rm host}(d)$.

Figure B.1 plots the satellite force deviation at $1R_{\rm sat}$ as a function of $d$. This is done using two different approximations: the method using the asymptotic value of the field appropriate for a small object at distance $d$ from the host and the total density profile method of eq. (2.20). Plotting continuous curves for the latter is impractical: the shooting method must be employed to solve eq. (2.14) for each distance $d$. Fortunately, a discrete set of points shows the trend sufficiently well.

We see that the computationally much simpler asymptotic value method approximates well the more sophisticated average density calculation as long as the host and satellite masses are within 2 orders of magnitude. Here the simpler method overestimates the fifth force by only $5 - 30\%$ $F_{\rm N}$ over the range of separations considered. The differences exceed

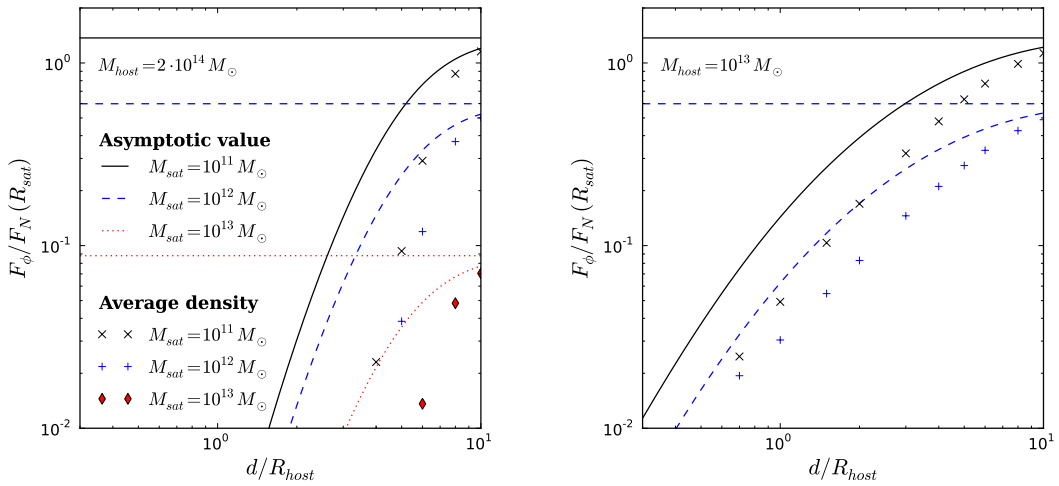


**Figure B.1:** (*left panel*): Satellite force deviation $F_\phi/F_{\rm N}$ at 1 $R_{\rm sat}$ as a function of center-to-center distance $d$ from a nearby host halo. Continuous lines display the result using the asymptotic value of the field appropriate for a relatively small object at distance $d$ from the host (see text for details). Satellite masses $M_{\rm sat} = 10^{11}, 10^{12}, 10^{13} M_\odot$ correspond to solid, dashed, and dotted curves, respectively. Also shown for the same range of masses are the results using the total density profile of eq. (2.20) applied at a discrete set of points. Horizontal lines show the force deviation of isolated satellites. The host mass is $2 \times 10^{14} M_\odot$. For the $10^{11}$ and $10^{12} M_\odot$ satellites, the screening from the host has a significant ($\sim 10\%$) effect even at separations of $\approx 7 - 8\ R_{\rm host}$. (*right panel*): Same as left, but for a host mass of $10^{13} M_\odot$.

this level for the case of a $10^{11} M_{\odot}$ halo in the neighborhood of a $2 \times 10^{14} M_{\odot}$ host, but only at separations of 5-6 $R_{\rm host}$ where it reaches $\approx 50\%$.

# Appendix C

# Excursion Set Theory

It is widely accepted that the large-scale structure (LSS) in the Universe has developed hierarchically through gravitational instability. The excursion sets (regions where the matter density exceeds some threshold when filtered on a suitable scale) generally correspond to sites of formation of virialised structures (10, 20, 21, 28, 29, 90, 112).

The filtered, or smoothed, matter density perturbation field $\delta(\mathbf{x}, R)$, is given by

$$\begin{aligned} \delta(\mathbf{x}, R) &= \int W(|\mathbf{x}-\mathbf{y}|; R)\delta(\mathbf{y})\mathrm{d}^3\mathbf{y}, \\ &= \int \tilde{W}(k; R)\delta_{\mathbf{k}} e^{i\mathbf{k}\cdot\mathbf{x}}\mathrm{d}^3\mathbf{k}, \end{aligned} \tag{C.1}$$

where $W(\mathbf{r}; R)$ is a filter, or window function, with radius $R$, and $\tilde{W}(k; R)$ its Fourier transform; $\delta(\mathbf{x}) \equiv \rho(\mathbf{x})/\bar{\rho} - 1$ is the true, unsmoothed, density perturbation field and $\delta_{\mathbf{k}}$ its Fourier transform; we will always use an overbar to denote background quantities.

As usual, we assume that the initial density perturbation field $\delta(\mathbf{x})$ is Gaussian and specified by its power spectrum $P(k)$. The root-mean-squared (rms) fluctuation of mass in the smoothing window is given by

$$S(R) \equiv \sigma^2(R) \equiv \langle \delta^2(\mathbf{x}; R) \rangle = \int P(k)\tilde{W}(k; R)\mathrm{d}^3\mathbf{k}. \tag{C.2}$$

Note that, given the power spectrum $P(k)$, $S$, $R$ and $M$ are equivalent measures of the scale of a spherical perturbation and they will be used interchangeablly below.

If $\tilde{W}(k;R)$ is chosen to be a sharp filter in k-space, then the increment of $\delta(\mathbf{x};R)$ as $R \to R - \delta R$ or equivalently $S \to S + \delta S$ comes from only the extra higher-$k$ modes of the density perturbation (see Eq. (C.1)). The absence of correlation between these different wavenumbers means that the increment of $\delta(\mathbf{x};R)$ is independent of its previous value. It is also a Gaussian field, with zero mean and variance $\delta S$. Thus, considering $S$ as a 'time' variable, we find that $\delta(\mathbf{x};S)$ can be described by a Brownian motion.

The probability distribution of $\delta(\mathbf{x};R)$ is a Gaussian

$$P(\delta,S)\mathrm{d}\delta = \frac{1}{\sqrt{2\pi S}}\exp\left[-\frac{\delta^2}{2S}\right]\mathrm{d}\delta. \tag{C.3}$$

In an Einstein-de Sitter or a ΛCDM universe, the linear growth of initial density perturbations is scale-independent, so that $\delta(\mathbf{x})$ and $\sigma(R) = \sqrt{S}$ grow in the same manner, and as a result the density field will remain Gaussian while it is linear. Following the standard literature, hereafter we shall use $\delta(\mathbf{x};R)$ to denote the initial smoothed density perturbation extrapolated to the present time using linear perturbation theory, and the same for $\sigma$ or $S$.

In the standard cold dark matter scenario, the initial smoothed densities which, extrapolated to the present time, equal (exceed) $\delta_c$ correspond to regions where virialised dark matter halos have formed today (earlier). In an Einstein-de Sitter universe $\delta_c$ is a constant, while in a ΛCDM universe it depends on the matter density $\Omega_m$. In neither case does $\delta_c$ depend on the size of (or equivalently the mass enclosed in) the smoothed overdensity, or the environment surrounding the overdensity.

As a result, to see if a spherical region with initial radius $R$ has collapsed to virialised objects today or lives in some larger region which has collapsed earlier, we only need to see whether $\delta(\mathbf{x};\geq R) \geq \delta_c$. Put another way, the fraction of the total mass that is incorporated in virialised dark matter halos heavier than $M = \frac{4}{3}\pi R^3\bar{\rho}_i$ is just the fraction of the Brownian

motion trajectories $\delta(\mathbf{x}; S)$ which have crossed the constant barrier $\delta_c$ by the 'time' $S = S(R)$, which is given by Bond et al. (4)

$$F(M, z) = \frac{1}{\sqrt{2\pi S}} \int_{\frac{D_+(0)}{D_+(z)}\delta_c}^{\infty} \left[ e^{-\frac{\delta^2}{2S}} - e^{-\frac{(\delta - 2\delta_c)^2}{2S}} \right] \mathrm{d}\delta, \tag{C.4}$$

where the lower limit of the integral is $\frac{D_+(0)}{D_+(z)}\delta_c$, because if a virialised object formed at redshift $z$, then its corresponding initial smoothed density linearly extrapolated to $z$ is $\delta_c$, while extrapolated to today it is $\frac{D_+(0)}{D_+(z)}\delta_c$ with $D_+(z)$ being the linear growth factor at $z$. In Einstein-de Sitter cosmology $D_+(z) \propto (1+z)^{-1}$ and this quantity becomes $(1+z)\delta_c$.

Alternatively, one can say that the fraction of the total mass that is incorporated in halos, the radii of which fall in $[R, R + \delta R]$ (or equally $[S, S + \delta S]$) and which collapse at $z = z_f$ is given by

$$f(S, z_f)\mathrm{d}S = \frac{1}{\sqrt{2\pi S}} \frac{D_+(0)\delta_c}{D_+(z_f)S} \exp\left[ -\frac{D_+^2(0)\delta_c^2}{2D_+^2(z_f)S} \right] \mathrm{d}S, \tag{C.5}$$

where $f(S)$ the distribution of the first-crossing time of the Brownian motion to the barrier $D_+(z = 0)\delta_c / D_+(z = z_f)$. Once this is obtained, one can compute the halo mass function observed at $z_f$ as

$$\frac{\mathrm{d}n(M)}{\mathrm{d}M}\mathrm{d}M = \frac{\bar{\rho}_m(z_f)}{M} f(S)\mathrm{d}S. \tag{C.6}$$

Other observables, such as the dark matter halo bias (86) or merger history (66), can be computed with certain straightforward generalizations of the theory.

# Appendix D

# Comparing fixed- and moving-environment models

In the main text we use a moving-environment approximation in which the smoothing scale of the environment is a function of the void scale, specifically $R_{\rm env} = 5R$. However we have also checked the effect of using a fixed-environment approximation to calculate the fifth force. We compare the effect of the approximations on the environment-averaged first-crossing distribution in Fig. D.1, for a fixed-environment scale of $R_{\rm env} = 75\,{\rm Mpc}/h$, corresponding to $S_{\rm env} = 0.01$. The differences are below 10% for $\nu \gtrsim 1$, corresponding to final void radii $R_f \gtrsim 1\,{\rm Mpc}/h$. Thus, throughout the range of observable void sizes our conclusions are fairly insensitive to the precise approximation used to calculate the environmental effect of the fifth force.

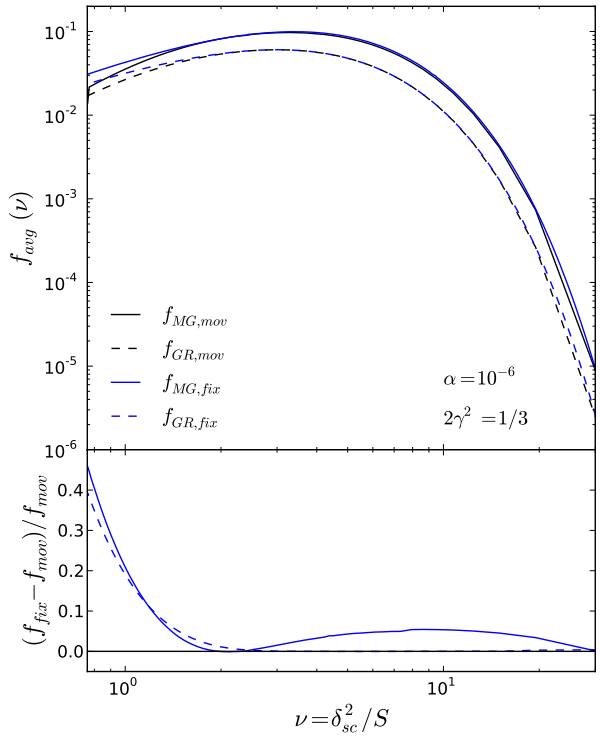


**Figure D.1:** *Upper panel:* Environment-averaged first-crossing distribution of voids with (solid lines) and without (dashed lines) the fifth force. The higher solid and higher dashed lines show results for the fixed-environment approximation, while the lower pair show the moving environment approximation. *Lower panel:* Fractional difference of fixed- from moving-environment approximation for modified gravity (solid) and GR (dashed). For $\nu \sim 1$ and larger, the observational range of interest, the difference is below 10%.

# Appendix E

# Theory variations

Figure E.1 shows the results for the conditional first-crossing distributions, for various parameter values. The results for any individual panel are qualitatively very similar to those for our fiducial model, $\alpha = 10^{-6}, \gamma = 1/3$. The main exception is for the $\alpha = 10^{-7}$ theories in very underdense environments, $\delta_{\rm env} \sim -2.4$. Here the random walk begins close to a barrier which is itself very near to the ΛCDM barrier. This situation shows that the monotonic increase of the deviation with void size is not universal.

In general, larger values of $\alpha$ allow for much greater variation in the conditional first-crossing distributions for various environments. Variations in the coupling $2\gamma^2$ cause less variation between the different environments. Finally, although it is more clearly seen after the environment averaging (Fig. 3.7), larger variations of the distribution with $2\gamma^2$ occur for larger $\alpha$ values.

## E. THEORY VARIATIONS

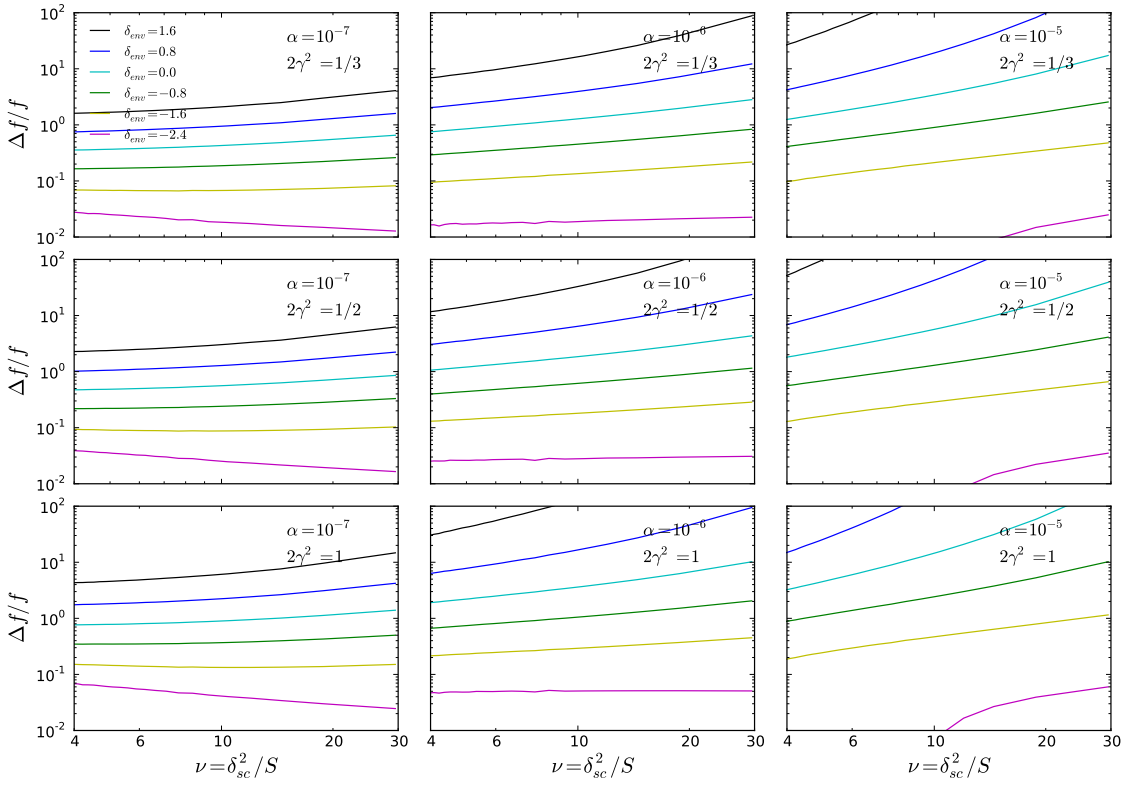


**Figure E.1:** Fractional differences of the conditional first-crossing distribution for various parameter values. Within each panel, $\delta_{\rm env}$ decreases from 1.6 to -2.4, from top to bottom. Our fiducial model is shown in the top center panel.

# Appendix F

# Halo ellipticity

In order to show that the contribution from halo ellipticity is small, we consider a very simple model which is even less spherical than an elliptical halo. Thus, if the shear from this model is negligible, then so is shear from elliptical halos. We take two point masses labelled E1 and E2 on Fig. F.1. These are each separated from the halo center by $\Delta \lesssim R_{\rm vir}$. The outermost square region pictured corresponds to the top square of Fig. 4.1, with side length $R_{\rm pair}$.

On the left panel of Fig. F.1 we extend two lines from E1 which are both 45 degrees from the horizontal axis. With our shear sign convention (Fig. 4.1), these lines describe points where the shear from E1 is purely $\gamma_2$, i.e., these lines are the zeros of $\gamma_1$. Thus, points which are on opposite sides of and equidistant from these lines have a net contribution of $\gamma_1 = 0$. As a result, the net $\gamma_1$ shear when summed over all galaxies in regions A and A' is zero. In the same way, regions B and B' sum to zero.

Likewise, on the right panel we draw a line from E2 which is 45 degrees from the vertical, and the net $\gamma_1$ shear in C and C' is zero. A final cancellation occurs in regions D and D', where the positive $\gamma_1$ shear from E1 in D cancels the negative shear from E2 in D'. The net shear from these two point masses is then given by the remaining regions, labelled $+\gamma$ and

$-\gamma$. These two regions do not cancel perfectly, but it is clear that (i) these regions nearly cancel: while the $+\gamma$ region is slightly closer to E1 than the $-\gamma$ region is to E2, in area, the $+\gamma$ region is slightly smaller; (ii) the size of these imperfectly cancelled regions shrinks rapidly as $\Delta/R_{\rm pair}$ gets smaller. The upper bound is

$$\Delta/R_{\rm pair} \leq \frac{R_{\rm vir}}{R_{\rm pair}} = \frac{1\ {\rm Mpc}/h}{6\ {\rm Mpc}/h}\,, \tag{F.1}$$

but most of our LRG pairs have smaller virial radii and larger pair separation. Furthermore, the density profile of halos falls off quickly, so that relatively little of the mass is displaced an entire virial radius from the center.

Finally, note two more points concerning the contribution of halo ellipticity to the systematic regions of Fig. 4.2. First, subtracting the signal in the left and right systematic regions, which have the same shape as the Signal region, partially removes the very small ellipticity contribution described above. Second, halo ellipticity could also contribute to the top and bottom systematic regions of Fig. 4.2. However, being offset by an additional distance of $R_{\rm pair}$, the contribution in these regions will be even smaller than the closer regions which we have just considered.

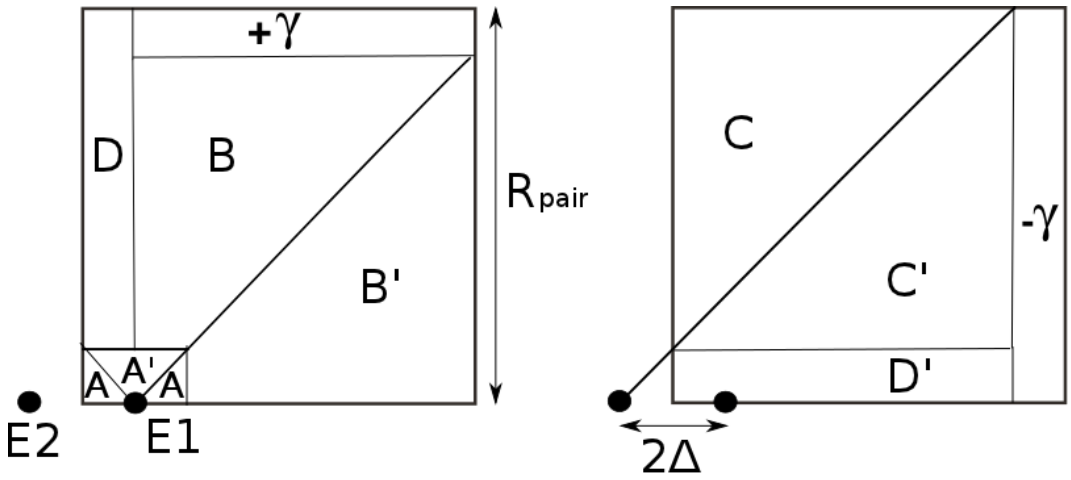


**Figure F.1:** As an extreme model of halo ellipticity, we consider the shear from point masses E1 and E2. The two panels show the same region twice: the left panel highlights the contribution from E1, and the right that from E2. The net $\gamma_1$ shear (with the sign convention of Fig. 4.1) cancels in regions A and A', B and B', etc. (See the text for the details.) The size of the uncancelled regions, $+\gamma$ and $-\gamma$, shrinks rapidly with the small number $\Delta/R_{\rm pair} \leq 1/6$, showing that contributions from halo ellipticity are highly suppressed in our measurement.

# References


[1] Babichev, E., Deffayet, C., & Ziour, R. 2009, International Journal of Modern Physics D, 18, 2147

[2] Baldi, M. 2011, MNRAS, 411, 1077

[3] Bernardeau, F., Colombi, S., Gaztañaga, E., & Scoccimarro, R. 2002, PhR, 367, 1

[4] Bond J. R., Cole S., Efstathiou G., Kaiser N., 1991, ApJ, 379, 440

[5] Brax, P., van de Bruck, C., Davis, A.-C., et al. 2011, Phys. Rev. D, 84, 123524

[6] Brainerd, T. G., Blandford, R. D., & Smail, I. 1996, ApJ, 466, 623

[7] Brax P., van de Bruck C., Davis A. C., Shaw D. J., 2010, PRD, 82, 063519

[8] Bullock, J. S., Kolatt, T. S., Sigad, Y., et al. 2001, MNRAS, 321, 559

[9] Cai, Y.-C., Cole, S., Jenkins, A., & Frenk, C. S. 2010, MNRAS, 407, 201

[10] Carlberg R. G., Couchman H. M. P., 1988, ApJ, 340, 47

[11] Carroll, S. M. 2004, Spacetime and geometry / Sean Carroll. San Francisco, CA, USA: Addison Wesley, ISBN 0-8053-8732-3, 2004, XIV + 513 pp.

[12] Carroll, S. M., Duvvuri, V., Trodden, M., & Turner, M. S. 2004, Phys. Rev. D, 70, 043528

[13] Cautun, M., van de Weygaert, R., Jones, B. J. T., & Frenk, C. S. 2014, arXiv:1401.7866

[14] Chan, K. C., & Scoccimarro, R. 2009, Phys. Rev. D, 80, 104005

[15] Clampitt, J., Jain, B., & Khoury, J. 2012, JCAP, 1, 30

[16] Clampitt, J., Cai, Y.-C., & Li, B. 2013, MNRAS, 431, 749

[17] Clampitt, J., Jain, B., & Takada, M. 2014, arXiv:1402.3302

[18] Colberg, J. M., Krughoff, K. S., & Connolly, A. J. 2005, MNRAS, 359, 272

[19] Colberg, J. M., Pearce, F., Foster, C., et al. 2008, MNRAS, 387, 933

[20] Cole S., Kaiser N., 1988, MNRAS, 233, 637

[21] Cole S., Kaiser N., 1989, MNRAS, 237, 1127

[22] Cooray, A., Sheth, R. 2002, Phys. Rep., 372, 1

[23] Cruz, M., Martínez-González, E., Vielva, P., & Cayón, L. 2005, MNRAS, 356, 29

[24] Damour, T., & Polyakov, A. M. 1994, Nuclear Physics B, 423, 532

[25] Davis, A.-C., Li, B., Mota, D. F., & Winther, H. A. 2012, ApJ, 748, 61

[26] Dietrich, J. P., Werner, N., Clowe, D., et al. 2012, Nature (London), 487, 202

[27] Dvali, G., Gabadadze, G., & Porrati, M. 2000, Physics Letters B, 485, 208

[28] Efstathiou G., Rees M., MNRAS, 230, 5

[29] Efstathiou G., Frenk C. S., White S. D. M., Davis M., 1988, MNRAS, 235, 715

[30] Enqvist, K., Hotchkiss, S., & Taanila, O. 2011, JCAP, 4, 17

[31] Feix, M., Xu, D., Shan, H., et al. 2008, ApJ, 682, 711

[32] Flender, S., Hotchkiss, S., & Nadathur, S. 2012, arXiv:1212.0776

[33] Furlanetto, S. R., & Piran, T. 2006, MNRAS, 366, 467

[34] Goroff, M. H., Grinstein, B., Rey, S.-J., & Wise, M. B. 1986, ApJ, 311, 6

[35] Granett, B. R., Neyrinck, M. C., & Szapudi, I. 2008, ApJL, 683, L99

[36] Hamaus, N., Wandelt, B. D., Sutter, P. M., Lavaux, G., & Warren, M. S. 2014, Physical Review Letters, 112, 041304

[37] Hamaus, N., Sutter, P. M., & Wandelt, B. D. 2014, arXiv:1403.5499

[38] Harrison, I., & Coles, P. 2012, MNRAS, 421, L19

[39] Hernandez-Monteagudo, C., & Smith, R. E. 2012, arXiv:1212.1174

[40] Higuchi, Y., Oguri, M., & Hamana, T. 2013, MNRAS, 432, 1021

[41] Hikage, C., Mandelbaum, R., Takada, M., Spergel, D. N. 2013, MNRAS, 435, 2345

[42] Hinterbichler, K., & Khoury, J. 2010, Physical Review Letters, 104, 231301

[43] Hinterbichler, K., Khoury, J., Levy, A., & Matas, A. 2011, Phys. Rev. D, 84, 103521

[44] Hogg, D. W. 1999, arXiv:astro-ph/9905116

[45] Holz, D. E., & Perlmutter, S. 2012, ApJL, 755, L36

[46] Hotchkiss, S. 2011, JCAP, 7, 4

[47] Hoyle, F., & Vogeley, M. S. 2002, ApJ, 566, 641

[48] Hoyle, F., & Vogeley, M. S. 2004, ApJ, 607, 751

[49] Hoyle, F., Vogeley, M. S., & Pan, D. 2012, MNRAS, 426, 3041

[50] Hoyle, B., Jimenez, R., & Verde, L. 2011, Phys. Rev. D, 83, 103502

[51] Hoyle, B., Jimenez, R., Verde, L., & Hotchkiss, S. 2012, JCAP, 2, 9

[52] Hu, W., & Sawicki, I. 2007, Phys. Rev. D, 76, 064004

[53] Hui, L., Nicolis, A., & Stubbs, C. W. 2009, Phys. Rev. D, 80, 104002

[54] Inoue, K. T., & Silk, J. 2006, ApJ, 648, 23

[55] Jain, B., & Zhang, P. 2008, Phys. Rev. D, 78, 063503

[56] Jain, B., & Khoury, J. 2010, Annals of Physics, 325, 1479

[57] Jain, B., & VanderPlas, J. 2011, JCAP, 10, 32

[58] Jain, B., Vikram, V., & Sakstein, J. 2013, ApJ, 779, 39

[59] Jauzac, M., Jullo, E., Kneib, J.-P., et al. 2012, MNRAS, 426, 3369

[60] Jee, M. J., Dawson, K. S., Hoekstra, H., et al. 2011, ApJ, 737, 59

[61] Jennings, E., Li, Y., & Hu, W. 2013, MNRAS, 434, 2167

[62] Kazin, E. A., Blanton, M. R., Scoccimarro, R., et al. 2010, ApJ, 710, 1444

[63] Khoury, J., & Weltman, A. 2004, Physical Review Letters, 93, 171104

[64] Khoury, J., & Weltman, A. 2004, Phys. Rev. D, 69, 044026

[65] Krause, E., Chang, T.-C., Doré, O., & Umetsu, K. 2013, ApJL, 762, L20

[66] Lacey C., Cole S., 1993, MNRAS, 262, 627

[67] Lam, T. Y., Nishimichi, T., Schmidt, F., & Takada, M. 2012, Physical Review Letters, 109, 051301

[68] Lavaux, G., & Wandelt, B. D. 2012, ApJ, 754, 109

[69] Lee, J., Springel, V., Pen, U.-L., & Lemson, G. 2008, MNRAS, 389, 1266

[70] Li B., 2011, MNRAS, 411, 2615

[71] Li B., Barrow J. D., 2011, PRD, 83, 024007

[72] Li, B., & Efstathiou, G. 2012, MNRAS, 421, 1431

[73] Li, B., & Lam, T. Y. 2012, MNRAS, 425, 730

[74] Li, B., Zhao, G.-B., & Koyama, K. 2012, MNRAS, 421, 3481

[75] Li B., Zhao H., 2010, PRD, 81, 104047

[76] Li, B., & Zhao, H. 2009, Phys. Rev. D, 80, 044027

[77] Mandelbaum, R., Hirata, C. M., Seljak, U., et al. 2005, MNRAS, 361, 1287

[78] Mandelbaum, R., Seljak, U., & Hirata, C. M. 2008, JCAP, 8, 6

[79] Mandelbaum, R., Slosar, A., Baldauf, T., et al. 2013, MNRAS, 432, 1544

[80] Martino, M. C., & Sheth, R. K. 2009, arXiv:0911.1829

[81] Martino M., Stabenau H. F., Sheth, R. K., 2009, PRD, 79, 084013

[82] Masina, I., & Notari, A. 2009, JCAP, 2, 19

[83] Maturi, M., & Merten, J. 2013, arXiv:1306.0015

[84] Mead, J. M. G., King, L. J., & McCarthy, I. G. 2010, MNRAS, 401, 2257

[85] Melchior, P., Sutter, P. M., Sheldon, E. S., Krause, E., & Wandelt, B. D. 2013, arXiv:1309.2045

[86] Mo H. J., White S. D. M., 1996, MNRAS, 282, 347

[87] Mota, D. F., & Shaw, D. J. 2007, Phys. Rev. D, 75, 063501

## 5. REFERENCES


[88] Musso, M., & Sheth, R. K. 2012, MNRAS, 423, L102

[89] Nadathur, S., Hotchkiss, S., & Sarkar, S. 2012, JCAP, 6, 42

[90] Narayan R., White S. D. M., 1987, MNRAS, 231, 97

[91] Narayan, R., & Bartelmann, M. 1996, arXiv:astro-ph/9606001

[92] Navarro, J. F., Frenk, C. S., & White, S. D. M. 1997, ApJ, 490, 493

[93] Neyrinck, M. C. 2008, MNRAS, 386, 2101

[94] Nicolis, A., Rattazzi, R., & Trincherini, E. 2009, Phys. Rev. D, 79, 064036a

[95] Nishimichi, T., Taruya, A. 2011, PRD, 84, 043526

[96] Nojiri, S., & Odintsov, S. D. 2003, Phys. Rev. D, 68, 123512

[97] Norberg, P., Baugh, C. M., Gaztañaga, E., & Croton, D. J. 2009, MNRAS, 396, 19

[98] Okumura, T., Jing, Y. P., & Li, C. 2009, ApJ, 694, 214

[99] Olive, K. A., & Pospelov, M. 2008, Phys. Rev. D, 77, 043524

[100] Padmanabhan, T. 2010, Gravitation: Foundations and Frontiers by T. Padmanabhan. Cambridge University Press, 2010. ISBN: 9780521882231

[101] Pan, D. C., Vogeley, M. S., Hoyle, F., Choi, Y.-Y., & Park, C. 2012, MNRAS, 421, 926

[102] Pápai, P., Szapudi, I., & Granett, B. R. 2011, ApJ, 732, 27

[103] Paranjape, A., Lam, T. Y., & Sheth, R. K. 2012, MNRAS, 420, 1648

[104] Parfrey K., Hui L., Sheth, R. K., 2011, PRD, 83, 063511

[105] Peebles, P. J. E. 2001, ApJ, 557, 495

[106] Peebles, P. J. E., & Nusser, A. 2010, Nature (London), 465, 565

[107] Pietroni, M. 2005, Phys. Rev. D, 72, 043535

[108] Platen, E., van de Weygaert, R., & Jones, B. J. T. 2007, MNRAS, 380, 551

[109] Pourhasan, R., Afshordi, N., Mann, R. B., & Davis, A. C. 2011, JCAP, 12, 5

[110] Rudnick, L., Brown, S., & Williams, L. R. 2007, ApJ, 671, 40

[111] Sachs, R. K., & Wolfe, A. M. 1967, ApJ, 147, 73

[112] Schaeffer R., Silk J., 1988, ApJ, 292, 319

[113] Schmidt, F. 2009, Phys. Rev. D, 80, 123003

[114] Schmidt, F., Lima, M., Oyaizu, H., & Hu, W. 2009, Phys. Rev. D, 79, 083518

[115] Schmidt, F. 2010, Phys. Rev. D, 81, 103002

[116] Shandarin, S., Feldman, H. A., Heitmann, K., & Habib, S. 2006, MNRAS, 367, 1629

[117] Sheldon, E. S., Johnston, D. E., Scranton, R., et al. 2009, ApJ, 703, 2217

[118] Sheldon, E. S., Johnston, D. E., Masjedi, M., et al. 2009, ApJ, 703, 2232

[119] Sheth R. K., 1998, MNRAS, 300, 1057

[120] Sheth R. K., Tormen G., 2002, MNRAS, 329, 61

[121] Sheth R. K., van de Weygaert R., 2004, MNRAS, 350, 517

[122] Simon, P., Watts, P., Schneider, P., et al. 2008, A&A, 479, 655

[123] Simon, P., et al., 2013, MNRAS, 430, 2476

[124] Sousbie, T. 2011, MNRAS, 414, 350

[125] Sutter, P. M., Lavaux, G., Wandelt, B. D., & Weinberg, D. H. 2012, ApJ, 761, 44

[126] Sutter, P. M., Lavaux, G., Wandelt, B. D., & Weinberg, D. H. 2012, ApJ, 761, 187

[127] Sutter, P. M., Lavaux, G., Wandelt, B. D., et al. 2013, arXiv:1309.5087

[128] Sutter, P. M., Lavaux, G., Wandelt, B. D., Weinberg, D. H., & Warren, M. S. 2014, MNRAS, 438, 3177

[129] Takada, M., Jain, B. 2003, MNRAS, 340, 580

[130] Tavasoli, S., Vasei, K., & Mohayaee, R. 2012, arXiv:1210.2432

[131] Tikhonov, A. V., & Klypin, A. 2009, MNRAS, 395, 1915

[132] Tinker, J. L., & Conroy, C. 2009, ApJ, 691, 633

[133] Vainshtein, A. I.972, Phys. Letters B , 39, 3

[134] Vikram, V., Cabré, A., Jain, B., & VanderPlas, J. T. 2013, JCAP, 8, 20

[135] Waizmann, J.-C., Ettori, S., & Bartelmann, M. 2012, arXiv:1210.6021

[136] Waizmann, J.-C., Ettori, S., & Moscardini, L. 2012, MNRAS, 420, 1754

[137] Wang, J., Hui, L., & Khoury, J. 2012, Physical Review Letters, 109, 241301

[138] Will, C. M.005, Living Rev. Rel., 9, 3

[139] Wright, C. O., & Brainerd, T. G. 2000, ApJ, 534, 34

[140] Zhang J., Hui L., 206, ApJ, 641, 641

[141] Zhang, Y., Dietrich, J. P., McKay, T. A., Sheldon, E. S., & Nguyen, A. T. Q. 2013, arXiv:1304.6696

[142] Zhao, G.-B., Pogosian, L., Silvestri, A., & Zylberberg, J. 2009, Phys. Rev. D, 79, 083513

[143] Zhao, G.-B., Li, B., & Koyama, K. 2011, Phys. Rev. D, 83, 044007

[144] Zhao, H., Macciò, A. V., Li, B., Hoekstra, H., & Feix, M. 2010, ApJL, 712, L179